STRUCTURE OF THE AIRFLOW ABOVE SURFACE WAVES

by

Marc Buckley

A dissertation submitted to the Faculty of the University of Delaware in partial fulfillment of the requirements for the degree of Doctor of Philosophy in Marine Studies

Summer 2015

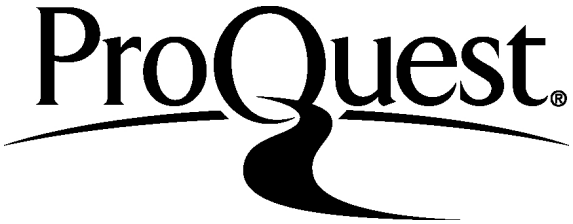

STRUCTURE OF THE AIRFLOW ABOVE SURFACE WAVES

by

Marc Buckley

Approved: _____
Mark A. Moline, Ph.D.
Director of the School of Marine Science and Policy

Approved: _____
Mohsen Badiey, Ph.D.
Acting Dean of the College of Earth, Ocean, and Environment

Approved: _____
James G. Richards, Ph.D.
Vice Provost for Graduate and Professional Education

I certify that I have read this dissertation and that in my opinion it meets the academic and professional standard required by the University as a dissertation for the degree of Doctor of Philosophy.

Signed: _____

Fabrice Veron, Ph.D.
Professor in charge of dissertation

I certify that I have read this dissertation and that in my opinion it meets the academic and professional standard required by the University as a dissertation for the degree of Doctor of Philosophy.

Signed: _____

I. Pablo Huq, Ph.D.
Member of dissertation committee

I certify that I have read this dissertation and that in my opinion it meets the academic and professional standard required by the University as a dissertation for the degree of Doctor of Philosophy.

Signed: _____

Tobias Kukulka, Ph.D.
Member of dissertation committee

I certify that I have read this dissertation and that in my opinion it meets the academic and professional standard required by the University as a dissertation for the degree of Doctor of Philosophy.

Signed: _____

Peter P. Sullivan, Ph.D.
Member of dissertation committee

ACKNOWLEDGEMENTS

I thank my Ph.D. advisor, Fabrice Veron, for giving me the opportunity to learn and grow. His guidance, enthusiasm, and extensive experience and scientific knowledge, were crucial for the completion of my doctoral research. He provided me with many degrees of freedom, which allowed me to explore and experiment, and develop a passion for this type of work.

I also thank my committee members, I. Pablo Huq, Tobias Kukulka, and Peter P. Sullivan, for their invaluable comments and insightful discussions.

I thank Frédéric Cyr for his important contribution to the field results presented in this paper. His efforts toward the design and construction of the R/P *Cheval Blanc*, the development and testing of the experimental setup, and the data acquisition, were essential.

Thank you to my parents, and to my brother Julien, for their love and support.

Finally, I thank my wife, Yoana.

TABLE OF CONTENTS

LIST OF TABLES

LIST OF FIGURES

ABSTRACT

We present a laboratory investigation of the structure of the turbulent airflow above water surface gravity waves. Specifically, we investigate the intimate coupling of the wind with the waves, and we examine the role of the turbulent airflow kinematics for the momentum flux across the air-water interface.

The airflow dynamics above the air-sea interface are believed to have a significant impact on the fluxes of momentum and scalars across the ocean surface. We present an experimental study of the turbulent structure of the airflow above waves, including instantaneous, mean, and wave-phase-averaged airflow characteristics. Measurements, taken at a fetch of 22.7 m in University of Delaware's large wind-wave-current facility, are reported. We present results for a total of 17 different wind-wave conditions, including 5 wind wave experiments with 10-m extrapolated wind speeds spanning from 2.19 m s^{-1} to 16.63 m s^{-1}. By combining winds with mechanically generated swells, we were able to achieve a wide range of wave ages C_p/u_*, from 1.4 to 66.7, where C_p is the peak wave phase speed, and u_* the air friction velocity. In order to complete this study, we developed a complex imaging system, combining particle image velocimetry with laser induced fluorescence techniques. High resolution two-dimensional (18.7 x 9.7 cm^2) velocity fields were measured as close as 100 μm above the air-water interface (on average). In addition, we acquired high spatial and temporal resolution wave field data simultaneously with the airflow measurements.

The mean velocity profile follows the law of the wall in low winds ($U_{10} = 0.86$ m s^{-1}, no waves detected). Over wind waves, the aerodynamic roughness of the airflow increases with increasing wind speed. Using our imaging system, we were able to measure airflow velocities within the viscous sublayer of the airflow boundary layer. Viscous sublayers remain intact and coherent upwind of wave crests at least up to a

moderate wind speed of $U_{10} = 9.41$ m s^{-1}. We were able to measure two-dimensional near-surface spanwise vorticity fields in the airflow. We observe direct evidence of airflow separation events past the crests of wind waves, starting at low to moderate wind speeds ($U_{10} > 2.19$ m s^{-1}). With increasing wind speed, the contribution of viscous stress to total wind stress decreases exponentially (in favor of form drag), and the frequency of airflow separation events increases. At high wind speeds ($U_{10} = 16.63$ m s^{-1}), over 85% of the waves experience airflow separation. Airflow separation causes dramatic along-wave variations in viscous stress.

In all 17 experiments, the turbulent boundary layer in the air is characterized by numerous velocity sweeps and ejections, accompanied by intense downwind-tilted spanwise vorticity (shear) layers stemming from the surface. We were able to directly observe these turbulent events, and estimate their statistical significance using quadrant analysis. These events become phase-locked in the presence of waves, and over young wind waves ($C_p/u_* < 3.7$), they are replaced by intermittent airflow separation events past wave crests. The mean airflow is subjected to a sheltering effect past wave crests, above the critical height ζ_c (defined by $\langle u(\zeta_c)\rangle = C_p$). Mean along-wave turbulent momentum and energy in the airflow are also phase-locked. Intermittent airflow separation events past young wave crests cause free high shear layers to generate on average intense turbulence downwind of crests. We observe an opposite, upwind sheltering effect below the critical height. The airflow within the critical layer is strongly coupled with the wave orbital velocities at the water surface, starting at relatively low wave ages ($C_p/u_* = 6.5$).

Preliminary instantaneous field measurements are consistent with our laboratory results.

Chapter 1

INTRODUCTION

The transfers of heat, momentum, mass and energy across the ocean surface have an important impact on large scale weather patterns, sea-state, and climate. As such, they are crucial components for the motions and thermodynamical states of both the ocean and the atmosphere. These fluxes are, in turn, largely controlled by the small scale dynamics that take place at the interface between the coupled marine atmospheric (MABL) and oceanic boundary layers (OBL). A casual observer of the ocean surface may notice that this wavy interface is very dynamic, rather complex, and constantly changing. In particular, one can readily observe that wind blowing over the open ocean surface generates waves, causes them to grow; the generated waves may eventually break and entrain air (whitecapping), injecting bubbles into the water. These wind waves may also mix and interact with other waves, including with longer swells, generated far away and long ago, thus giving the ocean surface a complex appearance, with a large range of spatial and temporal scales. A more experienced observer may notice that wind gusts rapidly and directly affect the water surface, in that a rhombic-like streak pattern may be formed upwind of crests, and parasitic capillaries appear just downwind of crests. A more patient (or lucky) observer, may notice the formation of streaks of foam at the ocean surface (the foam from the whitecaps), in the along-wind direction (surface convergence caused by Langmuir circulations). In fact, experienced mariners are generally capable of estimating the wind speed by visually assessing the appearance of the ocean surface, and in particular by estimating the density of whitecaps (caused by air entraining breaking waves) at the ocean surface. The general rule of thumb is that frequent whitecapping starts at wind speeds upward of 11-16 knots (6-8 m s^{-1}). The Beaufort scale, which relates wind speed to observed

conditions at sea, was devised by Irish Royal Navy officer Francis Beaufort in 1805, and is still commonly used by mariners today. Finally, the most adventurous observer, after strong enough wind conditions, may go home with a salty aftertaste, testament to the presence of marine aerosols in the air, caused by the ejection of water droplets into the atmosphere upon wave breaking (ocean spray) and subsequent evaporation.

These visible and tangible expressions of the coupling between wind and waves are only a hint to the complexity of the dynamics at the air-sea interface. Complex motions directly related to wind-wave interactions extend for some distance into both the MABL and the OBL. This region, directly coupled with the waves, is commonly called the wave boundary layer (WBL). On the water side, intense mixing is generated within the WBL by wave breaking that extends for some distance below the water surface. Langmuir circulations, intimately connected with Stokes drift, may cause a drastic increase in the depth of the mixed layer, capable of rapidly mechanically destroying density or temperature related stratification. Stokes drift is itself dramatically affected by wave breaking. On the air side, airflow separation events past wave crests, streamwise vorticity structures, and the general coupling of the turbulence with the wave field below, may have important consequences for the motions throughout a significant portion of the MABL.

Recently, the complex feedback mechanisms involved in the coupling between wind and waves and their effects on the atmospheric and oceanic boundary layers have received increased interest, particularly in the context of extreme weather forecasts and climate models (Sullivan and McWilliams, 2010). The development of extreme weather events (such as hurricanes) is dependent on the drag at the ocean surface (Powell et al., 2003; Donelan et al., 2004; Bell et al., 2012). At high wind speeds, the onset of wave breaking events and sea spray generation are contingent upon the wind shear at the ocean surface (Veron, 2015). Ocean spray is in turn thought to contribute to the development of large storm systems, because it enhances latent and sensible heat fluxes at the air-sea interface (Veron, 2015). In addition, the dynamics at the air-sea interface in high wind speeds are important for the transfer of gas across the

ocean surface, which is believed to be significantly enhanced by the wave breaking and bubble entrainment events that occur at high wind speeds (Edson et al., 2011). Global budgets of heat, gas and momentum fluxes at the air-sea interface are crucial for climate and ocean models, in particular in the context of climate change and ocean acidification (Friedlingstein et al., 2014). Yet, although drag parameterizations at high wind speeds have recently improved (e.g., Edson et al., 2013), the limited understanding of the mechanisms involved, remains problematic for accurate extreme weather and sea state prediction. This is due in part to the technical challenges involved in obtaining observations at the air-water interface in the laboratory, let alone in the field, as well as the difficulty in understanding and modeling the complex feedback mechanisms between highly nonlinear waves and the turbulent airflow.

This study focuses on the turbulent airflow above surface waves and their coupling. To this end, we will present results from extensive laboratory experiments, within the context of previous contributions to this field of research, including theoretical, experimental (laboratory and field), and numerical investigations.

1.1 Previous Contributions

As was emphasized by Jones and Toba (2001), current parameterizations of air-sea momentum fluxes are based on the "law of the wall", developed by aerodynamicists at the beginning of the twentieth century. Succinctly, the law of the wall relates the drag over a solid surface to its physical roughness, and identifies a self-similar log-linear velocity profile. Meteorologists were able to develop a similar law, that accounts for buoyancy effects, or Monin-Obukhov similarity theory (Monin and Obukhov, 1954), and model with relative success the drag of the turbulent atmospheric boundary layer over land.

Over water however, the problem is more complex, since the water surface is constantly moving and reacting to the airflow above. However rough the water surface may look, the total drag is not well estimated by assimilating the water surface to a solid rough wall, because a portion of the airflow momentum (and energy) is transferred to

and from the waves and currents, which in turn strongly impacts the total drag, through complex feedback processes. The mechanisms by which wind inputs momentum and energy toward the growth of waves are arguably an important component of the total flux, and yet they are still not fully understood, in spite of a large body of past work on the subject.

1.1.1 Wind wave generation theories

The question of the generation of waves by wind at the ocean surface has a very long history. Khandekar (1989) mentions that "Greek philosopher Aristotle (382-322 B.C.) recognized the importance of wind on wave generation". Phillips (1977) acknowledges the important contributions of eighteenth to early twentieth century "pioneers of theoretical fluid mechanics, Lagrange, Airy, Stokes and Rayleigh, [who] sought to account for the elementary properties of surface waves in terms of perfect fluid theory". Finally Bretschneider (1965) reports that the first ever recorded laboratory wave experiments were published by Weber and Weber (1825), that field observations were first documented by Paris (1871), and that Stevenson (1886) derived the first known empirical formula for wave generation, relating wave height to wind speed and fetch, or "length of water surface exposed to the wind" (Stevenson, 1886). The earlier contribution of Russell (1844) should also be mentioned here, since he had already reported a wind velocity threshold between capillary wind waves and regular gravity waves, as was later noted by Jeffreys (1925). A more recent review by Craik (2004) on the origins of water wave theory provides additional details on the important contributions of Russell (1844).

To synthesize very broadly almost 150 years of wind wave generation theory, essentially two approaches have been used to explain the generation and growth of waves under the action of wind: (1) a laminar instability mechanism, and (2) an aerodynamic sheltering mechanism.

1.1.1.1 Instability mechanisms

The first instability mechanism that was applied to wind wave generation is the Kelvin-Helmholtz shear instability theory, which can be attributed to Kelvin (1871) and Helmholtz (1868), and details of which can be found for example in Lamb (1932). The theory is essentially a stability analysis of the interface between two fluids with different densities and velocities. In these conditions, a linear stability analysis of the Bernoulli equation, which is the inviscid momentum balance (Euler equation) integrated along a streamline, suggests the existence of growing waves when:

$$g\left(\rho_w^2 - \rho_a^2\right) < k\rho_a\rho_w\left(U_a - U_w\right)^2 \tag{1.1}$$

where ρ_a and ρ_w are the densities of respectively the air and the water, k is the wave number of the unstable mode at the interface, g is the gravitational acceleration, U_a and U_w are the constant velocities respectively of the air and the water. The instability condition in equation 1.1 suggests that waves would exist as soon as the wind speed is greater than zero. Adding another restoring force in addition to gravity, the surface tension at the water surface, results in the following condition for wave generation:

$$g\left(\rho_w^2 - \rho_a^2\right) + k^2\sigma\left(\rho_a + \rho_w\right) < k\rho_a\rho_w\left(U_a - U_w\right)^2 \tag{1.2}$$

where σ is the water surface tension. This would now suggest that waves can only be generated by winds greater than 6.5 m s^{-1}. Neither of these conditions are in accord with past observations (e.g., Barnett and Kenyon, 1975; Kahma and Donelan, 1988), nor with the results presented in the following chapters. Recently however, it has been suggested that in hurricane wind speeds, where gravity and surface tension may be more readily overcome, Kelvin-Helmholtz type instabilities may control the formation of spume at the air-sea interface (Soloviev et al., 2014).

Later, Miles (1957) proposed a more elaborate instability theory, based on linear stability analysis of a stratified laminar shear flow. Here, already existing waves cause

an air-side shear instability which in turn forces them to grow. The predicted growth rate is exponential, and proportional to the curvature to slope ratio of the mean wind profile at the critical height, which is the height above the water surface where the mean wind velocity matches the phase speed of the water waves. Miles' critical layer mechanism implies that younger waves grow more rapidly than older waves. The critical layer is then very thin, and the curvature to slope ratio of the logarithmic wind profile is very large. In the limiting case of very young waves where the critical height is within the viscous sublayer, Miles' theory predicts very little wave growth. A number of modifications were subsequently applied to Miles' theory, to include effects of viscosity (Miles, 1962), and of turbulence (Phillips, 1977; Janssen, 1991; Miles, 1993).

Finally, Phillips (1957) suggested that waves are generated by resonance between turbulent pressure fluctuations in the air and the disturbed water surface. While the linear (as a function time) wave growth rates predicted by Phillips' theory may explain the initial stages of wave generation, they are not sufficient to explain observed exponential growth rates of already formed waves (e.g, Barnett and Kenyon, 1975). Phillips later combined his turbulent pressure generation mechanism with Miles' critical wave growth mechanism (Phillips, 1977).

1.1.1.2 Aerodynamic sheltering past wave crests

Jeffreys (1925) suggested that once the waves were generated, wave growth resulted from the along-wave pressure differential caused by airflow separation past wave crests. This idea is commonly known as the "sheltering hypothesis". It is derived from the known behavior of a turbulent airflow past a blunt body. Jeffreys (1925) essentially suggested that boundary layer separation occurred past wave crests, as it does past solid blunt bodies, and that the resulting asymmetry in the airflow would cause important pressure-slope correlations, favorable to wave growth.

Later, Stanton et al. (1932); Motzfeld (1937) were able to measure wave-induced pressure perturbations in the airflow above a solid wavy surface. Their results discredited Jeffreys' hypothesis, because they found that the sheltering effect caused by the

along-wave (solid wave) pressure differential was too weak (by an order of magnitude) to explain the growth rate of real water waves. Yet in his review on wind wave generation, Ursell (1956) emphasizes that measurements over solid surfaces may not be applicable to the wind-wave problem.

With pressure-slope correlations (form stress) apparently too weak to explain observed values of wave growth, Sverdrup and Munk (1947) suggested that, since tangential wind stress visibly transfers momentum to the water in the form of wind drift, it may also contribute to wave growth. This marked the beginning of a vigorous debate on the relative importance of tangential versus form stress for the total drag at the ocean surface.

Later, Belcher et al. (1993) and Belcher and Hunt (1998) improved and generalized the sheltering hypothesis, and introduced the term of "non-separated sheltering", which is the mechanism whereby a turbulent boundary layer thickens past a hill or a blunt body. Belcher and Hunt (1998) emphasized the importance of the work of wave-coherent turbulent forces, resulting in an along-wave pressure differential, favorable to wave growth.

Finally, as was well summarized by Sullivan and McWilliams (2010), "the existing theories and models are unable to reconcile their predictions of wave growth with available measurements, thus hinting to missing dynamics".

Next, we discuss past and current efforts to generate and acquire data that may help identify these dynamics. These efforts have been largely motivated by the need to understand and predict the momentum flux (wind stress) across the ocean surface.

1.1.2 Understanding the wind stress at the ocean surface

1.1.2.1 Models

Direct numerical simulations (DNS) have provided details on the structure of the airflow (Sullivan et al., 2000; Yang and Shen, 2010) and some have essentially supported the prediction by Belcher and Hunt (1998), that Miles' critical layer mechanism may be important for wave growth for intermediate wave ages ($15 \lesssim C_p/u_* \lesssim 25$,

where C_p is the speed of the dominant wave, and u_* the friction velocity of the air), whereas turbulence-driven sheltering effects dominate for young ($C_p/u_* \lesssim 15$) and for old waves ($C_p/u_* \gtrsim 25$) (Kihara et al., 2007). However due to high computational costs, DNS studies have been restricted to idealized monochromatic waves. Other modeling efforts were employed toward parameterizing wind-wave momentum fluxes over more realistic wide-spectrum wave fields (e.g., Makin et al., 1995; Hara and Belcher, 2002; Mueller and Veron, 2009). These suggested that the turbulent shear stress is reduced by the presence of the wave field and replaced by wave-coherent stress. Breaking waves and their effect on form drag were explicitly accounted for in momentum flux models by Kukulka and Hara (2008a,b); Suzuki et al. (2014). Recently, modelers were able to integrate realistic complex wave fields into large-eddy simulations (LES) and obtain insight on the instantaneous turbulent structure of the airflow over a wide range of wave ages (Yang et al., 2013; Sullivan et al., 2014), including very old waves (Sullivan et al., 2008) where upward wave-induced momentum flux was observed, as well as wave-driven jets, in agreement with field observations by Smedman et al. (1999) and Grachev and Fairall (2001).

1.1.2.2 Field measurements

Past and recent field observations have been largely of two kinds. The first, motivated by the need to forecast sea states, especially in rough weather conditions, followed a statistical/spectral approach. Important contributors to this effort were the wave growth and swell decay observations in the Joint North Sea Wave Project (JONSWAP, Hasselmann et al., 1973). In fact, their results provided wave spectra a wave growth rate baselines for a number of ensuing experiments, theories and models (e.g., Kahma and Calkoen, 1992). More recently, a number of turbulent flux measurement field campaigns were carried out, with the objective of parameterizing drag as a function of wind speed (see for example the COARE momentum flux model, Webster and Lukas, 1992). An important application for this work is the need to rapidly improve operational forecasting and climate modeling (e.g., Edson et al., 2013).

The second type of field measurements, have been concerned with the fundamental physics of wave generation and growth mechanisms. Important recent results were obtained by Donelan et al. (2006); Babanin et al. (2007), who, using a wave following pressure sensor (Donelan et al., 2005), were able to estimate the importance of form drag on the momentum transfer from wind to waves. Their results emphasized the important influence of airflow separation past the crests of steep waves, on the total flux. Later, Hristov et al. (2003); Grare et al. (2013a) obtained turbulent velocity profiles above waves, and were able to correlate them to the phase of the waves, thereby accessing (highly sought after) wave-coherent fluxes. They found evidence of Miles' critical layer mechanism for a certain range of wave ages. However these field studies were confronted to the obvious technical difficulties involved with the study of small scale dynamics in the open ocean in the viscinity of a highly dynamic interface (with a wide range of spatial and temporal scales). Hence they were limited to fixed height vertical profiler measurements, some distance above the level of the highest wave crest, rendering a full picture of the near-surface dynamics impossible. This means that in the field, our understanding of the near-surface distortion of the turbulence by the wave field below, is still incomplete.

1.1.2.3 Laboratory experiments

Laboratory measurements, although also technically challenging, have attempted to fill this knowledge gap. Hsu et al. (1981) observed a strong modulation of the wave-coherent stress by the wave-coherent turbulent stress, but their data were obtained over idealized mechanically generated waves. Later Mastenbroek et al. (1996) found evidence that rapid distortion (Batchelor and Proudman, 1954) of the turbulence occurs above the critical height, which has important implications on turbulence closure models, and, in particular, questions the validity of the commonly used eddy viscosity-type closure.

An important element of the momentum flux debate has been to determine the conditions of occurrence of airflow separation past wave crests, and the impact of

airflow separation on the internal structure of the momentum flux, and on the total drag at the ocean surface. Significant contributions to this problem have been those of Banner and Melville (1976) and later Gent and Taylor (1977), who suggested, based on theoretical grounds, that airflow separation can only occur over breaking waves. Their predictions were rapidly followed by a number of laboratory studies on the turbulent structure of the airflow above waves (Okuda et al., 1977; Kawamura et al., 1981; Kawai, 1981, 1982; Kawamura and Toba, 1988; Banner, 1990), where airflow separation events were suggested to occur. Returning to the tangential versus form stress debate, the first authors (Okuda et al., 1977) found that tangential stresses dominate the air-water momentum flux, while the last (Banner, 1990) observed a dominance of form drag. Later using Particle Image Velocimetry (PIV) in the water below wind waves, Banner and Peirson (1998), were able to measure near-surface tangential stresses. They concluded that when they are first being formed, waves are mostly subjected to tangential stress, whereas once they are further developed, form drag dominates the momentum flux. However the exact effect of airflow separation on the the stress distribution at the surface was not estimated, because of limited quantitative measurements and resolution. Higher resolution, air-side PIV measurements were limited to mechanical waves (Reul et al., 1999) until the work by Veron et al. (2007), who were able to directly measure the tangential viscous stress along the surface of wind waves. By looking at instantaneous surface vorticity, Veron et al. (2007) found direct evidence of airflow separation over young wind waves. These results may have important consequences for surface-drag calculations over the ocean (Sullivan and McWilliams, 2010). Recently, Grare et al. (2013b), using single point probes, were able to estimate viscous stress in the air above laboratory wind-generated waves, and suggested an important relative contribution of viscous stress with respect to the total air-water momentum flux. Unfortunately, such single point measurements do not provide a full along-wave picture of the structure of the airflow.

To conclude on past contributions and motivate the work presented in this dissertation, it can be noted that, in spite of numerous field measurements and efforts

to parameterize the drag coefficient at the ocean surface as a function of measured wind and wave characteristics, current parameterizations fail to produce satisfying predictions, especially at high wind speeds. This is problematic for hurricane intensity forecasting, sea state prediction, and global climate modeling. A crucial component of the total momentum flux across the wavy ocean surface is probably attributed to wave generation and growth. Based on a large set of laboratory and field data, Melville and Fedorov (2015) have recently shown that Miles' theory is able to predict wave growth rates reasonably well. However, direct evidence of the physics that control the distribution of momentum fluxes at the ocean surface still remains to be given.

1.2 Outline of this Dissertation

From the discussion above, it is clear that detailed investigations of the turbulent structure of the airflow above wind waves are needed. In this dissertation, we present high resolution two-dimensional measurements of the airflow above waves, obtained in the laboratory and in the field, using a complex experimental system specially developed for this study.

Chapter 2 describes in detail the different components of the complex experimental apparatus, and the methods used to acquire and analyze the data. The measurement system was developed and deployed in the large wind-wave facility at the Air Sea Interaction Laboratory of the University of Delaware, in Lewes, Delaware. The acquired data were of two types: (1) two-dimensional high resolution PIV (Particle Image Velocimetry) measurements in the air above waves, and (2) spatial and temporal wave field data. The combination of these methods allowed to not only understand the instantaneous turbulent structure of the airflow above waves, but also compute time averages, and phase averages (conditional averaging with respect to wave phase) of relevant quantities.

Chapter 3 presents the results of laboratory experiments on the turbulent structure of the airflow above wind-generated waves, for a range of very low to high wind speeds. Direct surface viscous stress and vorticity measurements are presented, and

the influence of airflow separation is discussed. It was found that, with increasing wind speed, the frequency of intermittent airflow separation events increases, while the importance of viscous stress with respect to the total momentum flux decreases.

Chapter 4 compares the airflow structure above waves covering a wide range of wave ages. The range of wave ages was extended in the laboratory, by blowing wind over mechanically generated swells. The results show three distinct regimes in the airflow, dependent upon the wave age: a sheltered, a critical layer, and a wave-driven regime.

Appendix A discusses the momentum balance, and the effect of coordinate transformation on the partitioning of the total momentum flux.

Appendix B presents preliminary results from a field experiment. A research platform, "R/P *Cheval Blanc*", was developed specifically to obtain high resolution two-dimensional velocity field measurements in the airflow above waves in the Delaware Bay, using PIV. Surface vorticity results begin to confirm the applicability of the laboratory measurements to the field.

Finally, in Appendix C, we show preliminary results from duration-limited wind wave generation experiments, performed in the laboratory at a 10-m fetch. We discuss the instantaneous structures in the airflow, that are coupled with the water surface, during the early stages of wave generation.

Chapter 2

METHODS AND EXPERIMENTAL PROCEDURES

The experiments presented here were conducted in the large wind-wave-current tank at the Air Sea Interaction Laboratory of the University of Delaware, in Lewes, Delaware. The tank is specifically designed and equipped for studies in air-sea interactions. The tank is 42 m long, 1 m wide and 1.25 m high. During the experiments described in this study, the water depth was kept at 0.70 m. An artificial permeable-type wave-absorbing beach was placed at the end of the tank to dissipate wave energy and eliminate wave reflections. The tank is equipped with a programmable, computer-controlled, recirculating wind tunnel, which, for this study, generated 10-m equivalent wind speeds ranging from 0.86 to 16.63 m s^{-1}. A honeycomb flow straightener, placed at the location of zero fetch, was used to condition the airflow before it reached the test section of the tank. In some cases, the wind speeds were combined with larger swells, generated by a plunging wedge mechanical wave maker; in other cases, the waves were solely wind-generated. The mechanical wave maker was specifically overhauled and upgraded for this study. In addition, the transfer function of the wave maker-wave tank system was measured, and the wave maker was thus made capable of generating spilling and plunging breaking waves, using the dispersive method developed by Rapp and Melville (1990). For this particular study however, the wave generator produced sinusoidal waves with frequencies ranging from 0.5 to 1.2 Hz. Mean experimental conditions are listed in Table 2.1. Figure 2.1 shows a sketch of the tank, and the location of the instrument setup, positioned at a fetch of 22.7 m. The fetch is defined as the distance from the point where the wind tunnel reaches the water, to the center of the imaging area. A complex imaging system was specifically developed for this study, and was able to measure velocities in the air above waves, on average as close as 100

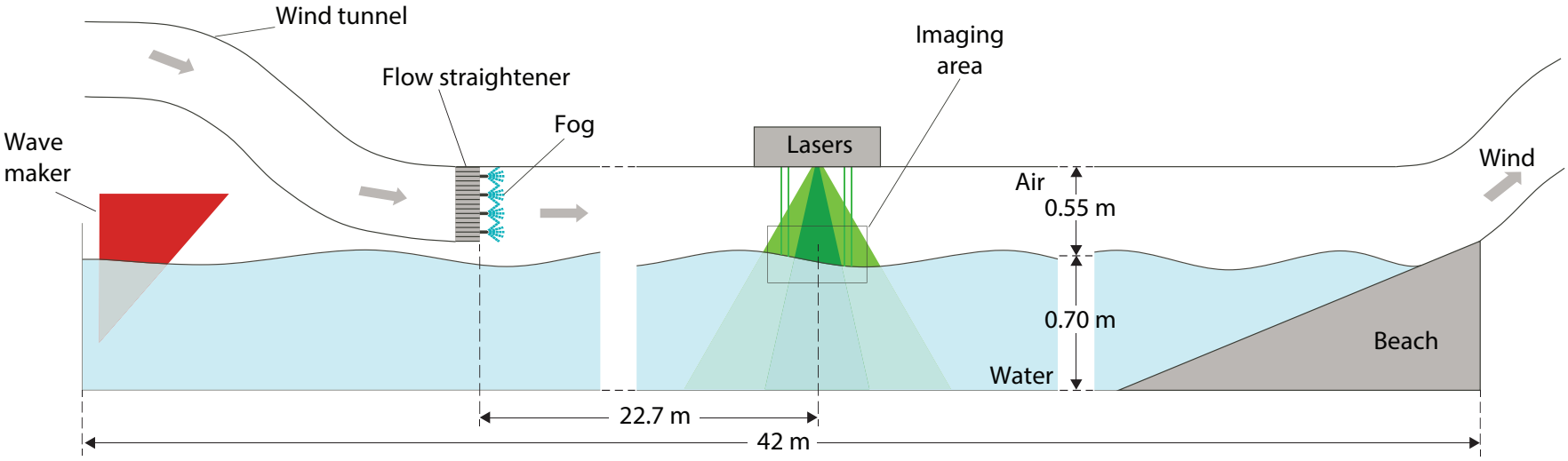

Figure 2.1: Sketch of the large recirculating wind-wave-current tank at University of Delaware's Air Sea Interaction Lab. The location of the experimental setup is shown. The center of the imaging area is located at a fetch of 22.7 m. The airflow is conditioned (airflow straightener) and seeded (fog) at the location of zero fetch.

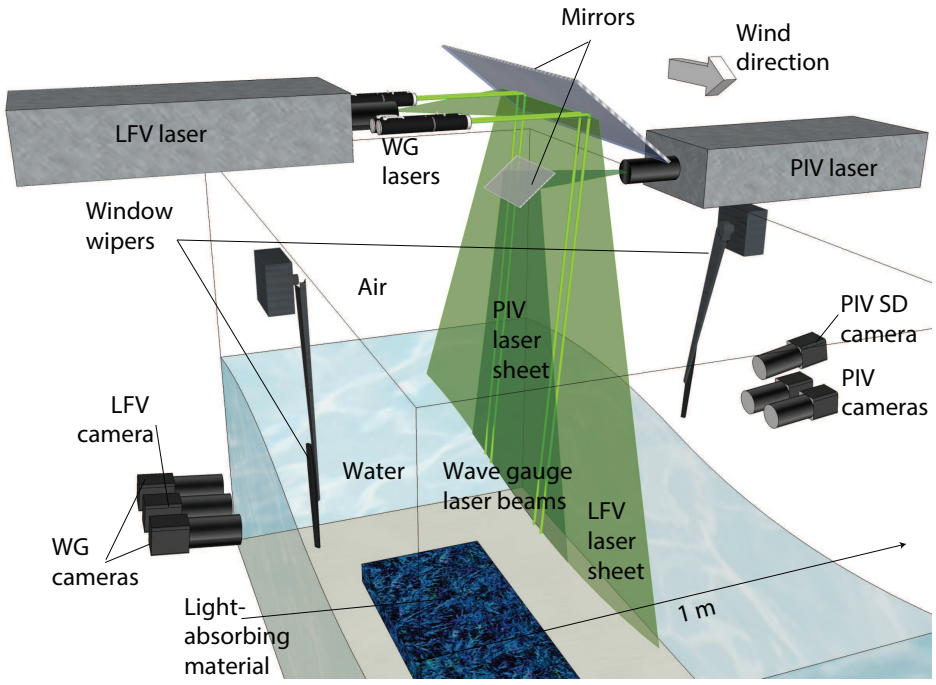

Figure 2.2: 3D sketch of the wind/wave imaging system, positioned at a fetch of 22.7 m. The airflow velocity measurement system is on the right-hand side. It is a combination of particle image velocimetry (PIV, velocity measurements) and laser-induced fluorescence (PIVSD, surface detection on the PIV images). Both make use of the PIV laser sheet for illumination. The PIV uses direct laser light reflection on the fog particles; the PIVSD uses fluorescence of the rhodamine 6G present in the water. The wave field measurement system is on the left, and consists of a large field of view spatial wave profile imager (LFV), and four single point laser wave gauge systems (WG). Both LFV and WG are using laser-induced fluorescence.

μm above the air-water interface, using a combination of Particle Image Velocimetry (PIV) and Laser Induced Fluorescence (LIF) techniques. In addition to wind velocities, temporal and spatial wave properties were measured by LIF, simultaneously with the velocity measurements. A 3-dimensional sketch of the instrument setup is presented in figure 2.2, and photos are shown in figure 2.3.

Figure 2.3: Photos of the imaging system, capable of measuring simultaneously airflow velocities up to 100 μm away from the water surface (2D PIV/PIVSD), spatial wave profiles (LFV), and water height time series (WG). (a) Downwind top view of the system, positioned 22.7 m downwind of the wind input. (b) Right top view of the system, with the 2 pairs of continuous WG laser beams (green), located respectively upwind and downwind of the PIV imaging section. (c) Left downwind view of the LFV and WG camera and LFV laser setup. (d) Right downwind view of the system. (e) WG and LFV cameras. (f) PIV and PIVSD cameras.

Table 2.1: Summary of mean experimental conditions. For each experiment, the friction velocity u_* and 10-m extrapolated velocity U_{10} were computed by fitting the logarithmic part of the mean PIV velocity profile in the air. Peak wave frequencies f_p were obtained from laser wave gauge frequency spectra (WG). Other parameters with subscript p were derived by applying linear wave theory to f_p. The root-mean-square amplitude a_{rms} was computed from the WG water surface elevation time series.

	C_p/u_*	C_p/U_{10}	u_* (cm s^{-1})	U_{10} (m s^{-1})	C_p (m s^{-1})	a_{rms} (cm)	λ_p (m)	$a_{rms}k_p$	f_p (Hz)
No waves	n/a	n/a	2.6	0.86	n/a	n/a	n/a	n/a	n/a
Wind waves	1.4	0.06	67.2	16.63	0.92	2.29	0.54	0.27	1.7
	1.6	0.06	53.8	14.34	0.87	1.96	0.48	0.26	1.8
	2.5	0.08	31.4	9.41	0.78	1.20	0.39	0.19	2.0
	3.7	0.12	16.7	5.00	0.62	0.50	0.25	0.13	2.5
	6.5	0.22	7.3	2.19	0.47	0.15	0.14	0.07	3.3
Wind over mechanical swell	6.4	0.23	20.3	5.60	1.30	2.72	1.08	0.16	1.2
	7.5	0.25	17.2	5.16	1.30	1.43	1.08	0.08	1.2
	16.1	0.52	8.1	2.48	1.30	1.36	1.08	0.08	1.2
	18.1	0.56	7.2	2.32	1.30	2.02	1.08	0.12	1.2
	19.1	0.57	6.8	2.30	1.30	2.63	1.08	0.15	1.2
	25.7	0.83	7.6	2.36	1.95	2.73	2.44	0.07	0.8
	27.7	0.93	4.7	1.40	1.30	2.63	1.08	0.15	1.2
	31.7	0.97	4.1	1.34	1.30	2.00	1.08	0.12	1.2
	38.6	1.28	8.1	2.44	3.12	2.72	6.25	0.03	0.5
	47.3	1.45	4.1	1.35	1.95	2.74	2.44	0.07	0.8
	66.7	2.15	4.7	1.45	3.12	2.73	6.25	0.03	0.5

Table 2.2: Specifications of the imaging devices. The following abbreviations are used in the table below: CCD: charged coupled device, FOV: field of view, FPS: frames per second, $\eta(x, t_0)$: along-channel instantaneous surface profile, $\eta(x_0, t)$: single-point surface elevation time series, NOF: total number of frames acquired.

Camera name	PIV (#1)	PIV (#2)	PIVSD	LFV	WG1	WG2
Technique	PIV	PIV	LIF	LIF	LIF	LIF
Model	RM-4200	RM-4200	RM-4200	RM-4200	CV-M2	CV-M2
CCD (pixel x pixel)	2048 x 2048	2048 x 2048	2048 x 2048	2048 x 2048	300 x 1600	300 x 1600
Resolution (μm/pixel)	47	47	100	250	66	66
FOV (cm x cm)	9.63 x 9.63	9.63 x 9.63	20.48 x 20.48	51.20 x 51.20	1.98 x 10.56	1.98 x 10.56
FPS	14.4	14.4	14.4	7.2	93.6	93.6
Lens size (mm)	105	105	50	14	60	60
Amber filter	no	no	yes	yes	yes	yes
Data type	velocities	velocities	$\eta(x, t_0)$	$\eta(x, t_0)$	$\eta_0(t)$, $\eta_1(t)$	$\eta_2(t)$, $\eta_3(t)$
NOF	115,314	115,314	115,314	57,657	749,541	749,541

The specifications of all imaging devices are listed in table 2.2. Additional details are provided in the following sections.

2.1 Particle Image Velocimetry Measurements of the Airflow above Waves

We developed a PIV system, capable of measuring along-channel 2D velocity fields in the air above wind waves. For this, the airflow was seeded with 8 to 12 μm water droplets generated by a commercial fog generator (Microcool Inc.) equipped with 28 fog nozzles, affixed to the airflow straightener at the location of zero fetch. In the PIV technique, small particles seed the flow and act as near Lagrangian tracers that are then illuminated with a flashed light source and imaged with a digital camera. The motion of the particles between two flashes then yields a local velocity estimate. The Stokes number for the tracer particles was found to be $O(0.01)$, which yielded a RMS tracking error below 1% (Raffel et al., 2007). The particles were illuminated by a high intensity green laser sheet (532 nm), generated by a pulsed dual-head Nd-Yag laser system (New Wave Research, 200 mJ/pulse, 3-5 ns pulse duration), fitted with a series of cylindrical and spherical lenses (Dantec Dynamics, Light Sheet Optics, visible in the bottom right corner of figure 2.3b). It should be noted that each Nd-Yag laser system is actually internally composed of two pulsed lasers. The output beams of both internal lasers are aligned such that their optical paths are quasi-identical, once outside the laser head. Each laser can flash at a frequency of up to 15 Hz. The two lasers can be flashed simultaneously, or with a time delay Δt. For PIV, Δt is generally adjusted such that particle displacement lengths are optimal on the PIV images. This time delay depends on the flow velocity and the size of the image detected (Raffel et al., 2007). In this study, the adjustable laser sheet thickness was set to approximately 0.3 cm, in order to provide crisp, in focus, high resolution images of the PIV particles (see the example image in panel a of figure 2.5 later).

The particles illuminated by the green flashed laser were imaged by two side-by-side (JAI PULNIX, 2048 x 2048 pixel) CCD cameras (bottom two cameras in figure 2.3f). Each of these PIV cameras was fitted with a 105 mm telephoto lens (Nikon).

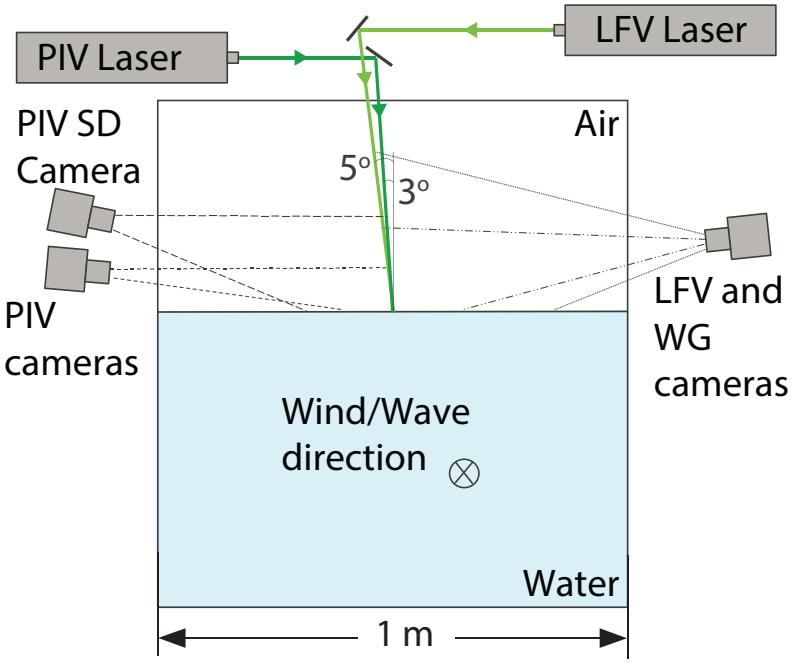

Figure 2.4: Upwind view of the imaging system. The positions of the pulsed Nd-Yag laser sheets are shown. The upper and lower limits of the camera optical paths are also sketched. The camera and laser sheet angles were optimized for maximum measurement quality.

The adjacent PIV frames were stitched together in order to obtain a high resolution (47 μm/ pixel) 18.7 x 9.6 cm PIV image, which was then processed with final interrogation windows of 8 x 8 pixel, with 50% window overlap, yielding 1 velocity vector measurement every 188 μm^2. The PIV cameras operated at 14.4 frames/second yielding PIV velocity estimates at a 7.2 Hz rate. In order to minimize direct high intensity laser light reflections from the wavy water surface into the PIV cameras, the PIV laser sheet was slightly tilted, with an angle of 3^o with respect to the vertical. This is illustrated in figure 2.4, where the instrument setup is seen from an upwind point of view. In order to avoid the obstruction of the imaged near-surface region by other waves (this is mostly an issue for wind waves, which are not two-dimensional), all cameras were slightly tilted downward. The angle of tilt was made sufficiently large such that wave obstruction was significantly reduced, even at high wind speeds, but it was also kept sufficiently small, such that the entire imaged plane (laser sheet plane) was still fully in focus on the images. This was possible because the depth of the cameras' field of view was made large enough ($O(\sim 1\text{cm})$), by properly adjusting the camera lens apertures. In the case of the more two-dimensional mechanical waves, the tilting of the cameras also prevented any obstruction of the imaged near-surface region by the water meniscus at the glass wall of the tank. The wall meniscus problem was encountered for example by Belden and Techet (2011), who also solved it by tilting their PIV cameras. Finally, it should be noted that the acquired images were corrected for both lens distortions and variations in spatial resolution.

Secondary laser light reflections near the air-water interface rendered precise automated surface detection difficult on the raw PIV images. To address this surface detection issue within the PIV images, high resolution (100 μm/pixel) LIF images (PIV surface detection images, noted "PIVSD" hereafter) of the wave surface profiles within the PIV field of view were acquired simultaneously with the PIV images, using another (JAI PULNIX, 2048 x 2048 pixel) CCD camera (top camera in figure 2.3f), but the same PIV laser. The PIVSD camera lens (Nikon, 50 mm) was fitted with an amber acrylic bandpass optical filter (Kentek ACRX-BB2 optical filter, with 6.1 optical density (OD)

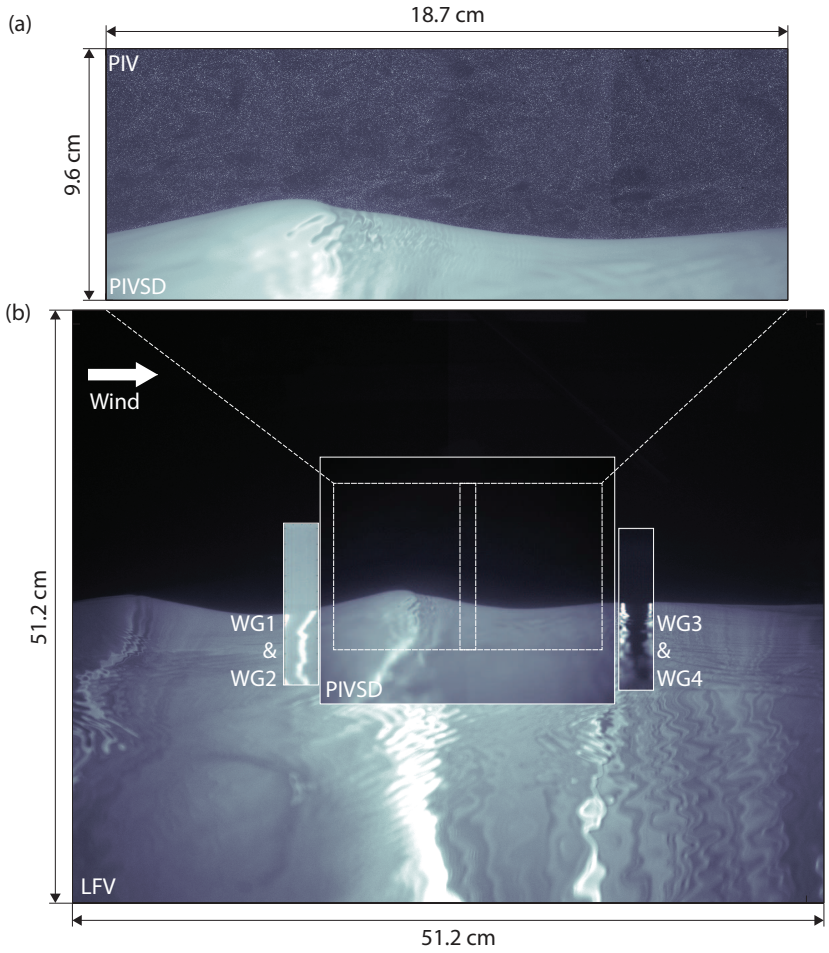

Figure 2.5: (a) Air-side portion of stitched raw PIV image, plotted above water-side portion of PIVSD image used for surface detection. The airflow is densely and uniformly seeded with fog particles. Below (b), examples of laser induced fluorescence (LIF) images are displayed, and the locations of all LIF camera fields of view are shown. Note that, since the LIF cameras are fitted with amber bandpass filters, the green-light reflecting fog particles are invisible, rendering these images ideal for automatic surface detection. All images shown here were acquired nearly at the same instant in time, with time intervals between snapshots less than 30 μs (see trigger timeline below in figure 2.6). No motions of the water surface are detectable (with an image resolution of 100 μm/pixel) within that time interval.

at 532 nm, and OD<0.6 at 566 nm). Rhodamine 6G dye (excitation at 532 nm, and maximum emission at 566 nm) was added to the water at a concentration of 8 x 10^{-6} g L^{-1}. Thus the pulsed PIV laser sheet not only illuminated the air-side PIV tracer fog particles to be imaged by the PIV cameras, but also excited the fluorescence of Rhodamine at the air-water interface, to be imaged by the LIF camera (PIVSD). Note that the amber optical filter on the PIVSD camera lens allowed the resulting PIVSD images to only show the fluorescing water (amber color), without being polluted by the reflecting PIV particles (green). A sample stitched PIV-PIVSD image is plotted in figure 2.5a.

In addition, automotive window wipers were placed in front of the cameras inside the flume in order to clean the accumulated fog off the tank windows. Special attention was given to the placement of the wipers so that they would not interfere with the airflow. Finally, light-absorbing material was placed at the bottom of the tank, under the imaging area, in order to avoid intense laser sheet light reflections back into the imaging area.

The PIV images were processed using an algorithm based on the adaptive PIV algorithm described in Thomas et al. (2005), which relies on a pyramid cascade of interrogation windows in order to achieve large dynamical range in the velocity. Subpixel resolution was obtained using a 3 point Gaussian least square fit. The PIV algorithm was run only on the portion of the image that is in the air above the instantaneous water surface. In order to achieve this, we developed a surface detection algorithm based on local variations of image intensity gradients, computed by kernel convolution. It was then applied to the PIVSD images to accurately locate the surface. Note that the PIVSD field of view extends farther upwind and downwind than the PIV field of view (see figure 2.5b). This was useful, because gradient calculations by kernel convolution can fail at the edges. This means that even in the rare cases where the surface detection algorithm failed to properly detect the surface at the edges of the PIVSD fields, the surface was still accurately determined within the PIV field of view.

2.2 Laser Induced Fluorescence Measurements of Wind Wave Properties

Two types of wave data were collected during these experiments: along-channel spatial surface profiles with high spatial resolution, and single point high frequency wave height measurements.

Large along-channel spatial profiles of the wavy surface were obtained by LIF, using a (JAI PULNIX 2048 x 2048 pixel, middle camera in figure 2.3e) CCD camera (noted "LFV" hereafter, as in "large field of view"), that was focused on the intersection with the surface of a large green laser sheet, generated by a pulsed dual-head Nd-Yag laser (New Wave Research, 120 mJ/pulse, 3-5 ns pulse duration). The LFV camera was fitted with a wide angle (115^o) lens (Rokinon, 14 mm) and an amber acrylic bandpass optical filter (Kentek, 566 nm). The resulting LFV images provided measurements of the along-wind surface elevation in the center line of the channel over a length of 51.2 cm (0.25 mm/pixel resolution), and at a rate of 7.2 Hz. The LFV field of view was positioned in the same along-channel plane as the PIV images, and extended 16.7 cm upwind and 15.8 cm downwind of the PIV field of view (figure 2.5b). Duncan et al. (1999) for example, used a similar LIF technique to study the surface profiles of mechanically generated breaking waves.

A single point optical wave gauge system, noted "WG", provided time series of the water height, respectively 2.8 and 1.4 cm upwind and 2.7 and 4.2 cm downwind of the PIV airflow velocity measurements. The system consisted of two CCD cameras (JAI 300 x 1600 pixel), each of which was fitted with a telephoto lens (Nikon, 60 mm) and an amber acrylic bandpass filter (Kentek, 566 nm). The cameras are shown in figure 2.3e, where the upwind WG camera is on the left, and the downwind one on the right. The amber lens filters are also visible, mounted on the LFV and WG cameras (as well as on the PIVSD camera, but this is not visible here). Each WG camera imaged the intersection with the surface of two 200 mW continuous green laser beams. The resulting LIF images provided measurements of the water height with a resolution of 66 μm/pixel, and at a frequency of 93.6 Hz.

2.3 Experimental Procedure

The entire imaging system was automated and computer-controlled, using National Instruments software and hardware. The triggers to all 6 cameras, the 2 pulsed Nd-Yag lasers, the 4 WG lasers, and the window wipers (see figure 2.2), were timed by PCI 6602 timing boards (National Instruments), and generated by BNC-2121 (National Instruments) connector blocks (see figure 2.7 later). A timeline of the triggers, image exposures, and laser pulses is sketched in figure 2.6. First, a LFV image was acquired, at time $t = 190$ μs. For this, excitation of both cavities within the LFV laser was initiated at $t = 0$ (Flash lamps 1 and 2). Then, at $t = 176.7$ μs, the LFV camera was triggered. This allowed the LFV laser flash to occur in the middle of the LFV camera exposure duration. Since total darkness was achieved in the laboratory, the LFV camera CCD only detected light during the LFV laser flash, that lasted 3 to 5 ns. This provided crisp sharp snapshots of the air-water interface (see figure 2.5). It can be noted that the LFV LIF imaging system only acquired one LFV image per PIV image pair, every 1/7.2 s. This means that it would have been possible to use only one cavity within the LFV laser. However, both cavities within the LFV laser were excited and flashed simultaneously in order to increase the total laser energy, and yield optimal quality LIF images. Next, the PIV (and PIVSD) images were acquired, 20 μs after the LFV images. Note here that the wavy water surface did not display any detectable displacements within this time interval. For this, the PIV laser's first cavity excitation had already been initiated at $t = 20$ μs. This allowed the laser to flash first at $t = 210$ μs, yielding the first images of a PIV pair. (A "PIV pair" here, represents actually a total of 6 images, since 2 PIV pairs and 1 PIVSD pair are acquired at each PIV laser flash.) The first PIV/PIVSD exposure was triggered 9.15 μs prior to the first PIV laser flash. The second PIV laser flash took place after a time interval Δt. Once again, since there was no other light source than the 3-5 ns laser flash, the PIV particle images were extremely sharp and in focus (see again figure 2.5a), even though the full exposure of the second PIV frame was set to 67 ms by the manufacturer. The PIV time interval Δt was adjusted for each experimental wind speed, in order to achieve

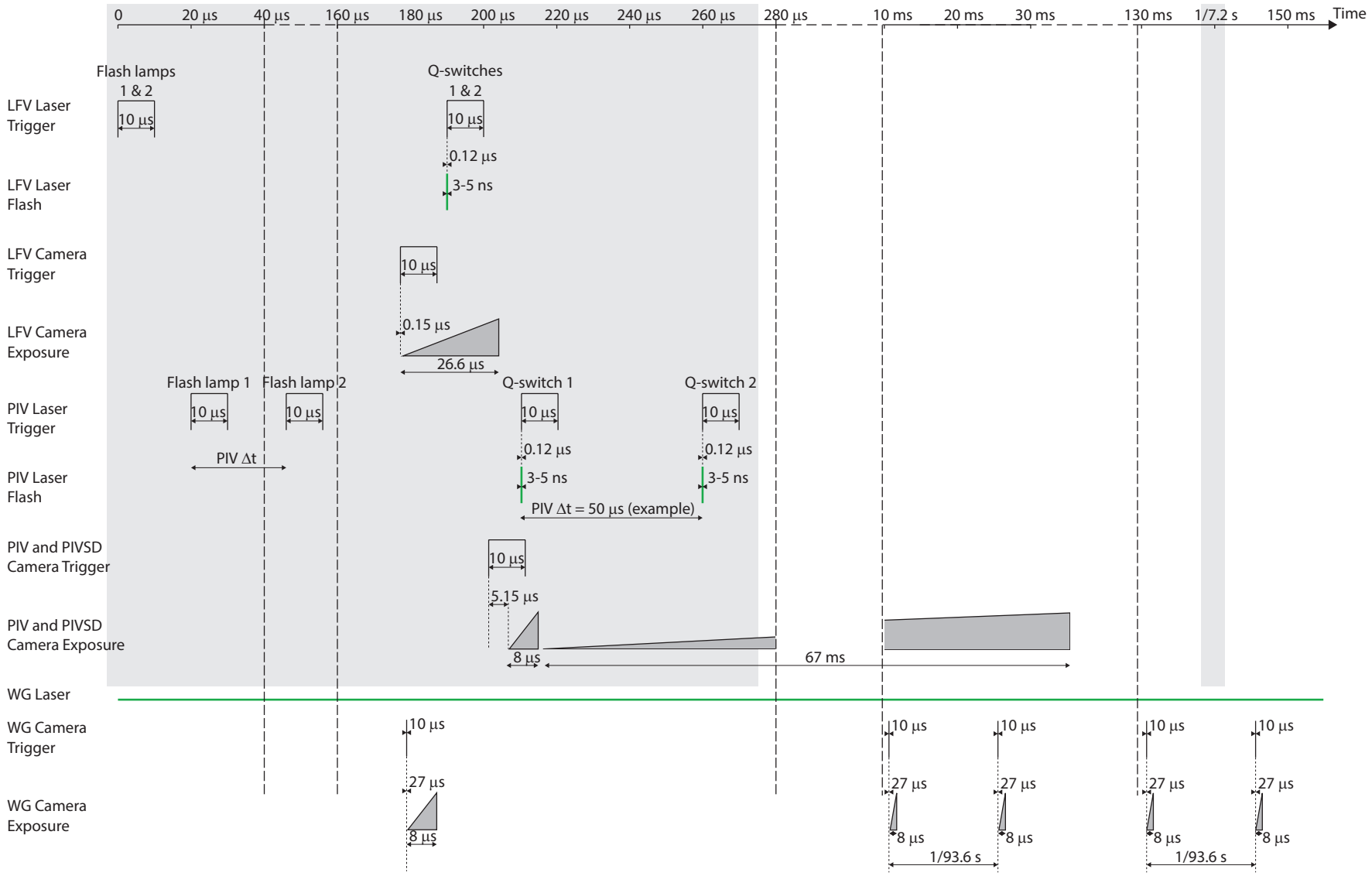

Figure 2.6: Trigger, laser flash, and image exposure timeline for the imaging system. The gray shaded region is the LFV/PIV/PIVSD imaging sequence. It is repeated at a frequency of 7.2 Hz, and takes place after every 13th WG measurement, between two consecutive WG image acquisitions (93.6 Hz).

optimal particle displacement on the PIV images for velocity vector calculation. In the meantime, the four continuous WG laser beams were on all the time. These did not pollute the PIV and PIVSD images, because the WG beams were outside of the PIV and PIVSD fields of view. They were equally undetectable on the LFV fields of view, because the LFV camera exposure time was short. The two WG cameras were simultaneously triggered at a frequency of 93.6 Hz. This particular frequency was chosen because it is an integer multiple (13) of 7.2 Hz, the PIV pair frequency. This allowed us to acquire 13 WG samples between LFV/PIV/PIVSD measurements, with no drift in the time intervals between LFV/PIV/PIVSD and WG samples. In fact the WG exposure time was kept short (8 μs), in order to optimize the WG signal resolution, and also to avoid contamination of every 13th WG image by the LFV/PIV/PIVSD laser flashes. The entire LFV/PIV/PIVSD laser flash and camera exposure sequence took place between two consecutive WG image acquisitions (gray shaded time interval in figure 2.6).

Each wind-wave experiment followed a fully automated, repeatable procedure. A data flow chart is provided in figure 2.7. At first, the wind was slowly increased to its target steady value. The experiments with mechanical swells had one additional step: the wave maker was set to generate monochromatic swells throughout the duration of the run. The wind blower and mechanical wave maker were controlled by analog signals, generated and sampled by a PCIe 6353 data acquisition board (National Instruments) coupled with a BNC-2090A connector block (National Instruments). After the wave field had sufficiently developed and reached a fetch-limited equilibrium state, the fog generator was digitally triggered (see figure 2.7) and the system acquired simultaneously PIV data, LIF PIV surface detection data, LIF large field of view data and LIF single point wave height data. During each experiment, the inside of the tank windows were dried using the window wipers every 30 s, and for a period of 3 s. The images altered by the presence of the wiper were later systematically removed from the dataset. Acquired images were transferred to hard drive striped sets by IO Industries frame grabbers. The images were then accessed through Streams 5 software

(IO Industries), and stored on a large data storage striped set. The data were later processed using Matlab (MathWorks).

For each of the 17 experiments presented here, the total number of images acquired by the imaging system ranged from 85,000 to 200,000, depending on the wind-wave conditions. In order to sample the same amount of full wave data per experiment, more data were acquired when the generated waves were longer. The results presented in this study were produced from the acquisition and processing of a total of 1,902,681 images.

2.4 Experimental Conditions

In this work, we present results for 17 different wind/wave conditions, with wave ages (C_p/u_*) ranging between 1.4 and 66.7. The different experimental conditions are summarized in Table 2.1. Experiments were performed for durations varying from 4.5 to 14 minutes, depending on the wind-wave conditions. Those durations were calculated based on the estimated dominant wavelength and wave speed for each experiment, with the objective of sampling the same number of waves (approximately 2000) per experiment. During the first experiment ($U_{10} = 0.86$ m s^{-1}), the wind did not generate any detectable waves. The mean wind profile above the flat water surface, obtained from averaging over 2 x 10^6 profiles obtained by PIV, is plotted in figure 2.8a. The mean wind profile follows the law of the wall, showing clear viscous sublayer, buffer, and logarithmic layers (e.g., Schlichting and Gersten, 2000). The fit of the logarithmic part of the mean wind profile is used to estimate values for friction velocity u_* and 10-m extrapolated velocity U_{10}.

Power spectral densities (PSD) of the water surface elevation were computed from the single point wave gauge signals. The wind wave spectra, represented in figure 2.8b, are relatively narrow-banded, with clear peaks at the dominant wave frequency f_p (reported in Table 2.1). Dominant wave frequencies decrease with increasing wind speed, as the fetch-limited waves grow longer with increasing wind speed. The PSDs increase with increasing wind speed, which indicates that the waves also increase in

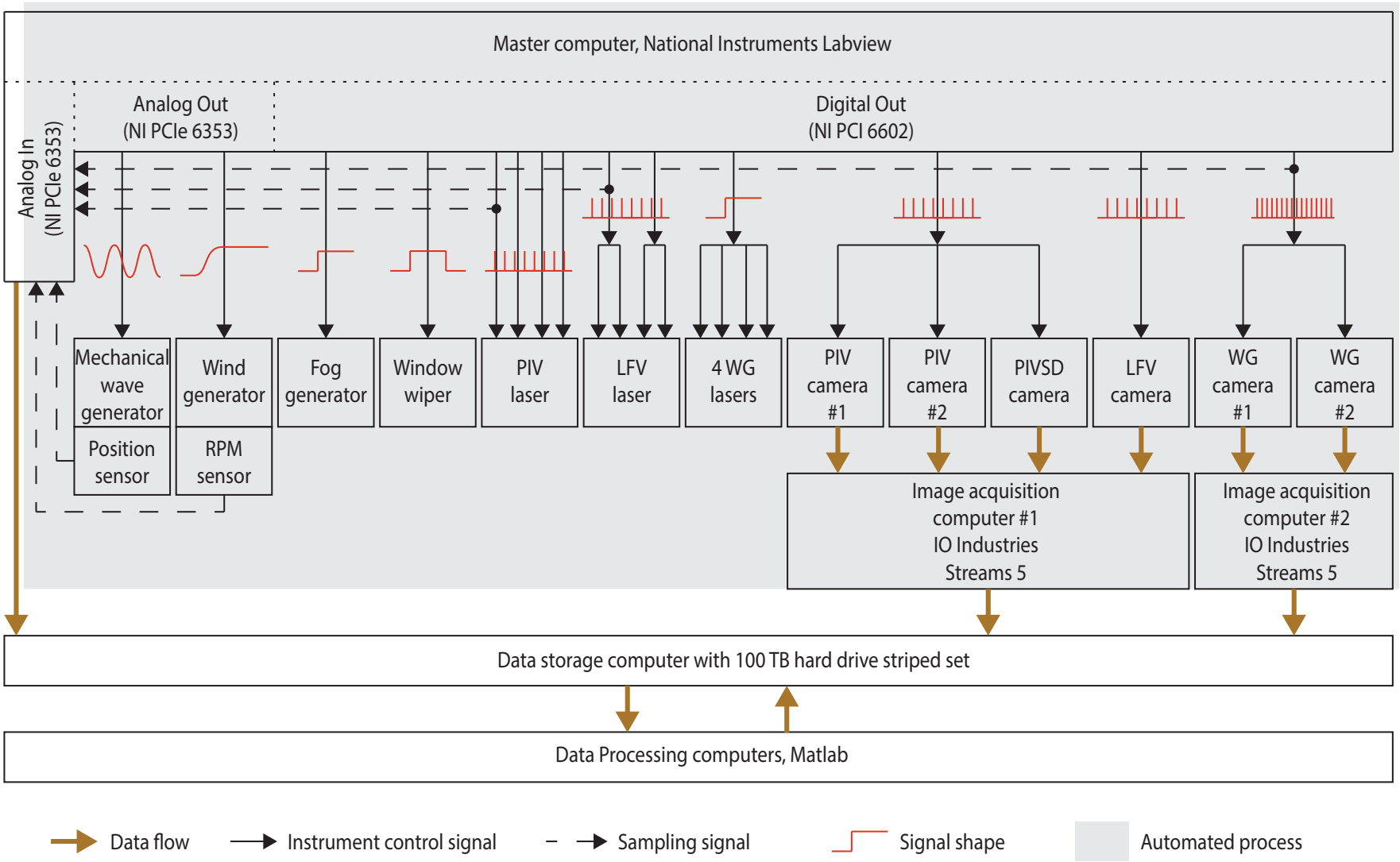

Figure 2.7: Signal and data flow chart for the wind-wave experiments. The gray shaded area represents the automated turn-key system.

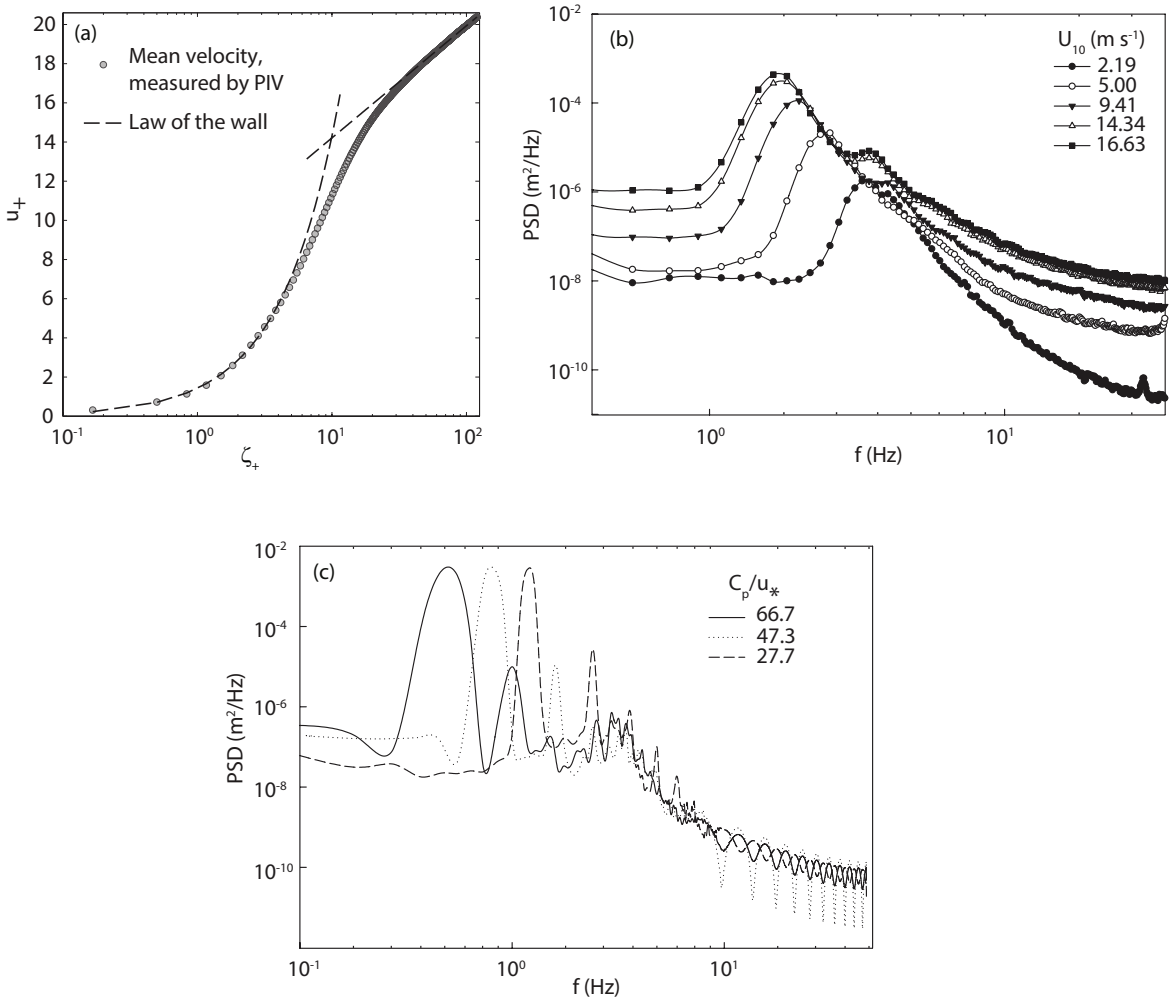

Figure 2.8: (a) Mean normalized wind profile ($u_+ = \overline{u}/u_*$, $\zeta_+ = \zeta u_*/\nu$, with ν the kinematic viscosity of air) from PIV for $U_{10} = 0.86$ m s^{-1}. Surface-following coordinate ζ is defined in section 2.5 below. Gray circles are data obtained with the PIV, dashed lines are respectively linear and logarithmic fits from the law of the wall. (b) Power spectral densities (PSD) of water surface elevation time series, measured 1.1 cm upwind of the PIV field of view (WG2), for all wind wave experiments. (c) Same as (b), but for 3 experiments with wind blowing over mechanical waves.

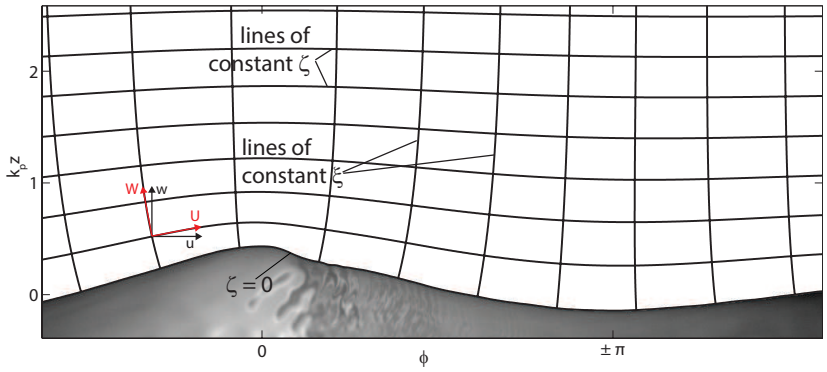

Figure 2.9: Sketch of the surface following coordinate transformation used in this study. The ζ coordinate is surface following at the surface, and decays toward the cartesian coordinate z away from the surface. $\zeta = 0$ coincides with the water surface. The ξ coordinate is orthogonal to the surface at the surface, and decays toward the cartesian coordinate x away from the surface. The abscissae are the along-wave phases ϕ, defined below in section 2.6. Measured variables u and w are respectively the horizontal and vertical (cartesian, (x, y) system) components of the velocity, and U and W are the curvilinear components ((ξ, ζ) system).

amplitude with increasing wind speed. The mechanical wave spectra, three examples of which are plotted in figure 2.8c, show peaks at the mechanically forced frequencies (0.5, 0.8, 1.2 Hz), and a number of sidebands with frequencies that are multiples of 1.2. Such harmonics are inevitable in wave-tank mechanical wave experiments (e.g., Bliven et al., 1986). In order to minimize their presence during the experiments, we limited our mechanical waves to relatively small amplitudes (see Table 2.1). The peak wave phase celerity C_p and wave length λ_p were estimated using the linear deep-water dispersion relationship. The root-mean-square wave amplitudes a_{rms} were computed using the measured water surface elevation time series (WG).

2.5 Coordinate Transformation

By using the LFV wave profiles, we were able to decompose every PIV water surface into spatial Fourier components, and derive a coordinate system that follows the surface near the surface, and tends toward the cartesian coordinate system away from

the surface. Since wind waves contain a number of different Fourier modes, the lines of constant ζ (see definition below) also contain several modes. Higher order modes (large wavenumbers) decay much faster than lower order modes, which is physically intuitive, in the sense that longer waves perturb the airflow up to a higher altitude than shorter waves do. We introduce curvilinear coordinates (ξ, ζ) related to cartesian coordinates (x, z) by:

$$\xi(x,z) = x - i\sum_n a_n e^{i(k_n\xi+\phi_n)}e^{-k_n\zeta}, \tag{2.1}$$

$$\zeta(x,z) = z - \sum_n a_n e^{i(k_n\xi+\phi_n)}e^{-k_n\zeta}, \tag{2.2}$$

where a_n, k_n and ϕ_n are respectively the amplitude, wavenumber and phase of the n-th mode in the Fourier decomposition of the water surface $\eta(\xi)$:

$$\eta(\xi) = \sum_n a_n e^{i(k_n\xi+\phi_n)}.$$

Figure 2.9 shows a sketch of the decaying surface-following grid. For clarity, only a small fraction of the grid lines are represented. Note that as we move away from the surface, high order modes such as the ripples present at the surface (grid line $\zeta = 0$) decay and disappear first, then the dominant mode decays slowly toward a horizontal line. A similar multimodal curvilinear transformation was first introduced for a wind-wave interaction numerical model by Chalikov (1978). It can be noted here that while this type of coordinate system is now somewhat frequently used in computational studies (e.g., Hara and Sullivan, 2015), experimental studies were up until now, not able to report data using such transformations.

2.6 Wave Phase Detection

Wave phase detection within the PIV field of view was achieved for wind waves by applying a Hilbert transform (Oppenheim and Schafer, 2013; Melville, 1983) directly to the LFV wave profiles. In panel a of figure 2.10, we show an example of an

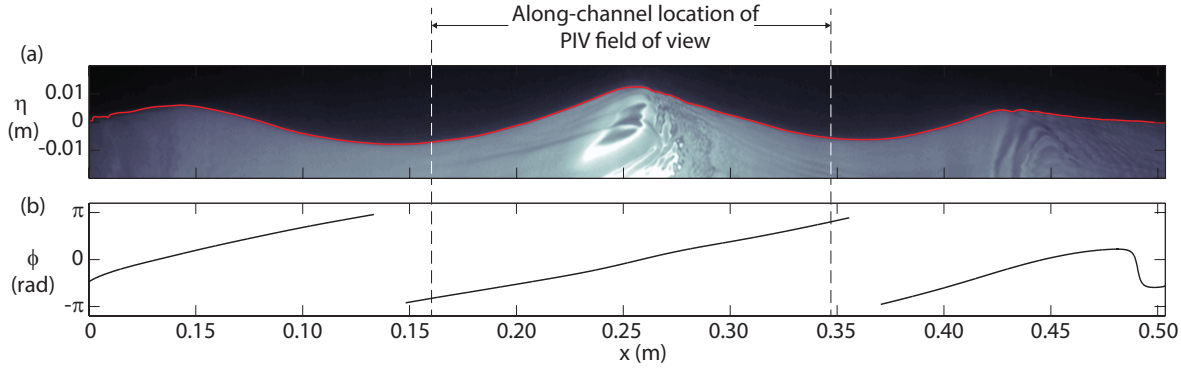

Figure 2.10: (a) Instantaneous along-channel profile of the wavy water surface (wind-generated waves), with $U_{10} = 5.00$ m s^{-1}. This profile was obtained by applying our surface detection algorithm to the large field of view LIF image (LFV), shown here in grayscale. (b) Along-surface wave phases, computed by Hilbert transform.

instantaneous LFV wave profile, extracted from the wind wave experiment with $U_{10} = 5.00$ m s^{-1}. In panel b, the corresponding phases computed by Hilbert transform are plotted. Using this method, it is apparent that at the upwind and downwind extremities of the LFV wave profile, edge effects (unavoidable in discrete Fourier analysis) render the phase information unusable. However, the phases of the wavy surface located within the PIV field of view are well detected, since they are far away from the edges of the LFV field of view.

In the case of longer swells, only a fraction of a wavelength was visible on the LFV images, rendering any Fourier/Hilbert analysis impossible. All spatial modes of the wavy surface were then neglected in the coordinate transformation except the dominant swell mode (i.e., $n \leq 1$ in equation 2.2), and wave phases were then detected by computing Hilbert transforms of the WG time series up- and downwind of the PIV field of view (WG2 and WG3), and linearly interpolating phases between WG2 and WG3 at the times matching with the PIV frame acquisitions. This method is illustrated in figure 2.11, where we show an instantaneous PIV surface (panel a), recorded at a certain instant t_0, and the corresponding sample wave gauge time series (panel b). Note that the PIV surface, since it represents only a fraction of a wavelength ($\sim 1/6$),

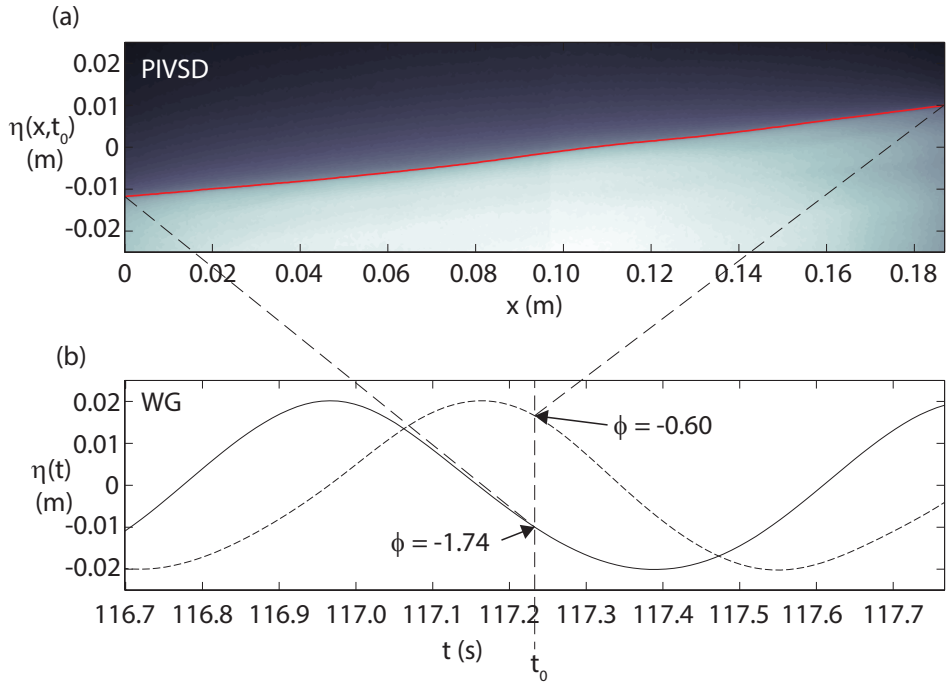

Figure 2.11: (a) Instantaneous spatial profile of a fraction of the upwind face of a mechanical wave ($C_p/u_* = 31.7$), acquired at time $t_0 = 117.2329$ s. This profile was obtained by applying our surface detection algorithm to the PIV surface detection image (PIVSD), shown here in grayscale. (b) Water surface elevation time series around t_0, extracted from the datasets acquired respectively upwind of the PIV field of view (WG1, solid line) and downwind of the PIV field of view (WG3, dashed line).

does not allow any phase detection. The wave gauge time series however, cover several thousands of wave periods, which is ideal for applying a Hilbert transform.

It is worth mentioning here that this complex imaging system is, to the best of our knowledge, the first of its kind, capable of simultaneously measuring velocities in the air, along with robust temporal and spatial wind wave and mechanical wave properties. Previous wave follower studies (e.g., Hsu et al., 1981), beyond the limitations caused by the one-dimensionality of the measurements, were also challenging due to wave follower response times, which generated uncertainty in their phase detection and in estimating the height of their measurements from the water surface. This also prevented experimentalists from getting measurements close enough to the water surface. Grare (2009); Grare et al. (2013b) were able to obtain measurements very close to the water surface by plunging their probe into the water, but this forced them to reduce the accuracy of their probe, in order to not destroy it upon submersion. Finally, we may mention here the work of Siddiqui and Loewen (2010), who, in spite of an effort to determine the phases of wind waves by linear interpolations of phases between zero-crossings, crests, and troughs of the peak waves, were limited by the difficulty to accurately detect surfaces on PIV images because of secondary laser light reflections, and by the limited size of their PIV field of view. Our combination of PIV images with simultaneous LIF PIVSD and LFV images provided robust high resolution surface and wave phase detection for the air-water interface. The phase information was used to phase average the measured and computed quantities, and decompose them into mean, phase mean, and turbulent contributions.

2.7 Triple Decomposition

A quantity q near the wavy interface can be represented as the sum of a phase average $\langle q \rangle$ and a turbulent perturbation (e.g., Hussain and Reynolds, 1970; Phillips, 1977):

$$q(x, z, t) = \langle q \rangle(\xi, \zeta) + q'(x, z, t).$$

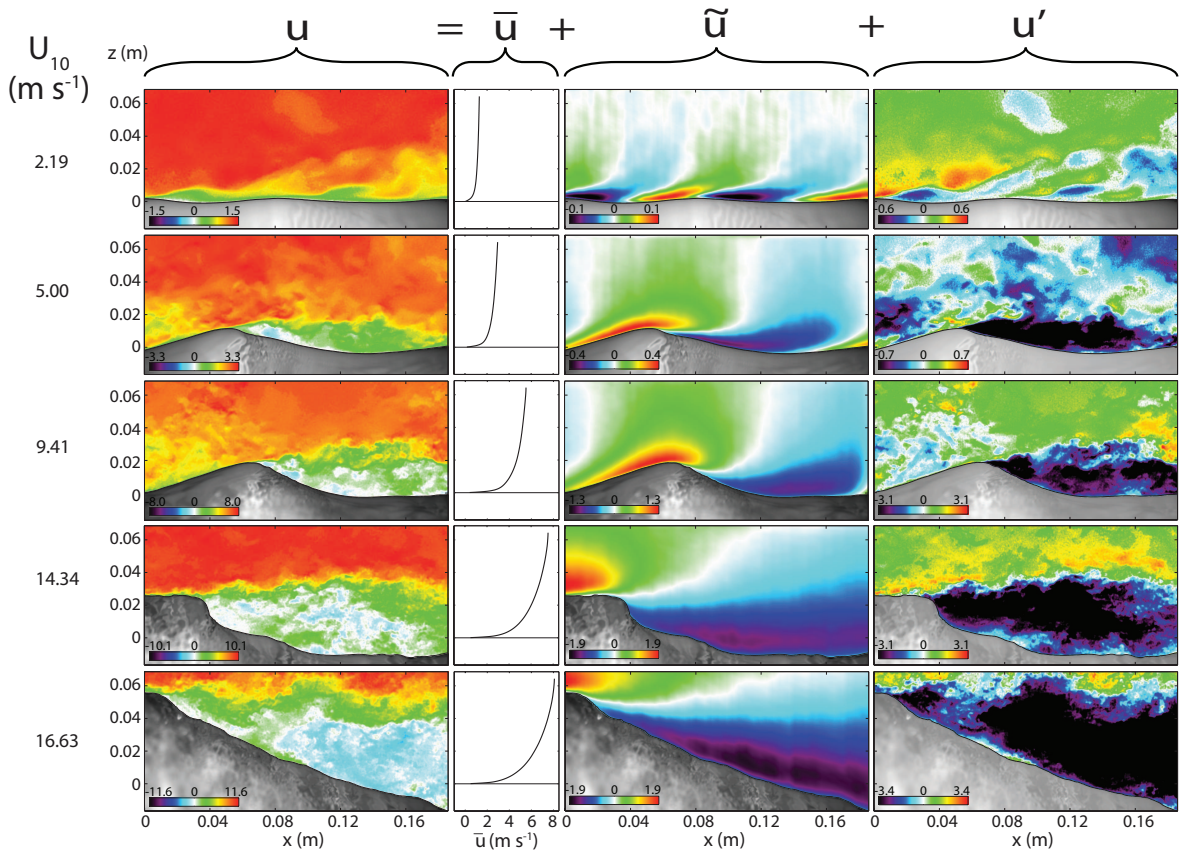

Figure 2.12: Examples of triple decomposed instantaneous velocity fields (horizontal component). Examples were extracted from 5 different wind wave experiments. All quantities are plotted in m s^{-1}. Each line corresponds to a different wind speed (in increasing order), with the wind speed written on the left of each line.

Proper phase detection and subsequent conditional averaging (by phase bin) yields directly $\langle q \rangle$. Turbulent quantities are then obtained by subtracting $\langle q \rangle(\phi)$ from instantaneous profiles at phase ϕ. In this study, wind wave phases were binned into 144 bins, each covering a phase interval of 4.36 x 10^{-2} rad, and mechanical wave phases were sorted into 72 bins of width 8.72 x 10^{-2} rad. The phase averaged quantity $\langle q \rangle$ can be further decomposed into the sum of a phase independent mean $\overline{q}$ and a wave-coherent perturbation $\widetilde{q}$. This leads to the following triple decomposition:

$$q(x, z, t) = \overline{q}(\zeta) + \widetilde{q}(\xi, \zeta) + q'(\xi, \zeta, t) \tag{2.3}$$

It should be noted that in order to define $\overline{q}$ near the wavy boundary, it is necessary to use a wave-following coordinate system, such as the one defined above. Otherwise, $q(z)$ at a fixed height z less than the wave amplitude, is alternatively in the air and in the water. Equation 2.3 is illustrated in figure 2.12, where instantaneous horizontal velocity fields are decomposed into the sum of a mean velocity profile, a wave-coherent, and a turbulent velocity field. The velocity fields u are a direct output of the PIV processing (described at the end of section 2.1). The wave perturbation velocities $\widetilde{u}$, which are mean wave phase coherent values, are plotted here over the instantaneous wave profiles. This can be achieved by plotting each phase dependent wave perturbation profile $\widetilde{u}(\phi, z)$ above the section of the instantaneous wavy surface that has the same phase ϕ. The turbulent fields u' are then computed by subtracting both the $\widetilde{u}$ fields and $\overline{u}$ profiles, from instantaneous fields u. Finally, it should also be noted that the instantaneous fields shown in figure 2.12 are not "best picks"; they were chosen because they give a representative picture of the dynamics upwind and downwind of crests, above waves at the peak of the spectrum. Additional details on these dynamics are provided in the following chapters.

Chapter 3

AIRFLOW STRUCTURE AND WIND STRESS ABOVE LABORATORY WIND WAVES, AND INFLUENCE OF AIRFLOW SEPARATION

3.1 Introduction

The dynamics in the airflow above wind-generated waves are crucial for wind-wave coupling and for the air—sea momentum flux as a whole. Detailed investigations of the airflow structure and wind stress above wind waves are rare, because of the technical challenges involved with acquiring high resolution measurements very close to a rapidly moving interface. However there is a need for such measurements, because for example, momentum flux parameterizations still need to be improved at high wind speeds (e.g., Edson et al., 2013), in order to help better predict extreme weather events such as hurricanes. At high wind speeds, when waves break, airflow separation is believed to have an important impact on the total momentum flux. The details of airflow separation above wind waves are largely unknown. Until now, only qualitative characterizations of the phenomenon have been achieved (e.g., Kawai, 1981), with the exception of Veron et al. (2007). In addition, a number of experimental studies were performed over mechanically generated waves (e.g., Hsu et al., 1981; Reul et al., 1999), where waves are not in local equilibrium with the wind. Recently, Grare et al. (2013b) presented single point measurements above laboratory wind waves very close to the surface. However single point probes provide only limited information on the three-dimensional structure of the airflow, and its interactions with the three-dimensional wavy surface. In this chapter, using the complex imaging system described in chapter 2, we present two-dimensional high resolution results on the instantaneous structure of the airflow above wind-generated waves. We further investigate mean and phase averaged

motions and stresses, and estimate the different contributions to the momentum flux across the air-water interface. Finally, the impact of airflow separation on the average surface viscous stress is assessed. Six experiments are considered in this chapter (lines 1 through 6 in table 2.1, chapter 2). During these experiments, waves were solely generated by winds, with mean 10-m wind speeds respectively $U_{10} = 0.86$, 2.19, 5.00, 9.41, 14.34, and 16.63 m s^{-1}. The data were collected at a fetch of 22.7 m.

3.2 Instantaneous Airflow Structure

3.2.1 Airflow separating waves and non-airflow separating waves

In figure 3.1, we show instantaneous kinematic fields in the airflow above two different waves, that were sampled 35 s one after the other, during the same wind wave experiment ($U_{10} = 5.00$ m s^{-1}). The wave on the left, with a slope of $ak = 0.29$, has a relatively sharp crest and a flat trough, as well as what appear to be parasitic capillary waves just downwind of the crest. The wave on the right is comparatively smoother, more sinusoidal, and less steep ($ak = 0.14$).

Above the crest of the steep wave, the airflow moves very fast throughout the entire height of the sampled air column, and the streamwise velocity only decreases very near the surface (figure 3.1a). This suggests that, over the crest, the turbulent boundary layer is very thin, and the near surface shear is large. In aerodynamics, turbulent boundary layer thinning is known to occur in a similar fashion in favorable pressure gradient conditions, caused for example by the presence of an airplane wing or a hill in the airflow (Baskaran et al., 1987; Simpson, 1989). Just past the wave crest, the air boundary layer appears to detach from the water surface, and the near surface streamwise velocity drops dramatically. We observe a region of negative velocity near $\phi = \pi/4$, which indicates that the crest of the wave is completely sheltering this region from the wind, and that the airflow within the sheltered region recirculates. The vertical velocity field w/U_{10} (figure 3.1c) does not provide clear evidence of flow separation, but is not incoherent with the hypothesis of separated sheltering. It should be noted that in general, the instantaneous vertical velocities in a turbulent boundary

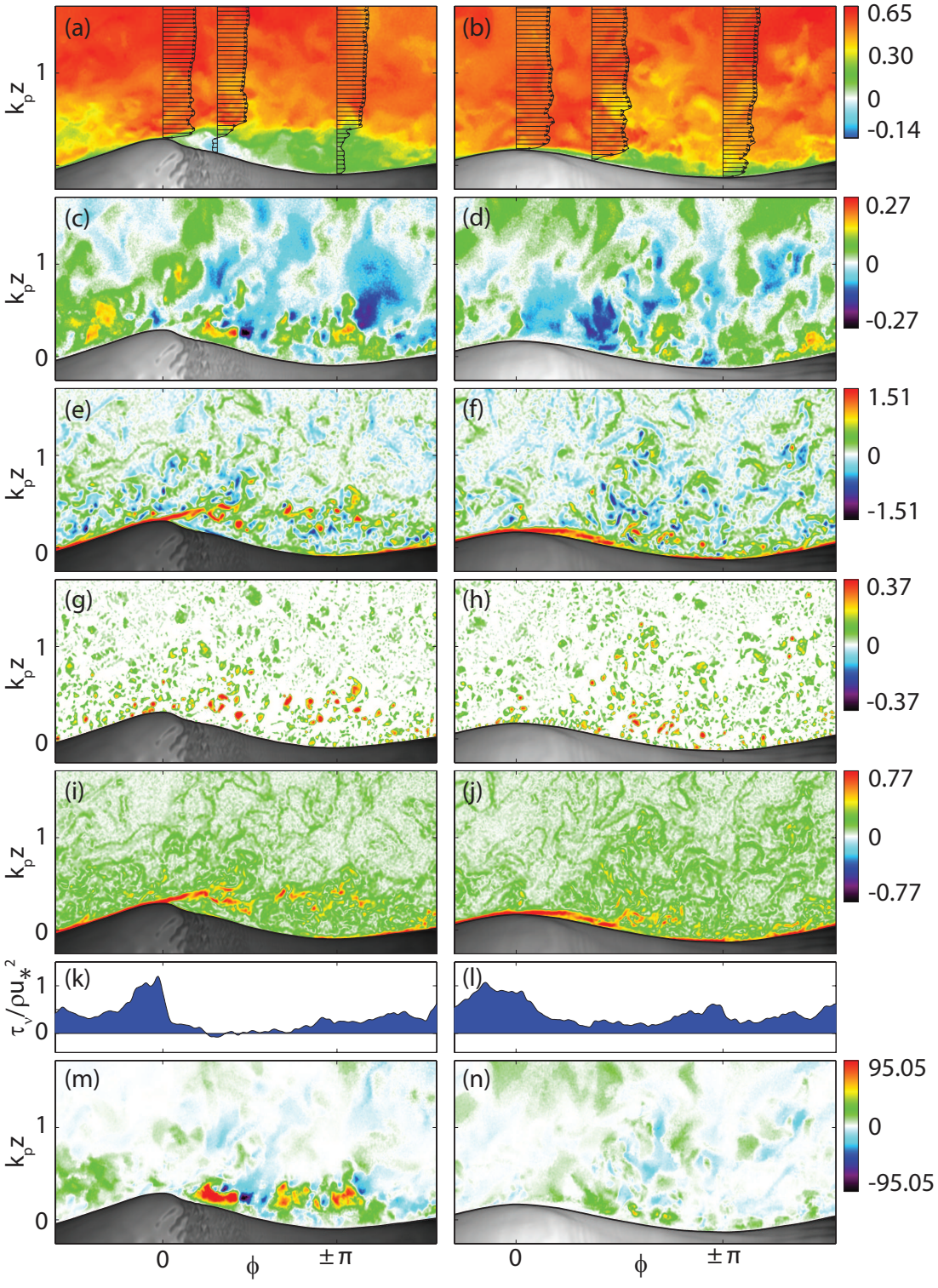

Figure 3.1: Instantaneous fields over an airflow separating wind wave (left) and a non-separating wind wave (right), with $U_{10} = 5.00$ m s^{-1}. (a,b) Horizontal velocity component u/U_{10}; (c,d) Vertical velocity component w/U_{10}; (e,f) Vorticity $\omega/(u_*^2/\nu)$; (g,h) Swirling strength $\lambda_{ci}/(u_*^2/\nu)$; (i,j) Shearing strength $\gamma_s/(u_*^2/\nu)$; (k,l) Surface viscous stress $\tau_\nu/\rho u_*^2$; (m,n) Turbulent stress $-u'w'/u_*^2$.

layer can be assimilated to turbulent velocities, because the mean vertical velocity is zero. Here, the presence of waves complicates the definition of turbulence, such that the vertical velocities are a result of both wave-induced and pure turbulent perturbations (see triple decomposition in section 2.7 in chapter 2). Upwind of the crest, the airflow is significantly forced upward near the surface (wave effect, see phase averaged velocities later in section 3.4). Past the crest, near $\phi = \pi/4$, the airflow moves upward near the surface, then back downward near $\phi = \pi/2$ and continues to vary significantly above the wave trough (figure 3.1c). These variations are now probably turbulent, and are coherent with the separated sheltering hypothesis, which suggests the presence of recirculations past the point of separation (e.g., Simpson, 1989). The vorticity field, plotted in figure 3.1e, confirms quite unequivocally the conjecture that the airflow is separating past the crest of the wave. The layer of high positive spanwise vorticity (mostly due to shear, see below), attached to the surface on the windward side of the wave, completely detaches from the surface past the crest of the wave. This (now free) high vorticity layer then appears to oscillate (near $\phi = \pi/4$), and break up into small centers of high (now essentially vortical, see below) vorticity. The oscillations of the unstable free shear layer past the wave crest are reminiscent of Kelvin-Helmholtz type instabilities. The vortices that are shed past the crest show signs of vortex pairing or "roll-up" (for example just past $\phi = 3\pi/4$). Vortex production and "roll-up" are known to occur in perturbed free shear layers (e.g., Winant and Browand, 1974; Ho and Huang, 1982; Ho and Huerre, 1984). We may also note here that there is absolutely no positive vorticity below the flow-reversal sheltered region, but rather slightly negative spanwise voriticity, which is coherent with a reversed airflow in that region.

In order to distinguish between vortical vorticity and shear-related vorticity, we show estimates of the "swirling strength" λ_{ci} (Zhou et al., 1999) and the shearing strength γ_s, respectively in panels g and i of figure 3.1. The "swirling strength" was suggested by Zhou et al. (1999) to be a measure of the strength of the local swirling motion, and is defined as the imaginary part of the complex eigenvalue of the velocity

gradient tensor:

$$\lambda_{ci} = \mathrm{Im}\left\{\frac{1}{2}\left[\frac{\partial u}{\partial x}+\frac{\partial w}{\partial z}-\sqrt{\left(\frac{\partial u}{\partial x}+\frac{\partial w}{\partial z}\right)^2-4\left(\frac{\partial u}{\partial x}\frac{\partial w}{\partial z}-\frac{\partial u}{\partial z}\frac{\partial w}{\partial x}\right)}\right]\right\}.$$

Here, in figure 3.1g, we observe centers of intense positive spanwise swirling strength predominantly past $\phi = \pi/4$, which is where the detached high vorticity layer begins to lose coherence. This confirms that the observed centers of high vorticity (figure 3.1 panel e) are due to vortical motions.

To estimate the importance of shearing motions in the airflow, the "strength of anisotropic stretching", written by Zhang et al. (2009) as

$$\gamma_s = \frac{1}{2}\sqrt{\left(\frac{\partial u}{\partial x}-\frac{\partial w}{\partial z}\right)^2+\left(\frac{\partial u}{\partial z}+\frac{\partial w}{\partial x}\right)^2},$$

is plotted in figure 3.1i. A thin layer of high γ_s, is present along the windward face of the wave, detaches from the crest, and extends up to $\phi = \pi/4$. The existence of this high γ_s layer, combined with the absence of significant swirling strength along that layer, suggests that the vorticity is essentially shear related, when it is still in layer form. Past $\phi = \pi/4$, downwind of the now disintegrated free shear layer, a number of vortices and small high shear structures populate the turbulent boundary layer. Then, just before $\phi = \pi$, a high shear layer is gradually regenerated at the surface, indicating a gradual restoration of the surface-attached airflow.

Over the smoother more sinusoidal wave (right hand side of figure 3.1), the picture is different. The airflow does not dramatically separate from the surface, as it did over the steeper wave. The boundary layer does however begin to thicken past the crest, and low velocity fluid is ejected away from the surface starting at a phase of $\phi = \pi/2$ (figure 3.1b). In fact, the velocity profiles throughout the sampled air column show minimal fluctuations above the crest, and even some distance past the crest, whereas past $\phi = \pi/2$ and above the trough, a turbulent mix of low velocity and higher velocity air extend from the surface up to a height of at least $k_p z \sim 1$. Thus, the

boundary layer tends to be thinner and less turbulent above the crest (similarly to the case of the steeper wave crest on the left), and then thickens past the crest, without any clear separation of the airflow. The instantaneous vorticity field, plotted in figure 3.1f, also shows a gradual thickening of the surface vorticity layer (positive spanwise vorticity) past the crest (note also the thickening of the surface shearing strength layer in panel j), which is coherent with boundary layer thickening (Wu et al., 2006). Then, we observe an ejection of vortical structures away from the surface (near and past $\phi = \pi/2$, see also the swirling strength in panel h of figure 3.1). In this case however, the surface vorticity does not vanish as it does in the separated case. The turbulent airflow here does not separate from the surface. This burst of vorticity and low velocity fluid away from the surface is rather reminiscent of "Q2" type events, that have been directly observed in turbulent boundary layers over flat plates (e.g., Kline et al., 1967; Adrian, 2007). In turbulent boundary layers over solid boundaries, Q2 and Q4 events are generally attributed to the existence of quasi-streamwise vortical structures and vortex "hairpins" (e.g., Adrian, 2007). Quasi-streamwise vorticity can suddenly bring low velocity fluid upward ($u' < 0$ and $w' > 0$, called Q2 events or ejections) and bring high velocity fluid downward ($u' > 0$ and $w' < 0$, Q4 events or sweeps). Since in both cases, the product $u'w'$ is negative, Q2 and Q4 events are downward turbulent momentum flux events. These have been suggested to be an important contributor to downward turbulent momentum flux across the ocean surface, in young wind-wave conditions (Sullivan and McWilliams, 2010). Further information on these is given in a more detailed along-wave quadrant analysis in section 3.4.3 below. It should also be noted here that the alternating thinning and thickening of the turbulent boundary layer above waves, without airflow separation, was predicted and modeled by Belcher et al. (1993), who introduced it under the term "non-separated sheltering". After considering the implications of this mechanism for the along-wave turbulent pressure distribution (which, when correlated with the wave slope, causes form drag, or stress normal to the surface), they concluded that this sheltering effect may control the transfer of momentum from the wind to the waves.

Here, in figure 3.1 panels k and l, we present along-wave surface viscous stress measurements, taken within the airflow's viscous sublayer (averaged from 100 and to 500 μm above the air-water interface). It can be noted that viscous stress is also commonly referred to as skin friction drag, in aerodynamics, (e.g., Schlichting and Gersten, 2000). The viscous stress is computed from:

$$\tau_\nu = \mu \left(\frac{\partial U}{\partial \zeta} + \frac{\partial W}{\partial \xi} \right)_{\zeta \sim 0} \tag{3.1}$$

where μ is the air dynamic viscosity, and U and W are respectively the projections of the air velocity vector along directions that are locally tangent and normal to the instantaneous water surface, within the along-channel plane. It can be noted here that the second term of equation 3.1, very small, has been omitted in previous viscous stress estimates (e.g., Reul et al., 1999; Grare et al., 2013b).

Over the steeper, airflow separating wave, the viscous stress peaks at the crest, where it matches the total stress ρu_*^2 (figure 3.1k). It dramatically drops just past the crest, at the point of separation of the airflow. The surface viscous stress then becomes negative (below the flow reversal region), and remains close to zero up to $\phi \sim 3\pi/4$, and then slowly increases back up to $\sim 50\%$ of the total stress, on the windward side of the next wave. Over the non-separating wave, the viscous stress is greatest just before and at the crest, and decreases past the crest, to $\sim 15\%$ of the total stress (figure 3.1l). It then increases just before $\phi = \pi$, decreases just past the trough, and slowly increases again upon approaching the next wave. While the general behavior upwind of both wave crests (airflow separating and non-separating) is an increase in surface viscous stress, downwind of crests the picture depends greatly upon the occurrence of airflow separation. In particular, the downwind face of the airflow separating wave is exerting at times upward viscous stress on the airflow, while the non-separating wave only experiences a reduction of downward stress on its lee side.

In fact, the turbulent Reynolds stresses, plotted in figure 3.1 panels m and n, also show large differences between the separated and non-separated cases. Structures

of extremely intense turbulent stress (almost $O(100\rho u_*^2)$) dominate the lee of the airflow separating wave (figure 3.1m). These are located in the region where the free shear layer, source of intense mixing and turbulence production, breaks up into turbulent vortices. In contrast, the smoother wave only shows a minor increase of turbulent stress in the viscinity of the surface past the crest (figure 3.1n). In this non-separated sheltering case, the turbulent structures are located where the ejection of low velocity fluid occurs, which is in general agreement with previous results from turbulent boundary theory, i.e. that such ejections are important sources of turbulence for the boundary layer as a whole (Robinson, 1991).

3.2.2 Note on the lifetime of the near surface turbulent events

The question of the duration of the observed turbulent events is addressed next. Estimating the lifetime of coherent turbulent structures has been the subject of vigorous debate in turbulent boundary layer studies over solid flat surfaces (e.g., Kline et al., 1967; Robinson, 1991; Jiménez, 2011). The lifetime of airflow separation events, which has been an important question in turbulent boundary layer separation studies (Simpson, 1989), is also discussed below.

Recent results in turbulent boundary layer studies have shown the existence of coherent, relatively long-lived (with respect to turbulence timescales) structures in the buffer and logarithmic layers of wall-bounded turbulent flows (Robinson, 1991; Adrian, 2007; Jiménez, 2011). These results have important consequences for the spatial distribution of turbulent production mechanisms within turbulent boundary layers (Jiménez, 2011). For the wind-wave coupling problem, spatial (and particularly along-wave) distribution of turbulence production is crucial, because it may influence how wind stress is transferred to the wave field below. We suggest here that the presence of long-lived spatially coherent structures near the water surface may have an influence on the distribution of turbulent stress along the water surface, which could be important for the initial stages of wave generation. When surface waves are present,

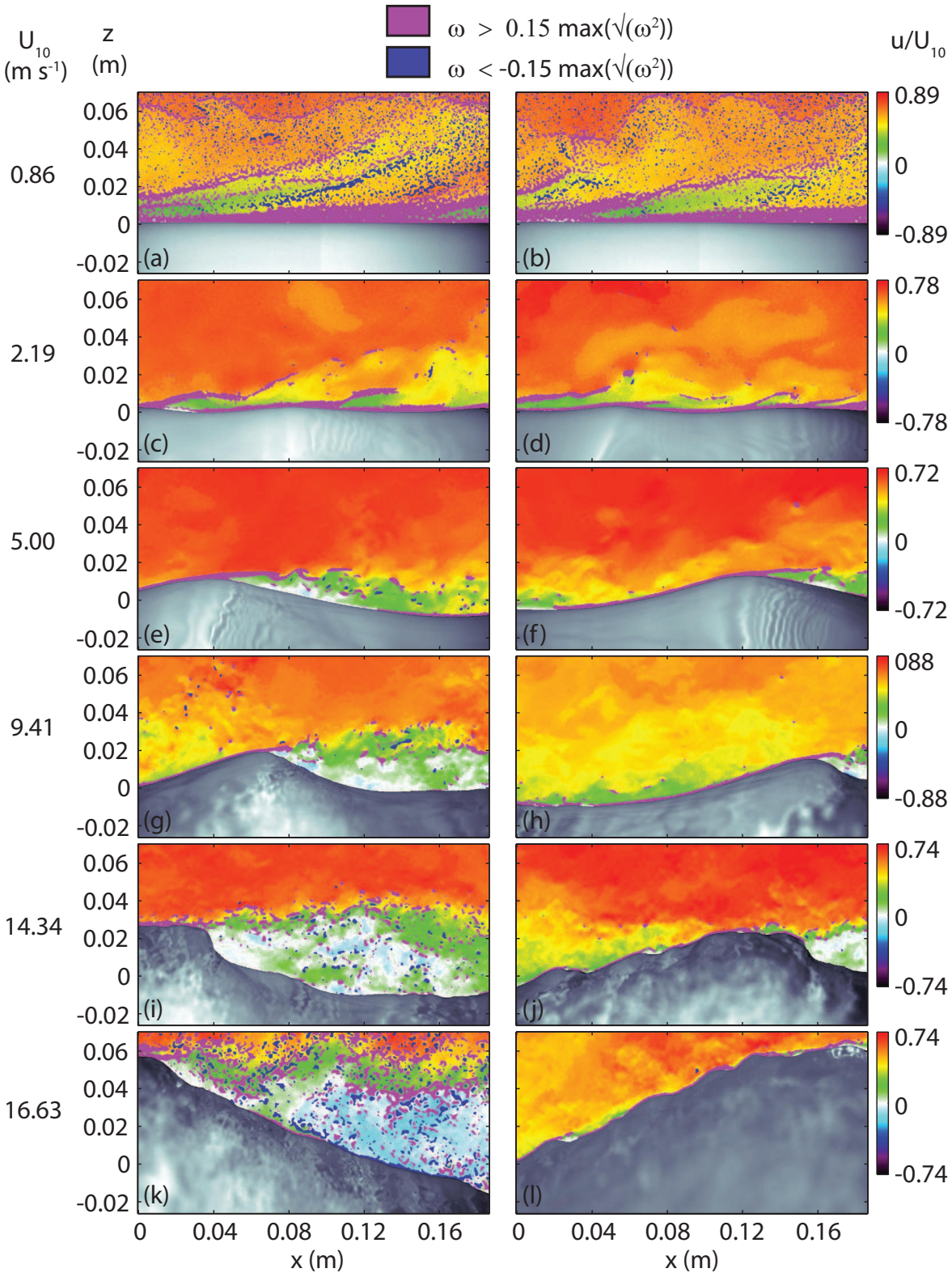

Figure 3.2: Left: $t1$, right: $t1 + 1/7.2$ s. Regions of important positive and negative spanwise vorticity ($|\omega| > 0.15\max\left(\sqrt{\omega^2}\right)$), superimposed over normalized horizontal velocity field u/U_{10}.

the phase-locked distribution of the turbulent structures may also contribute to wave growth.

A common difficulty with experimental studies has been that the identification of "bursting" events by a fixed probe may be biased by the measurement technique, since a long-lived event rapidly passing by the probe may be mistaken for a short-lived burst (Robinson, 1991). The 7.2 Hz sampling frequency of our two-dimensional PIV imaging system allowed us to observe the evolution over two time steps, of turbulent velocity and (spanwise) vorticity structures in the airflow above the air-water interface.

In figure 3.2, thresholded ($|\omega| > 0.15\text{max}\left(\sqrt{\omega^2}\right)$) and binarized (purple for clockwise, blue for anti-clockwise) instantaneous spanwise vorticity fields are superimposed over velocity fields, taken from two consecutive PIV measurements. Examples are shown where one can recognize similar structures in the air from one image to the next. In the first experiment ($U_{10} = 0.86$ m s^{-1}), where no waves are visible, low velocity fluid is ejected away from the surface before $x = 0$ (not visible here) and up to $x =$ 4 cm (figure 3.2, panel a). Then, 139 ms later (1/7.2 s), the same downwind tilted low velocity region is clearly visible between $x = 4$ cm and $x = 10$ cm (figure 3.2b). Once ejected upward, the low streamwise velocity region is surrounded by higher velocity fluid. The boundaries between low velocity and high velocity regions are clearly visible in the instantaneous velocity fields and their existence implies the presence of free layers of high shear between the different velocity contours. In fact, in figure 3.2a, we observe directly the positive (spanwise) vorticity layer marking the upwind boundary of the low velocity ejection, and the negative vorticity layer along the downwind boundary. Thus the ejected, downwind tilted, low velocity region is "sandwiched" between two regions of higher velocity fluid. Similar features are still present 139 ms later, approximately 4 cm farther downwind (figure 3.2b). This suggests that such low velocity fluid ejections, although they are being rapidly advected downwind, remain coherent for some time before being fully dissipated.

When surface waves are present (or at least detected), which requires slightly higher wind speeds, single turbulent feature tracking is more difficult in the airflow,

especially away from the surface, because the velocities are too high for structures to be detected from one image to the next (and perhaps such structures are short-lived). However, near the surface, the airflow is coupled with the waves in such a way that specific events appear to be phase-locked. In particular, over small wind waves in low winds (U_{10} = 2.19 m s^{-1}) (panels c and d in figure 3.2), low velocity ejections occur predominantly on the downwind face of waves. This can be explained by the fact that downwind wave faces are areas of adverse pressure gradients. Adverse pressure gradient conditions have been found in the past to be favorable to ejections and sweeps, in studies over solid flat plates (Kline et al., 1967; Kovasznay, 1970). Over waves, the problem is further complicated by the movements of the air-water interface, and in particular the wind driven surface drift, the surface orbital motions, and the continuously evolving shapes of the wave profiles as single waves travel and propagate through a group. Here (in figure 3.2, panels c and d), we can recognize a detached high vorticity layer stemming from a region of the surface just past a wave crest located at $x = 0$ in panel c, and extending for some distance downwind, away from the surface (up to x = 8 cm). Later (figure 3.2d), the same wave has traveled downwind by approximately 5 cm, and the same vorticity layer is still stemming from its crest, but now is broken some distance downwind of the crest (near x = 8 cm).

At higher wind speeds (panels e through l in figure 3.2), airflow separation occurs past the crests of the waves sampled here. In the two lower wind speed airflow separating cases (U_{10} = 5.00, 9.41 m s^{-1}, figure 3.2 panels e through h), the viscous sublayer, characterized by a thin, elongated region of high surface (spanwise) vorticity, is well established and remains intact upwind of the wave crest, and then clearly detaches from the surface past the crest. There is no longer a surface viscous sublayer past the crest of these airflow separating waves, until the flow gradually reattaches some distance downwind. In fact in the lower wind case (U_{10} = 5.00 m s^{-1}), the viscous sublayer is already being regenerated before the next trough (panel e, figure 3.2).

In the two highest wind speed cases (U_{10} = 14.34, 16.63 m s^{-1}), the separation of the airflow creates intense free shear past the wave crest, but we do not observe a

coherent detached high spanwise vorticity layer. Furthermore, at the surface, before and at the crest, the high vorticity structures also appear to break up and lose coherence. We can even observe small airflow separation events past the crest of one of the small scale waves that populate the surface of the peak wave plotted here (for example near $x = 7$ cm in figure 3.2j). The lack of a coherent viscous sublayer suggests that the airflow is aerodynamically rough everywhere. More details on the aerodynamic roughness of the mean flow are provided below.

Thus, two main mechanisms are observed on these instantaneous velocity and vorticity fields above wind waves. First, at low wind speeds ($U_{10} = 2.19$ m s^{-1}), low velocity fluid is ejected upward and high velocity fluid is swept downward. This is probably caused by coherent quasi-streamwise vorticity structures in the airflow near the water surface. These ejections and sweeps cause elongated high vorticity regions to form between the regions of constant momentum, such as those observed over solid flat plates by Meinhart and Adrian (1995), for example. The observed phase-locking of ejections and sweeps (on the few instantaneous snapshots shown thus far), is coherent with a phase-locking of quasi-streamwise vortical structures, as was observed over solid wavy surfaces by Calhoun and Street (2001). This was also predicted by the DNS results of Yang and Shen (2010). Second, at slightly higher wind speeds ($U_{10} = 5.00$, 9.41 m s^{-1}), airflow separation past a wave crest leads to the detachment from the surface of a relatively stable coherent high shear layer, which becomes unstable and disintegrates into vortical eddies, some distance downwind. The instabilities observed past airflow separating wave crests, are in agreement with past studies of perturbed free shear layers (Ho and Huerre, 1984). The distance over which detached high vorticity layers remain coherent, decreases with increasing wind speed; such coherent structures vanish at high wind speeds ($U_{10} = 14.34$, 16.63 m s^{-1}). In addition, our observations on the existence of a viscous sublayer are in broad agreement with Melville (1977), who, using order of magnitude estimates, predicted that smooth wall conditions are required for a distance on the order of 1 m, for a smooth-flow type viscous sublayer to fully form. Our measurements do however suggest that even in airflow separation

conditions, coherent viscous sublayers appear to have enough time and distance to fully exist, on the windward face of wind waves, but only when the upwind face of these waves is smooth enough (see also mean phase averaged viscous stress results, later in this chapter).

Finally, we note that all three of the airflow separating waves shown in figure 3.2, are displaying flow separation at two different moments in time. This suggests that, much like ejections over the flat water surface in low winds, airflow separation events at high winds may be "intermittent" rather than "incipient" [1], at least over the lifespan of an individual wave. However the lifetime of the wave profile is a key (and complicating) factor in our case, because a wave changes shapes as it evolves through space and time, especially at high wind speeds, where waves become strongly nonlinear and often break (see for example the evolution of the wave profile in figure 3.2, panels i and j). Nonetheless, in spite of a large change in the wave profile (that occurs over 1/7.2 s), the airflow above the wave in figure 3.2i is still separated in panel j. It is apparent that once separated past the crest of a steep wave, the airflow tends to remain separated past that wave, even as the wave breaks and perhaps becomes less steep (not clearly shown here, because we cannot follow a wave for times longer than 1/7.2 s). Similarly, in aerodynamics, turbulent boundary layer separation has been found to be subject to a hysteresis effect (commonly called "stall hysteresis"), whereby reattachment of the airflow can only occur in more favorable pressure gradient conditions than are required for the already attached flow to remain attached (e.g., McCroskey, 1982). In any case, the persistence (in time) of airflow separation past a wave crest, may have important consequences for the coupling between wind and waves, and in particular, for the momentum transfer mechanisms between wind and waves: for example, along-surface tangential stress shows dramatic along-wave variations when airflow separation occurs (figure 3.1k). If this surface stress drop takes place throughout the lifetime of the wave

[1] In the sense specific to the turbulent boundary layer separation (over solid boundaries) community, who, based on the percentage of time that the flow is detached, distinguish "incipient" from "intermittent transitory", "transitory" and finally simple "detachment". This was well summarized by Simpson (1989).

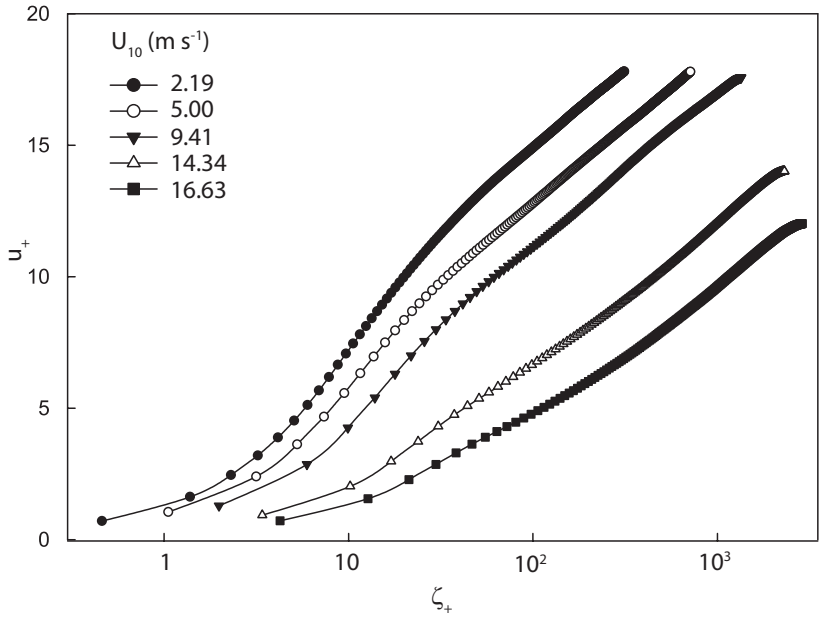

Figure 3.3: Profiles of mean along-channel velocity, in surface-following coordinates. The plotted quantities are wall normalized: $u_+ = \overline{u}/u_*$, $\zeta_+ = \zeta u_*/\nu$, with ν the kinematic viscosity of air).

as it propagates downwind, this will certainly influence the growth and dissipation of the wave field.

3.3 Mean Profiles

The instantaneous snapshots presented thus far suggest that the instantaneous dynamics in the airflow above wind waves are not only a function of wind speed (e.g., occurrence or not of airflow separation, existence and lifetime of coherent turbulent structures in the airflow), but also of the position along the wave profile, or wave phase (e.g., along-wave surface viscous stress distribution). In order to determine the importance of these events on the air-water momentum flux as a whole, we present in this section an investigation of the mean flow properties.

3.3.1 Velocities

In figure 3.3, we show the mean airflow velocity profiles for each wind wave experiment, in the surface following coordinate system. Over 3 x 10^6 profiles were used

to compute each of these mean profiles. Away from the surface, the profiles follow a log-law, which suggests that turbulent stress dominates the airflow (Schlichting and Gersten, 2000). Very close to the surface, the mean profiles deviate from the log-law. They are linear very close to the surface at low wind speeds. This means that on average, viscous effects are important near the surface. With increasing wind speed, the profiles increasingly deviate from the law of the wall over a flat plate, since for example the logarithmic part extends beyond $z_+ = 10^3$, for $U_{10} = 9.41$ m s^{-1} (in contrast with past results over flat plates, see for example Schlichting and Gersten (2000)). We attribute this shift to the non-zero wave phase velocities (C_p) and the surface wind drift. The log-law over a rough surface can be written as (e.g., Schlichting and Gersten, 2000):

$$\frac{\overline{u}}{u_*} = \frac{1}{\kappa} \ln \frac{z}{z_0}$$

where κ is the von Karman constant, z_0 the roughness height, u_* the airflow friction velocity. It should be mentioned here that existing literature is unclear on the choice of a frame of reference, when comparing airflow velocity measurements above waves, to the law of the wall. For example, Hsu et al. (1981) found a very different roughness parameter (z_0) than Stewart (1970) for similar experimental conditions. Hsu et al. (1981) attributed the difference to the fact that their frame of reference was vertically oscillating, in order to follow the surface, whereas Stewart's was cartesian. Hsu et al. (1981) claimed that the choice of frame of reference affects the slope of the logarithmic profile. This in turn impacts the roughness parameter, determined by the intercept of the mean log profile with $u_+ = 0$. In contrast, we find that the slopes of the logarithmic profiles (and hence the estimates of u_*), are independent of the vertical oscillations of the frame of reference, because the wave-induced mean flow variations disappear away from the surface. In fact, we obtain similar results (not shown here) for u_* and z_0, whether we use our surface following frame of reference or a fixed cartesian frame of reference.

We suggest however that a large variability in the estimates of the roughness

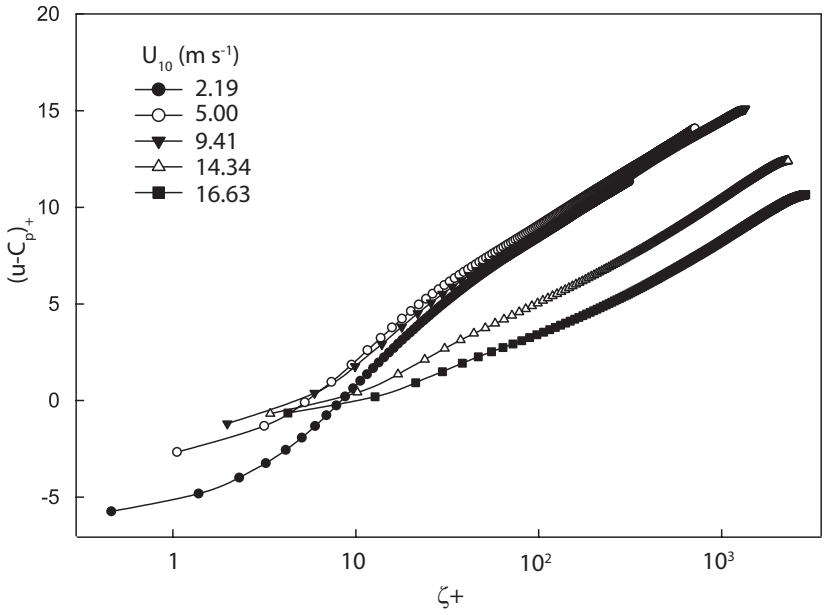

Figure 3.4: Profiles of mean along-channel velocity, in surface-following coordinates, and moving at wave phase velocity C_p. Wall normalized quantities are defined as: $(u - C_p)_+ = (\overline{u})/u_*$, $\zeta_+ = \zeta u_*/\nu$, with ν the kinematic viscosity of air).

length may come from the horizontal motions of the water surface. The roughness length problem is actually at the heart of the airflow separation debate, since, for example, if the airflow is separated from the water surface most of the time and over most of the space, then the wavy surface may be seen as a solid (moving) rough wall. In fact, the concept of roughness over a wall depends entirely on the scale of the roughness elements (Belcher and Hunt, 1998). If the roughness elements are large and smooth enough such that the airflow remains attached most of the time, then the intercept of the log profile with the z-axis has a different meaning than if the flow is detached most of the time, i.e., it does not "follow" the surface.

In figure 3.4, we removed the peak wave velocity from the mean profiles. The logarithmic parts of the three lowest wind speed cases collapse, and follow remarkably well the law of the wall. However the two higher wind speed cases remain different. We attribute this discrepancy in part to the wind drift, which is not considered here. But wind drift alone cannot account for the difference: a shift of at least $3C_p$ would be

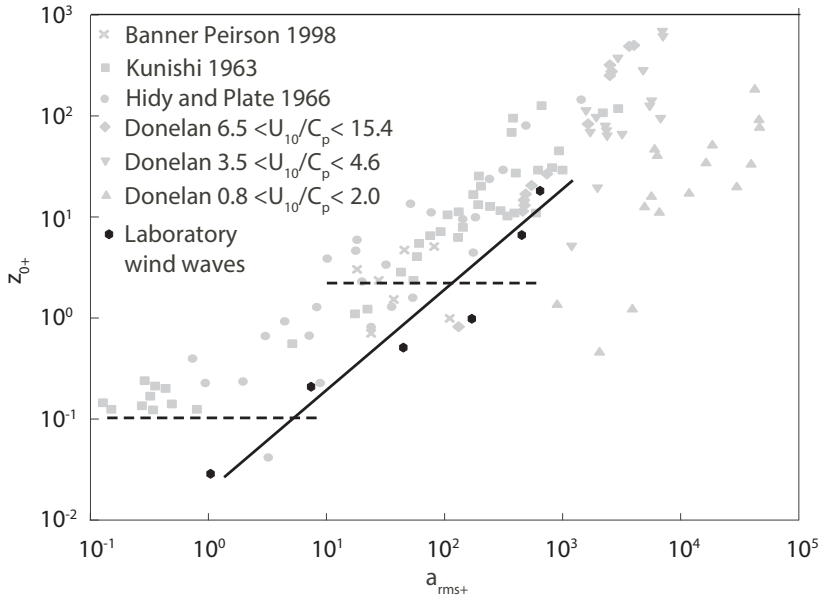

Figure 3.5: Mean wall-normalized roughness parameter $z_{0+} = u_* z_0/\nu$ as a function of wall-normalized root-mean-square wave amplitude $a_{rms+} = u_* a_{rms}/\nu$. The horizontal lines are limits between smooth, transitional, and rough flows, as defined by Kitaigorodskii and Donelan (1984). The solid line is a best log-linear fit of our data (slope: 0.89, $R^2 = 0.93$).

needed in order to collapse these two highest wind speeds with the lowest three. This change in regime is also produced by the onset of intermediate airflow separation (see statistics below), that strongly affects the mean airflow properties.

3.3.2 Aerodynamic roughness

As stated above, the estimates of aerodynamic roughness strongly depend on the horizontal velocity of the frame of reference used to measure the along-wind velocities. For example, Sullivan et al. (2000), using their DNS results, computed z_0 in a frame of reference moving at the phase speed C_p of their monochromatic sinusoidal waves. Past field and laboratory studies have used fixed frames of reference to compute z_0 (e.g., Donelan, 1990). For comparison with such results, we show in figure 3.5 our values of normalized roughness z_{0+} estimated in a fixed frame of reference, as a function of the wall-normalized root-mean-square amplitude of the waves a_{rms+}. Past laboratory and

field results (extracted from Donelan (1990)) are also plotted. If we use the classification devised by Kitaigorodskii and Donelan (1984) (see also the similar classification from Donelan (1990)), our lowest wind speed experiment (U_{10} = 0.86 m s^{-1}) falls within the smooth flow category. Then, in our three lowest wind speed experiments (U_{10} = 2.19, 5.00, and 9.41 m s^{-1}), the airflow is transitionally rough. The airflow in the two highest wind speed cases (U_{10} = 14.34, 16.63 m s^{-1}) is fully rough. Our values are coherent with past laboratory and field measurements reported in Donelan (1990), and reproduced in figure 3.5. It can also be noted that in a frame of reference moving with the waves, our roughness length estimates would have been rather increased, by up to 200%, but the increased values still fall in the same respective categories between smooth, transitional, and rough (not shown here). Additionally, in figure 3.5, the correlation of z_{0+} with a_{rms+}, is generally good at low wind speeds. The roughness estimates present more scatter at higher wind speeds. The departures from the law of the wall that we begin to observe for our two higher wind speed (and higher wave amplitude) cases, are coherent with this scatter.

So far, we have shown that the mean flow becomes on average more rough with increasing wind speed. In general, "dynamically smooth surfaces are defined to be such that the average height of roughness elements at the surface is smaller than the thickness of the viscous sublayer" (Kundu and Cohen, 2010), whereas aerodynamically rough surfaces have "roughness elements [that] protrude outside the viscous sublayer" (Kundu and Cohen, 2010). From instantaneous surface viscous stress and vorticity fields, we have observed that the viscous sublayer tends to exist everywhere along the wave profiles at low wind speeds. At slightly higher wind speeds, when airflow separation occurs past smooth wave crests, the viscous sublayer remains intact on the upwind face of waves, and disappears on the downwind side. Finally at high wind speeds, the viscous sublayer is broken up by roughness elements. Phase-averaging the measured quantities is necessary in order to understand the influence of these along-wave variations in roughness, on the mean along-wave momentum flux.

3.4 Mean Along-Wave Airflow Characteristics: Phase Averages

3.4.1 Velocities

Phase averaged velocities are plotted in figure 3.6, for each wind wave experiment. The mean horizontal velocity fields $\langle u \rangle / U_{10}$ show that the airflow is fast on the upwind face of the waves, and slows down on the downwind face. This is a sheltering effect past the crest of the waves, as predicted by Belcher and Hunt (1998). This effect corresponds to a thinning of the boundary layer as the airflow approaches the crest, and a boundary layer thickening past the crest. This can be readily observed on the mean $\langle u \rangle / U_{10}$ profiles that are plotted in figure 3.6, at phases $\phi = -\pi/2, 0, \pi/2,$ and π. No flow reversal is observed in the horizontally fixed frame of reference. In a frame of reference moving at peak wave phase speed C_p, the horizontal component of the airflow would be reversed near the surface, downwind of crests (not shown here, but see for example figure 4.5 later in chapter 4). This effect, when combined with downward vertical velocities past the crest, is commonly referred to as a cat's eye pattern (e.g., Miles, 1957), because in that particular frame of reference, the mean streamlines in the airflow downwind of crests are closed and present sharp upwind and downwind kinks. Streamlines are however dependent upon the frame of reference. In contrast, the sign and intensity of the spanwise vorticity at the surface are more reliable indicators of airflow separation, because vorticity is a Galilean invariant property of the flow (e.g., Wu et al., 2006). In fact, on average, the vorticity at the surface is very similar to the slope of the vertical profile of horizontal velocities at the surface, because average horizontal variations of vertical velocities are small compared with the vertical variations of horizontal velocities (slope of the mean profile). While the slope of the profiles vary as the boundary layer thins and thickens, the slope never becomes negative. Although airflow separation clearly occurs past a portion of the waves, it does not cause the mean horizontal velocity component to be reversed.

At the four highest wind speeds (figure 3.6, panels g through j), the phase averaged vertical velocities $\langle w \rangle / U_{10}$ show common phase locked features: the air moves upward above positive wave slopes, and downward above negative slopes. This behavior

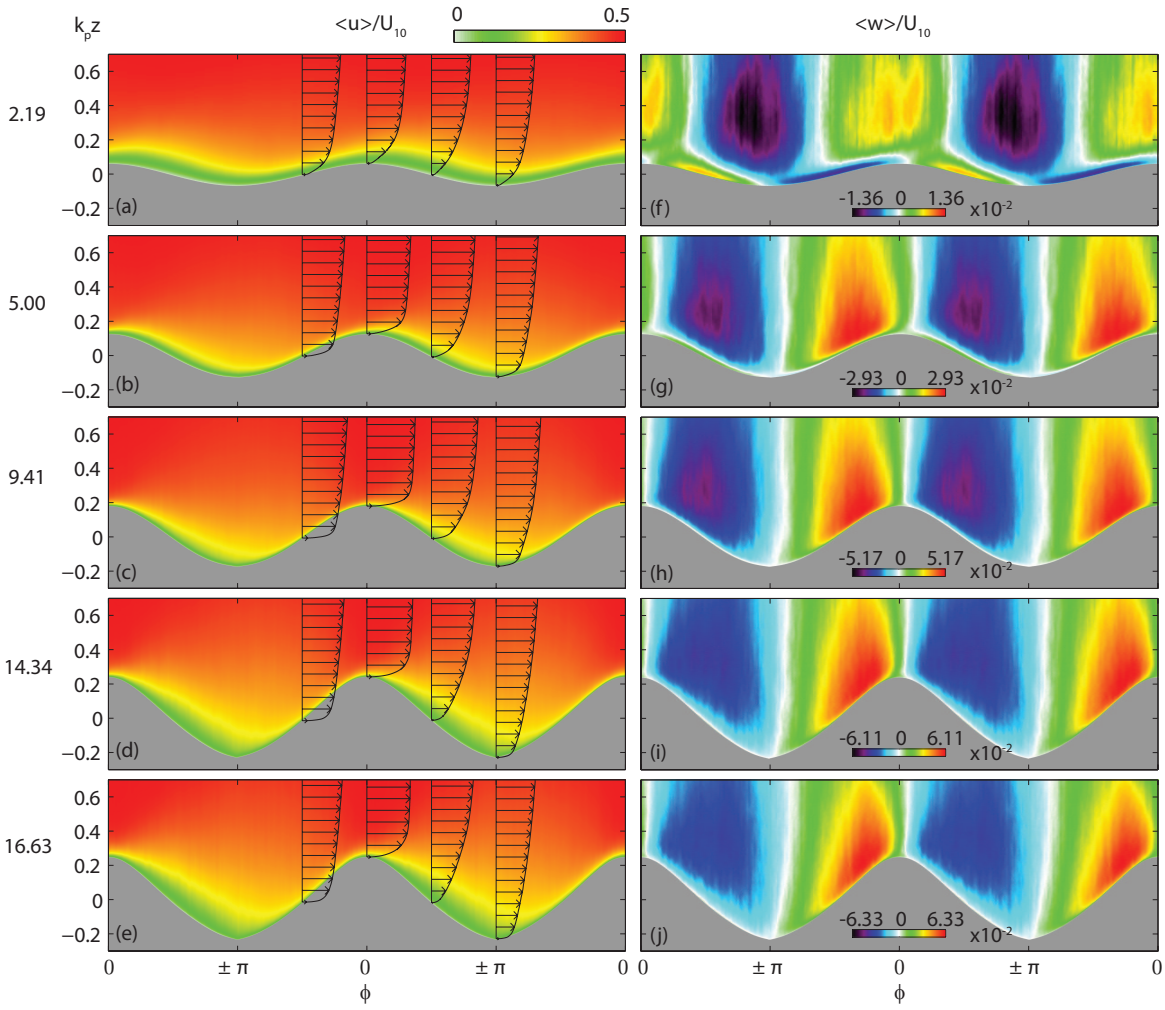

Figure 3.6: Normalized phase averaged velocities, plotted over the mean water surface elevation. On the left, we show the horizontal velocity component ($\langle u \rangle / U_{10}$), along with mean horizontal velocity profiles above the upwind face, the crest, the downwind face, and the trough of the waves. The vertical profiles hint to the variations in boundary layer thickness (see also figure 3.7 later), while the color plots emphasize the sheltering effect. On the right are plotted the phase averaged normalized vertical velocities $\langle w \rangle / U_{10}$.

is similar to that of a non-separating, surface-following airflow above solid hills (e.g., Belcher and Hunt, 1998). However, in the case of the two highest wind speeds (panels i and j in figure 3.6), an asymmetry is apparent, between the intensity of the upward velocities and the downward velocities. The latter are on average weaker than the former. This effect is exacerbated close to the surface: on the upwind face of the waves, $\langle w \rangle / U_{10}$ is strong and positive (upward), while on the downwind face, $\langle w \rangle / U_{10}$ is very weakly negative (downward). This asymmetry is caused by the large sheltering that occurs past these steep waves: the airflow is dramatically constrained upward by the wave crest, and then tends to not follow the surface as well, past the crest. Interestingly, on the downwind face of the waves, $\langle w \rangle / U_{10}$ is not positive on average, in spite of numerous airflow separation events at such high speeds (see airflow separation statistics later in section 3.5). This points to the very turbulent nature of airflow separation events above wind waves. Instantaneous (turbulent) upward velocities are found past airflow-separating waves, but their turbulent fluctuations in space are such that they don't always take place at the same wave phase. Hence the mean airflow moves downward past wave crests.

In figure 3.6f, the behavior of $\langle w \rangle / U_{10}$ is different. Within a thin layer near the surface, the behavior of $\langle w \rangle / U_{10}$ is the exact opposite of what we have observed in figure 3.6, panels g through j: here, within the critical layer, the airflow is forced downward upwind of crests, and upward downwind of crests. These motions are coherent with a forcing from the underwater and surface wave orbital motions. This near surface effect (below the critical height) and its relation to wave age is discussed in more detail in chapter 4. Outside the critical layer, $\langle w \rangle / U_{10}$ is more similar to the higher wind speed cases, but with a phase shift of $\pi/4$: The regions of downward motion are nearly centered on the wave troughs, and the regions of upward motion are almost centered on crests. This behavior is reminiscent of Miles' critical layer wave growth mechanism. Solutions of the inviscid laminar shear layer instability problem show a similar behavior in the mean vertical velocities (e.g., Hristov et al., 2003). Practically, the outer flow is disconnected from the water surface, because it does not immediately

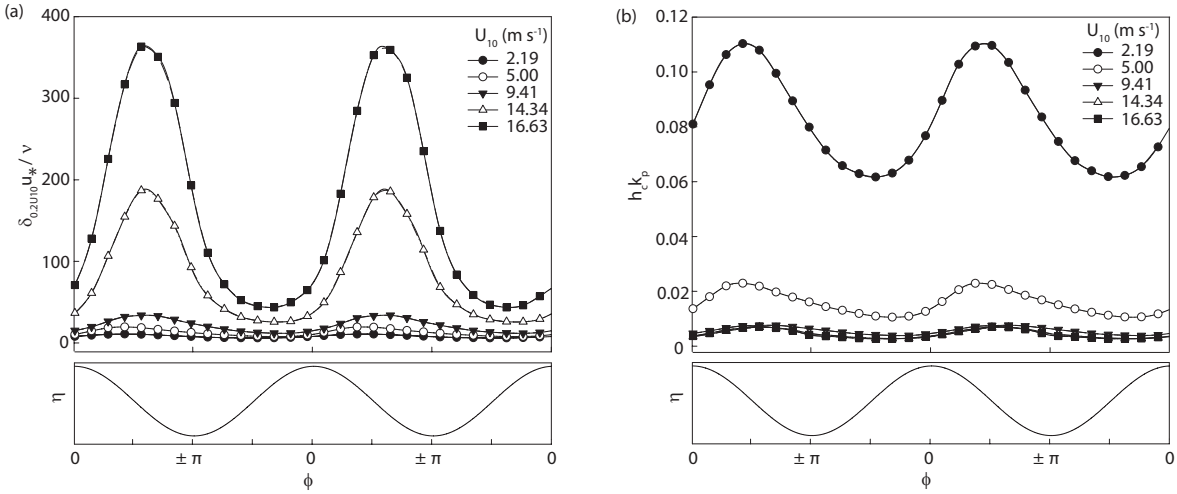

Figure 3.7: (a) Mean along-wave wall-normalized boundary layer thickness, defined here as the height δ where $\langle u \rangle = 0.2U_{10}$. (b) Mean along-wave critical layer thickness (normalized by peak wavenumber k_p). A sketch of a mean wave profile is provided (bottom panels) to help visualize the wave phase.

react to the adverse and favorable pressure gradient conditions offered by the wavy surface. However, as was mentioned above, the mean horizontal velocity field (figure 3.6a) shows a mean behavior of boundary layer thickening and thinning.

In order to quantify the thickness of a boundary layer, one can measure the height at which $\overline{u} = 0.99U$, where U is the free stream velocity (Schlichting and Gersten, 2000). While this approach is arbitrary in terms of the absolute value of the boundary layer height, we use a similar method here in order to compare relative variations in the boundary layer thickness. We arbitrarily chose to look at the distance above the water surface where the mean velocity is $0.2U_{10}$ (see figure 3.7a). The broad features of the mean, wall-normalized boundary layer thickness (noted δ_+ hereafter), are an increase past crests and a decrease before crests, at all wind speeds. The amplitude of these phase-locked variations in boundary layer thickness is much greater (up to over ∼10 fold) for the two highest wind speed experiments ($U_{10} = 14.34$, 16.63 m s^{-1}), compared with the three lower wind speed cases ($U_{10} = 2.19$, 5.00, 9.41 m s^{-1}). While

the boundary layer thickness remains quite low in all cases ($\delta_+ < 60$) as the airflow approaches the crest, it is the average thickening that is drastically more extreme at high wind speeds than at low to moderate wind speeds. This may be explained by the increased occurrence of airflow separation events past wave crests at higher wind speeds (see airflow separation statistics below), which tend to dramatically reduce the velocity past wave crests. This dramatic drop was shown in figure 3.1a for example. Finally, the variations in δ_+ show on average a phase lag of approximately $\pi/2$ with respect to the wavy surface. This result holds for all wind speeds, and is coherent with studies over solid wavy boundaries (e.g., Belcher et al., 1993). In addition, the phase lag of the peak boundary layer thickness increases slightly with increasing wind speed. This may be related to the phase lag variations of surface viscous stress. These are discussed later in this chapter.

Another reference height, relevant for wave generation and growth, is the height above the waves where the airflow velocity matches the phase speed of the waves, the "critical height" h_c (Miles, 1957). This variable, has also been called "matched height" by Phillips (1977) and later Belcher and Hunt (1998), who questioned its critical role for wave growth in turbulent airflow conditions, especially when wind waves are what they consider to be young or "slow" ($C_p/u_* < 15$) (Belcher and Hunt, 1998). The critical height, plotted for all wind wave experiments in panel b of figure 3.7, shows similar along-wave variations as the boundary layer thickness does. The critical height shows a phase lag of approximately $\pi/2$ with respect to the mean water surface, at all wind speeds. Additionally, it should be noted that the thickness of the critical layer increases here with decreasing wave speed. The reason for this is presumed to be the fact that the age of our wind waves increases with decreasing wind speed. The critical layer height increases with increasing wave age (see chapter 4 later).

Next, we investigate four aspects that are closely related to the thinning/thickening of the boundary layer before/past wave crests: (1) the along-wave distributions of wave-coherent and turbulent stresses within the airflow above waves, (2) the partitioning of the turbulent momentum fluxes between four quadrants (see quadrant analysis below),

(3) the along-wave distribution of turbulent kinetic energy production, and (4) the along-wave distribution of surface viscous stress.

3.4.2 Turbulent and wave stresses

The phase-averaged normalized turbulent (or "Reynolds") stresses $-\langle u'w' \rangle / u_*^2$ are plotted in figure 3.8 (left), for each wind wave experiment. On the right, we show the average Reynolds stress across all phases $-\overline{u'w'}/u_*^2$. At all wind speeds, $-\langle u'w' \rangle / u_*^2$ displays a strong coupling with the waves. Regions of strong Reynolds stress are found on average downwind of the waves, which is where the boundary layer thickens. This phase-locked "jet" of increased turbulent stress can be related to the sheltering effect (separated or not) that occurs downwind of waves. The separation of the airflow past wave crests is the obvious candidate to explain increased turbulence production past crests, since detached free shear layers are primary producers of turbulence. However, the non-separated sheltering can also increase turbulence because it is also associated with free shear layers. As mentioned above, these mark the interfaces between swept/ejected regions of high/low velocity, which are known to occur often in such adverse pressure gradient conditions (e.g., Kline et al., 1967; Kovasznay, 1970). It should also be noted that in figure 3.8, the lowest wind speed case ($U_{10} = 2.19$ m s^{-1}) differs from the four others, in that the regions of high Reynolds stresses (downwind of crests) are only marginally more intense that the surrounding stresses at other phases. It is likely that these smaller amplitude waves do not cause as much turbulence-generating sheltering as the others. In addition, we had observed in figure 3.2 that detached free shear layers in these lower wind speed conditions simply do not break up as fast and as much into small-scale vortical eddies, as in high wind speed conditions. So these longer-lived free shear layers extend farther past just the downwind face of waves (than at higher wind speeds), and generate less intense turbulence. In that sense, they are "smearing" the turbulent stresses which are now more uniformly distributed along the average wave. Finally, over the older waves of this lower wind speed experiment ($U_{10} = 2.19$ m s^{-1}, $C_p/u_* = 6.5$), we notice a near-surface layer of reduced turbulent stress at

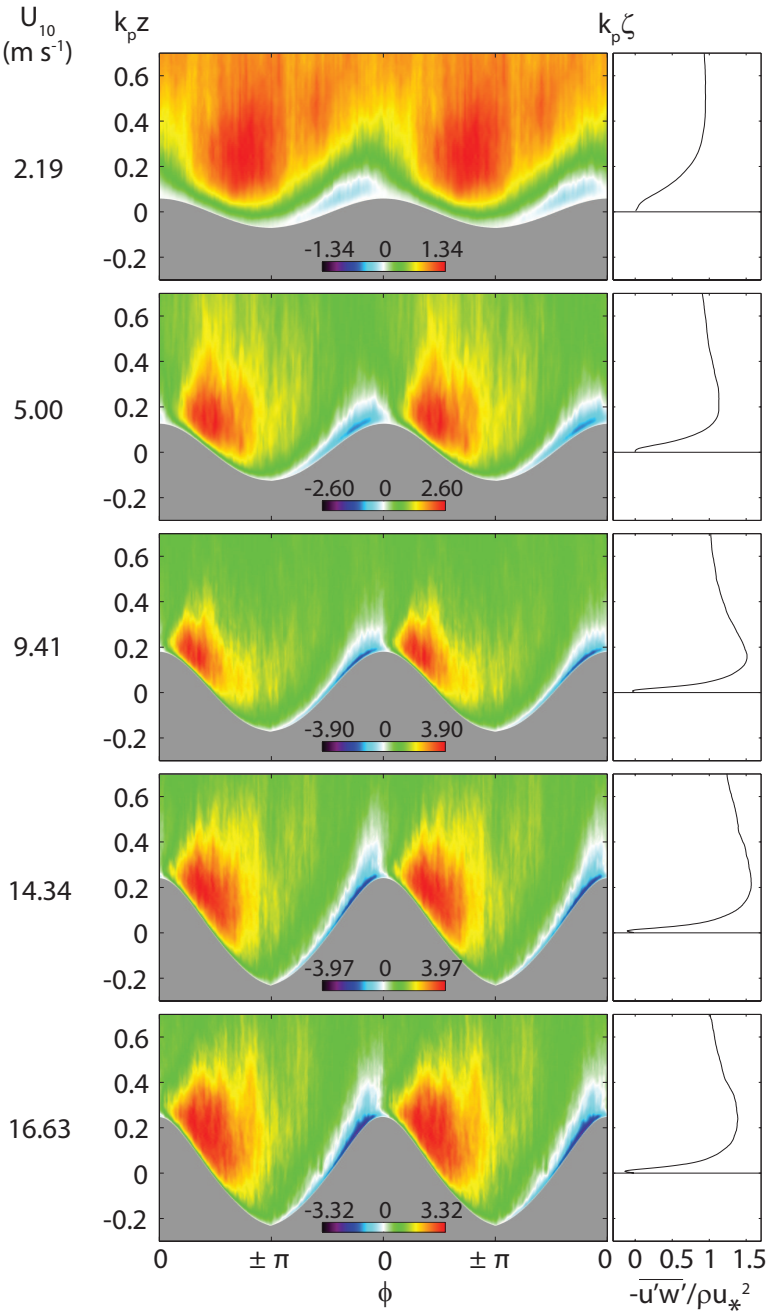

Figure 3.8: Normalized phase averaged turbulent stress $-\langle u'w' \rangle / u_*^2$ (left) and total mean (across all phases) turbulent stress $-\overline{u'w'}/u_*^2$ (right). Phase averages are plotted above the phase averaged water surface elevation, and total mean profiles are plotted with respect to the surface following vertical coordinate ζ. Each line corresponds to one experiment, and the corresponding mean 10-m wind speeds are indicated on the left.

all phases. This suggests that within the critical layer, the work of turbulent forces on the waves is reduced, and airflow is coupled with the underwater wave orbital motions.

In all five experiments, the Reynolds stress near the surface is negative (upward flux) along the upwind face of the waves, and positive (downward flux) along the downwind face. The cause for the negative stress region on the windward face of wavy surfaces, has recently been debated by Yang and Shen (2010). They compare their DNS results over Airy water waves, to experimental results from Hudson et al. (1996), who were able to measure turbulent velocities in water flowing over a solid wavy wall. Hudson et al. (1996) computed Reynolds stresses in a cartesian coordinate system, and also found thin regions of negative stress, upstream of their solid waves. They interpreted this to be an artifact of the coordinate system, and noted that the stresses in an along-surface projected coordinate system ($-\langle U'W' \rangle$) remain positive everywhere. In contrast, Yang and Shen (2010), who observed in their DNS results relatively large regions of negative stress on the upwind face of relatively old ($C_p/u_* = 25$) Airy waves, suggested that these regions were related to the along-surface horizontal gradient of wave-orbital induced vertical motions in the air. They further stated that, in spite of the negative sign of the mean Reynolds stress in that region, sweeps and ejections are in fact produced in those regions (this is counter-intuitive because in turbulent boundary layers, sweeps (Q2 events) and ejections (Q4) are generally attributed to positive turbulent flux events; see for example the definition of Q2 and Q4 events in section 3.2 above). We do confirm that older waves induce on average important vertical motions in the air (downward motions upwind of crests, and upward motions downwind of crests), as can be seen when looking again carefully at the near surface phase averaged vertical velocities in panel f of figure 3.6. This is even more obvious in our results over older, mechanically generated waves, presented in the chapter 4, where we have also estimated the underwater and surface orbital velocities. However, our results over young wind waves are in disagreement with Yang and Shen (2010), since in the case of our young wind waves, we find that the wave-orbital-induced velocities in the air are negligible compared with the "sheltering effect" (Belcher et al., 1993) of the waves, on

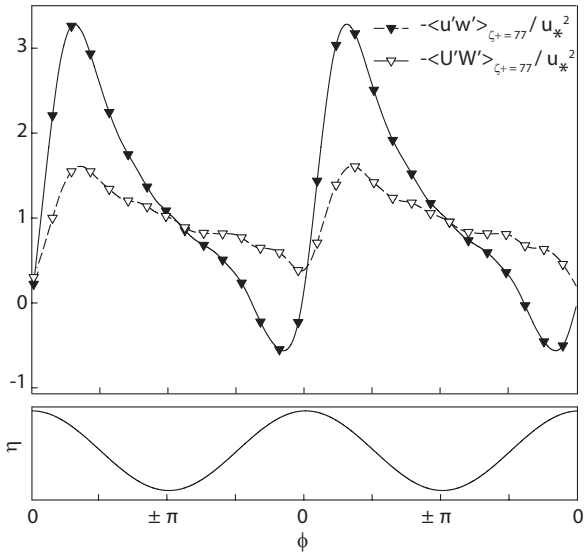

Figure 3.9: Comparison of along-wave mean turbulent stresses, at height $\zeta_+ = 77$, computed in two different frames of reference, over wind waves with U_{10} = 9.41 m s^{-1}. $-\langle U'W'\rangle_{\zeta_+=77}$, on average positive along the entire wave profile, is computed using the along-surface and surface-orthogonal projections of the instantaneous turbulent velocity vectors. $-\langle u'w'\rangle_{\zeta_+=77}$ involves the cartesian turbulent velocity components, and becomes negative upwind of crests.

both the airflow horizontal and vertical velocities. It should be noted also that our results are in broad agreement with predictions by Belcher and Hunt (1998). Furthermore, even over older waves, we contend that the (always weak) wave-orbital-induced horizontal velocity gradient cannot have comparable effects on the turbulence as the vertical gradient associated with turbulent boundary layers. The latter is generally larger and associated with very high shear. Finally, additional proof is provided by the fact that the extent of the negative stress region does not increase with increasing wave age.

Our measurements are in agreement with the remarks of Hudson et al. (1996). We also find that the across-surface fluxes of along-surface turbulent momentum, written here $-\langle U'W'\rangle$, remain on average positive everywhere, even upwind of the waves. In figure 3.9, we show an example of turbulent vertical fluxes of horizontal momentum

($-\langle u'w' \rangle$, called "surface-following cartesian approach" hereafter) and turbulent across-surface fluxes of along-surface momentum ($-\langle U'W' \rangle$, or "fully curvilinear" approach; see additional details in appendix A), at a wall normalized height of $\zeta_+ = 77$, over wind waves with $U_{10} = 9.41$ m s^{-1}. This height was chosen because the differences between $-\langle u'w' \rangle_{\zeta_+=77}$ and $-\langle U'W' \rangle_{\zeta_+=77}$ are large: $-\langle u'w' \rangle_{\zeta_+=77}$ is very negative upwind of the crest and very positive downwind, while $-\langle U'W' \rangle$ remains positive everywhere. Similar effects are present closer to the surface as well (not shown here). We observe that both fluxes vary in a similar manner, in that they decrease upwind of crests, and increase downwind. They also both show dramatic dips in the vicinity of the crest. In fact near the crest is where viscous stresses usually peak (see for example the instantaneous viscous stress plots in panels of figure 3.1 and phase averaged viscous stress plots later in figure 3.18). These reductions in turbulent stress upwind and at the crest are coherent with the assumption that the airflow tends to stabilize and become less turbulent upon approaching wave crests. Relaminarization has been observed in aerodynamics, when a flow enters a region of strongly favorable pressure gradient and accelerates (e.g., Kovasznay, 1970). Incidently, aerodynamicists have also observed that in such favorable (negative) pressure gradient conditions, the occurrence of turbulent sweeps and ejections, that are characteristic of turbulent boundary layers, is usually strongly decreased (e.g., Kline et al., 1967; Kovasznay, 1970).

The wave-coherent mean stresses $\langle \widetilde{u}\widetilde{w} \rangle / u_*^2$ are shown, for all five wind speeds, in figure 3.10. For the four moderate to high wind speed cases ($U_{10} = 5.00$, 9.41, 14.34, and 16.63 m s^{-1}), the general pattern is of positive regions of intense wave stress along most of the upwind face of waves, as well as along most of the downwind face, where the positive stress is slightly less intense. These regions are interlaced with regions of negative wave stress just downwind of crests (intense negative stress) and of troughs (less intense negative stress). The negative stress contours are pinched thin near the surface, such that the negative stress regions are barely connected to the surface, and they broadly widen away from the surface. In the older wave, low wind speed case

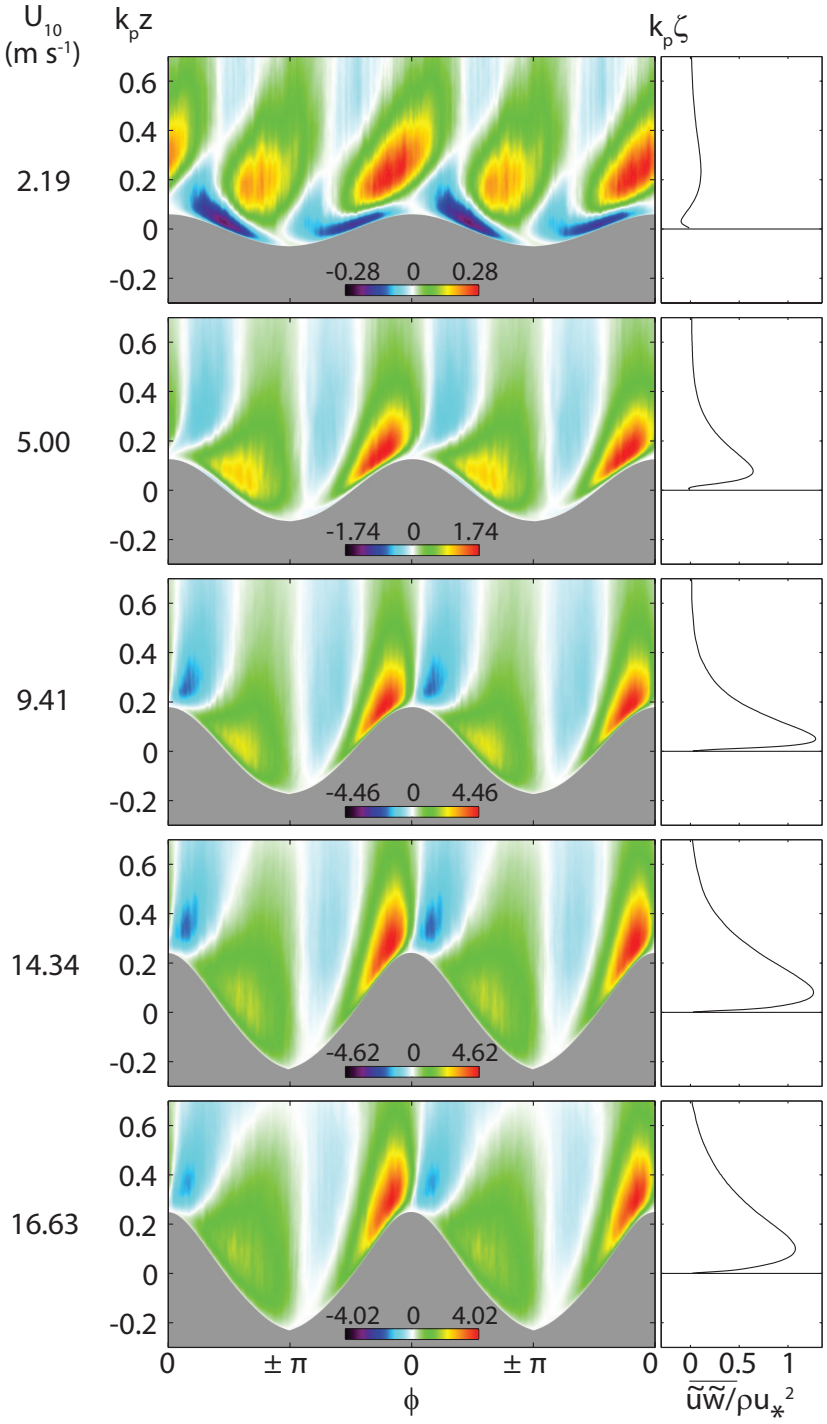

Figure 3.10: Normalized phase averaged wave stress $\langle \widetilde{u}\widetilde{w} \rangle / u_*^2$ (left) and total mean (across all phases) turbulent stress $\overline{\widetilde{u}\widetilde{w}}/u_*^2$ (right). Phase averages are plotted above the phase averaged water surface elevation, and total mean profiles are plotted with respect to the surface following vertical coordinate ζ. Each line corresponds to one experiment, and the corresponding mean 10-m wind speeds are indicated on the left.

however (U_{10} = 2.19 m s^{-1}, $C_p/u*$ = 6.5), while the alternating positive-negative-positive-negative stress pattern exists in a broadly similar form away from the surface, near the surface the mean wave stress pattern is considerably different. Here (figure 3.10, upper panel), the upwind and downwind faces of the wind waves are exposed to regions of negative wave stress, more intense downwind of crests, and slightly less intense upwind. These regions of negative stress are interlaced by slightly positive (and pinched, above troughs) stress regions. Thus, in this case (U_{10} = 2.19 m s^{-1}, $C_p/u*$ = 6.5), the situation is almost exactly the mirror image of the higher wind speed younger wave cases (e.g., U_{10} = 9.41 m s^{-1}, $C_p/u*$ = 2.5). It should be noted that Belcher and Hunt (1998) predicted this effect, and named it a "negative asymmetry" effect. Thus, near the surface, in this older wave case, the airflow behaves as if it were traveling from right to left over stationary solid hills. Away from the surface, starting around $k_pz \sim 0.3$, it behaves like it does over younger waves, i.e. as a flow usually behaves when traveling from left to right over solid hills. This effect is attributed to the forcing of the wave surface orbitals. In fact, the negative asymmetry effect is also well represented by the mean profiles of wave stress (right hand side of figure 3.10). In the lowest wind speed case, we observe on average negative wave stress near the surface, and positive stress away from the surface. The three highest wind speed cases (U_{10} = 9.41,14.34, 16.63 m s^{-1}) show only a peak of positive wave stress near the surface. The moderate wind speed U_{10} = 5.00 m s^{-1}, slightly older wave case (C_p/U_{10} = 4.1), shows a small, near surface kink in the mean wave stress profile, reminiscent of the surface orbital forcing that dominates in the older wave case. These results are in qualitative agreement with results from DNS over monochromatic waves, reported by Sullivan et al. (2000).

3.4.3 Quadrant analysis

In this section, a quadrant analysis (Wallace et al., 1972; Willmarth and Lu, 1972) of the turbulent momentum fluxes within the buffer layer above wind waves, is presented. We follow a similar methodology as Yang and Shen (2010) did with their

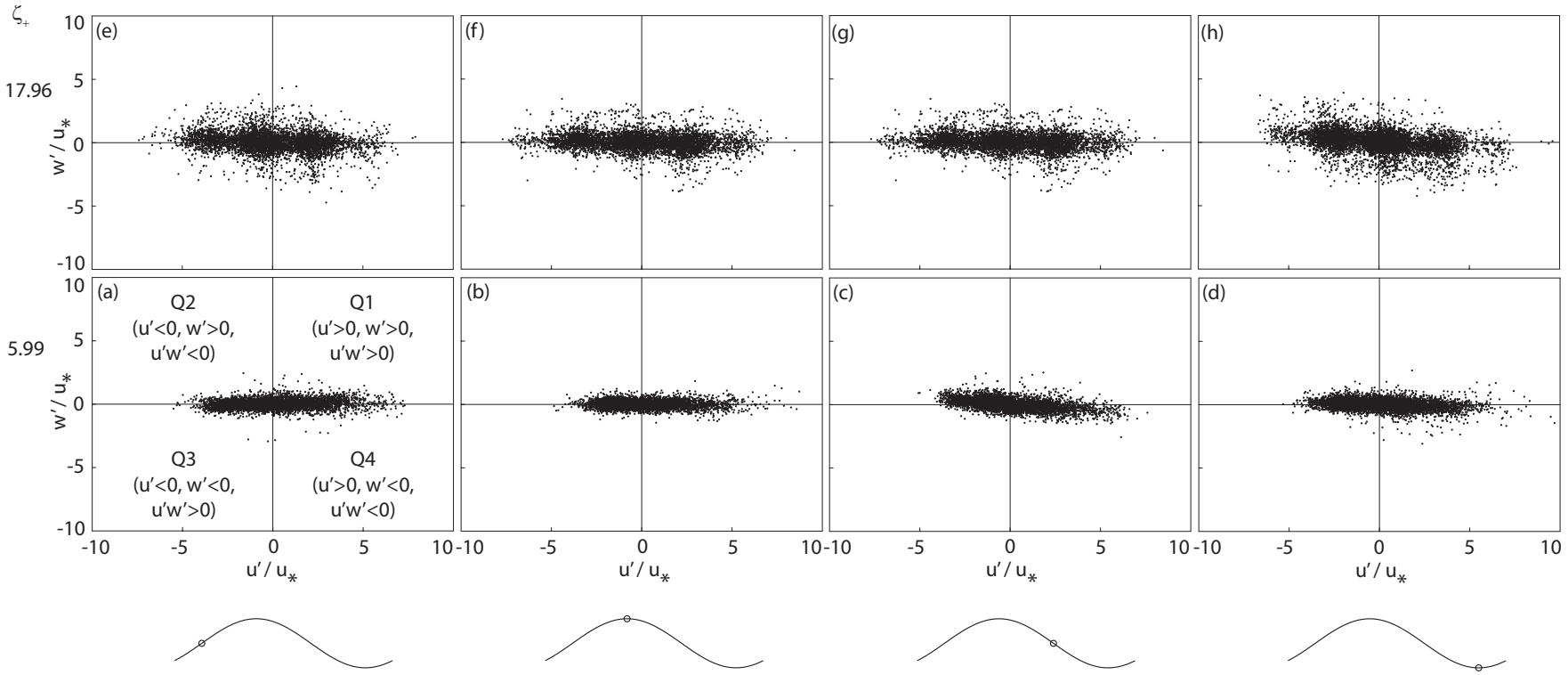

Figure 3.11: Quadrant distributions of normalized turbulent velocity perturbations, w'/u_* versus u'/u_*, above wind waves with $U_{10} = 2.19$ m s^{-1}. Turbulent velocities are measured at two different heights within the sublayer above the wavy water surface. Panels a through d show measurements closest to the water surface, and the data in panels e through h are taken farther away from the surface. Four along-wave phases are chosen: $\phi = (-\pi/2, 0, \pi/2, \pi))$. These locations are sketched below the plots. Quadrants Q1, Q2, Q3, and Q4 are defined in panel a.

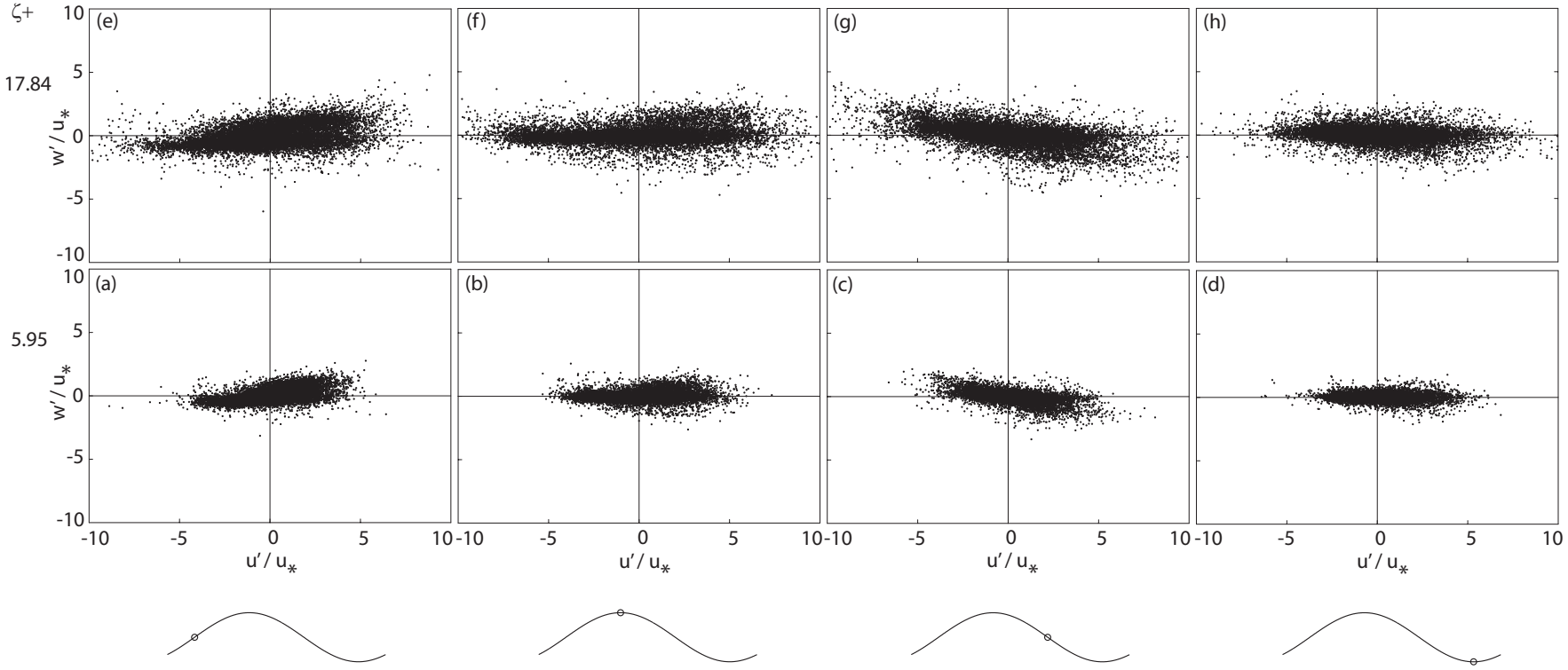

Figure 3.12: As figure 3.11, but for case $U_{10} = 9.41$ m s^{-1}

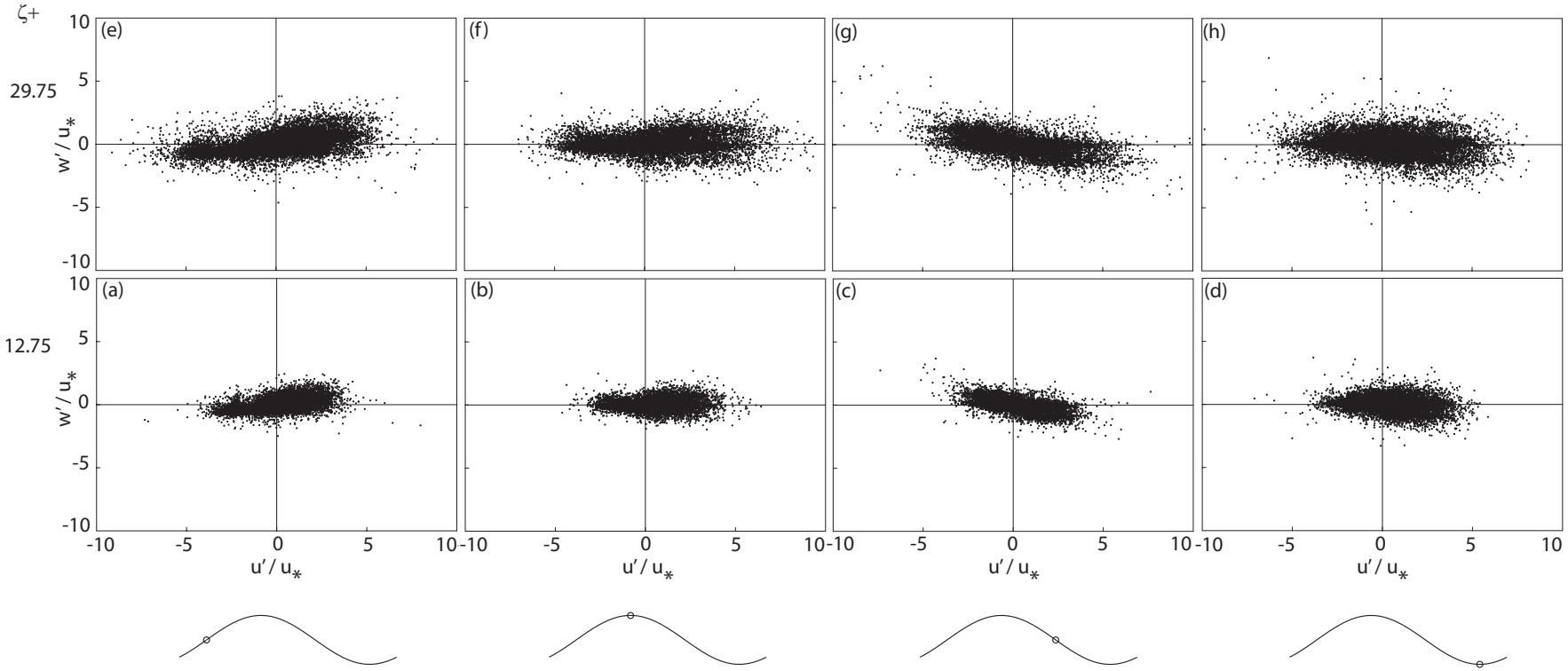

Figure 3.13: As figure 3.11, but for case $U_{10} = 16.63$ m s^{-1}

DNS results over Airy waves: first we present distributions among the four quadrants (defined below) of instantaneous flux events at four different wave phases and two different heights above the water surface (figures 3.11, 3.12, and 3.13), then we discuss the mean contributions of each quadrant to the mean along-wave Reynolds stress (figure 3.14). Like Yang and Shen (2010), for the quadrant analysis, we chose to remain in a surface-following cartesian approach (as opposed, for example, to the fully curvilinear approach of Hudson et al. (1996), discussed earlier), because it is the vertical fluxes of horizontal momentum that are relevant to the understanding and modeling of the coupled atmospheric and oceanic boundary layers.

Here, we show results for wind wave experiments, with 10-m wind speeds of 2.19, 9.41, and 16.63 m s^{-1}. In figures 3.11, 3.12, and 3.13, the lower row corresponds to measurements that are closer to the surface, whereas the measurements in the upper row were taken farther away from the surface, but still within the buffer layer. In past studies of turbulent boundary layers over solid walls, important turbulence-generating structures have been located within the buffer layer (Robinson, 1991). Four different along-wave locations were chosen: the center of the upwind face of the waves ($\phi = -\pi/2$), the wave crests ($\phi = 0$), the center of the downwind face of the waves ($\phi = \pi/2$), and finally the trough ($\phi = \pi$). Plotting turbulent vertical fluctuations w' versus the horizontal fluctuations u', allows to visualize the distribution of turbulent flux events among four quadrants: Q1 ($u' > 0, w' > 0$), Q2 ($u' < 0, w' > 0$), Q3 ($u' < 0, w' < 0$), and Q4 ($u' > 0, w' < 0$). An illustration of the quadrant definitions is provided in panel a of figure 3.11.

Above the wind waves with $U_{10} = 2.19$ m s^{-1}, at a height of $\zeta_+ = 5.99$, on the upwind face of the waves (figure 3.11a), we observe that all quadrants are nearly equivalent, with a very slight dominance of Q1 and Q3 events (slope of linear regression $\alpha = 0.023$, not plotted here). At the crest, all quadrants are equivalent. On the downwind face of the waves, we note a relatively strong dominance of Q2 and Q4 events ($\alpha = -0.1$). At the trough, all quadrants are nearly equivalent again, with nonetheless a slight dominance of Q2 and Q4 events ($\alpha = -0.05$). It is worth mentioning here

that in this experiment ($U_{10} = 2.19$ m s^{-1}), the height $\zeta_+ = 5.99$ is always below the mean along-wave critical height $\langle h_c \rangle$, since $\langle h_c \rangle$ oscillates between $\zeta_+ \sim 7$ and $\zeta_+ \sim 12$ (figure 3.7b, earlier). Past experimental studies (e.g., Kim et al., 1987) have shown that Q2 (ejections) and Q4 (sweeps) type events occur frequently in turbulent boundary layers over flat walls. Earlier, an experimental study by Kline et al. (1967) revealed that such events may occur more frequently in adverse pressure gradient conditions, and less frequently in favorable pressure gradient conditions. This was later confirmed in a review by Kovasznay (1970). Based on the observed along-wave thickening and thinning of the boundary layer, out of phase with the waves by $\pi/2$ (figure 3.7a earlier), we assume that the upwind faces of waves are favorable pressure gradient conditions, and the downwind faces constitute adverse pressure gradient conditions for the airflow above. Thus, the observed Q1-Q3 dominance on the windward side, and the Q2-Q4 dominance on the leeward side of the waves, is in agreement with previous work over solid walls.

Similar patterns are observed outside the critical layer (but still within the buffer layer), at $\zeta_+ = 17.84$. In this case however, all turbulent stress events are much more intense than near the surface. This is a well-known effect in boundary layer turbulence, where turbulence intensity increases with distance from the wall. This is consistent with our previous observations of the instantaneous turbulent airflow properties, that show an increase in turbulent velocity and vortical structures away from the surface.

Over the younger waves at higher wind speeds ($U_{10} = 9.41$, 16.63 m s^{-1}, figures 3.12 and 3.13), we observe at all heights a general pattern of Q1-Q3 events upwind of crests, Q2-Q4 events downwind of crests, and an equivalence of all quadrants above crests and troughs. This is now in full agreement with solid wall results from Kline et al. (1967). Also, similarly to the lower wind speed case ($U_{10} = 2.19$ m s^{-1}, $C_p/u_* = 6.5$), the intensity of the turbulent flux events increases dramatically with increasing height above the surface.

Finally, the differences between the behavior above the older waves and the two younger, higher wind speed waves, is probably linked to the phase shift in the mean

along-wave Reynolds stress, which shows a phase lag (of about $\pi/4$) with respect to all other higher wind speed (younger wave) experiments (see again figure 3.8 above). This phase shift is likely a consequence of the dynamical role of the near-surface critical layer, that isolates the outer flow from the water surface. The critical layer is thought to have a larger role for older waves than for young ones (Belcher and Hunt, 1998), see also chapter 4.

Figure 3.14 shows the contributions of each quadrant to the along-wave turbulent stresses, for experiments with 10-m wind speeds of 2.19 m s^{-1}, 9.41 m s^{-1}, and 16.63 m s^{-1}, respectively. Again, we note strong differences between the lower wind speed case (U_{10} = 2.19 m s^{-1}) and the two higher wind speed ones (U_{10} = 9.41, 16.63 m s^{-1}). In panel a of figure 3.14, we observe that Q2 and Q4 contributions are strong above the downwind face of waves. They are approximately two times more intense than Q1 and Q3. The regions of high Q3 are centered above wave troughs, but they are located relatively far from the surface. In fact, the most intense Q3 related turbulent fluxes start around $k_p z \sim 0.3$, which is where the wave-coherent stresses started showing a similar behavior to the younger, higher wind speed wind waves (see the comments on figure 3.10 in section 3.4.2 above). In this scenario, as was suggested earlier, the mean outer flow is somewhat disconnected from the surface. It is rather coupled with the outside of the critical layer, or critical height h_c. Since $\langle h_c \rangle$ has a phase lag of $\pi/2$ with respect to the water surface, if Q3 fluxes are above the wave troughs, this means that they are also above the downwind face of $\langle h_c \rangle$. In the intermediate wind speed case (U_{10} = 9.41 m s^{-1}), the largest Q3 events are located downwind of crests, but their intensity is also never more than half the intensity of Q2 events. Q2 events dominate, and are located above the leeward face of the waves. The difference in intensity between Q3 and Q2 explains why the scatter plots do not show a dominance of Q3 events on the leeside of the waves (panels c and g of figure 3.12). At this wind speed, Q4 events (sweeps) are also an important contributor to the turbulent stress on the lee of the waves, but they contribute approximately two times less than ejections (Q2) do. However sweep related fluxes remain attached to the downwind face of the waves,

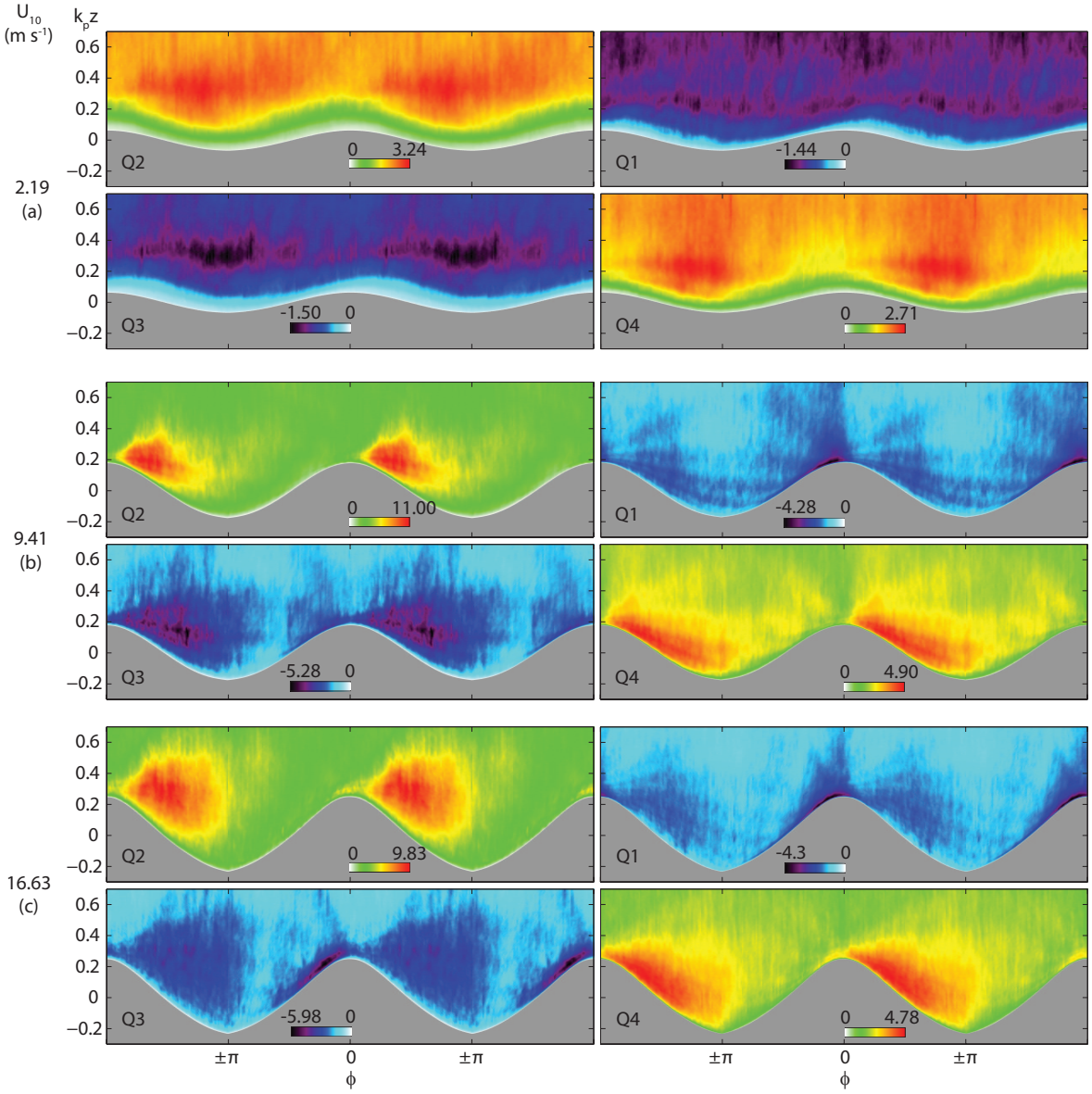

Figure 3.14: Quadrant contributions to the normalized turbulent stress $-\langle u'w'\rangle/u_*^2$, above wind waves for $U_{10} = 2.19$ m s^{-1} (panel a), $U_{10} = 9.41$ m s^{-1} (panel b), and $U_{10} = 16.63$ m s^{-1} (panel c). Q1 and Q3 events are associated with upward momentum flux ($-u'w' < 0$), while Q2 and Q4 events are downward momentum flux events ($-u'w' > 0$).

whereas intense ejection fluxes are concentrated in a jet-like region past the crest. This difference may be due to the difference between separated and non-separated sheltering, which are both important in these wind-wave conditions. Airflow separation truly ejects fluid away from the surface, while non-separated sheltering (caused by the positive pressure gradient due to the down-sloping surface) enhances both Q2 and Q4 events (Kovasznay, 1970). The highest wind speed case ($U_{10} = 16.62$ m s^{-1}, figure 3.14, panel c) shows very similar patterns to the intermediate case (panel b), especially for the Reynolds stress contributions of quadrants Q1, Q2, and Q4. Q3 events contribute to the total turbulent stress on the upwind face of the waves, very close to the surface, and over a large region past the wave crests. The distribution of Q3 contributions is, however, different between panels b and c (figure 3.14). In the case of $U_{10} = 9.41$ m s^{-1}, Q3 events are more important for the flux downwind of crests, whereas for $U_{10} = 16.63$ m s^{-1}, the intensity peaks on the upwind face of the waves. These observations point to the relative contribution of airflow separation to the total stress in different wind-wave conditions. These differences in the along-wave location of the upward momentum flux contributions suggest that at the lower wind speed $U_{10} = 9.41$ m s^{-1}, airflow separation past wave crests is an important contributor to upward momentum flux. In contrast, over the steep waves of the highest wind speed case ($U_{10} = 16.63$ m s^{-1}), it is possible that the relative importance of airflow separation may be less than that of the adverse pressure gradient on the upwind face of the waves. In addition, as we have observed on the instantaneous snapshots panels j and l of figure 3.2, small airflow separation events may occur over the rough upwind faces of waves, at high winds. This could cause, on average, an important upward momentum flux contribution of the upwind face of waves. This mechanism may be an important contributing factor to the reduction of drag coefficients, observed in high wind speed conditions at the ocean surface (e.g., Powell et al., 2003).

3.4.4 Turbulent kinetic energy production

In order to better understand the turbulent mechanisms in the airflow above wind waves, we investigate along-wave distributions of mean turbulence production. If we neglect spanwise variations of the airflow, the mean along-wave turbulent kinetic energy (TKE) production rate P_{TKE} can be expressed as (e.g., Hudson et al., 1996; Yang and Shen, 2010):

$$P_{TKE} = \underbrace{-\langle u'w' \rangle \frac{\partial \langle u \rangle}{\partial z}}_{P_1} \underbrace{-\langle u'^2 \rangle \frac{\partial \langle u \rangle}{\partial x}}_{P_2} \underbrace{-\langle w'^2 \rangle \frac{\partial \langle w \rangle}{\partial z}}_{P_3} \underbrace{-\langle u'w' \rangle \frac{\partial \langle w \rangle}{\partial x}}_{P_4} \tag{3.2}$$

The total TKE production P_{TKE} is presented in figure 3.15, for each experiment. Phase averages are on the left, and means across all phases are on the right. Color plots are provided to show the along-wave distribution of TKE production. However, variations in color intensity from one experiment to another can be misleading, because each plot has a unique data range. Profiles with the same scaling factor for all five experiments are plotted at phases $-\pi/4$ and $\pi/4$, in order to better show the differences in magnitude from one experiment to another.

We observe a number of important features, in general agreement with our previous remarks. At the lowest wind speed ($U_{10} = 2.19$ m s^{-1}), nearly no TKE is produced near the surface, within the critical layer. Upwind of the wave crest, intense TKE is produced within a thin region located at the top of the critical layer. Just before the wave crest, the high TKE production region begins to expand into a jet-like region, which then extends past the crest onto the downwind face of the average wave, up to $\phi \sim \pi/2$. We attribute this expansion of the high TKE region to the bursts of high spanwise vorticity (and high shear) layers away from the surface, that occur frequently in adverse pressure gradient conditions, over the downwind face of the waves (see previous sections of this chapter). These free shear layers are sources of intense TKE production. When $U_{10} = 5.00$ m s^{-1}, once again, P_{TKE} is large within a thin layer that coincides with the critical layer height. However in this case, the

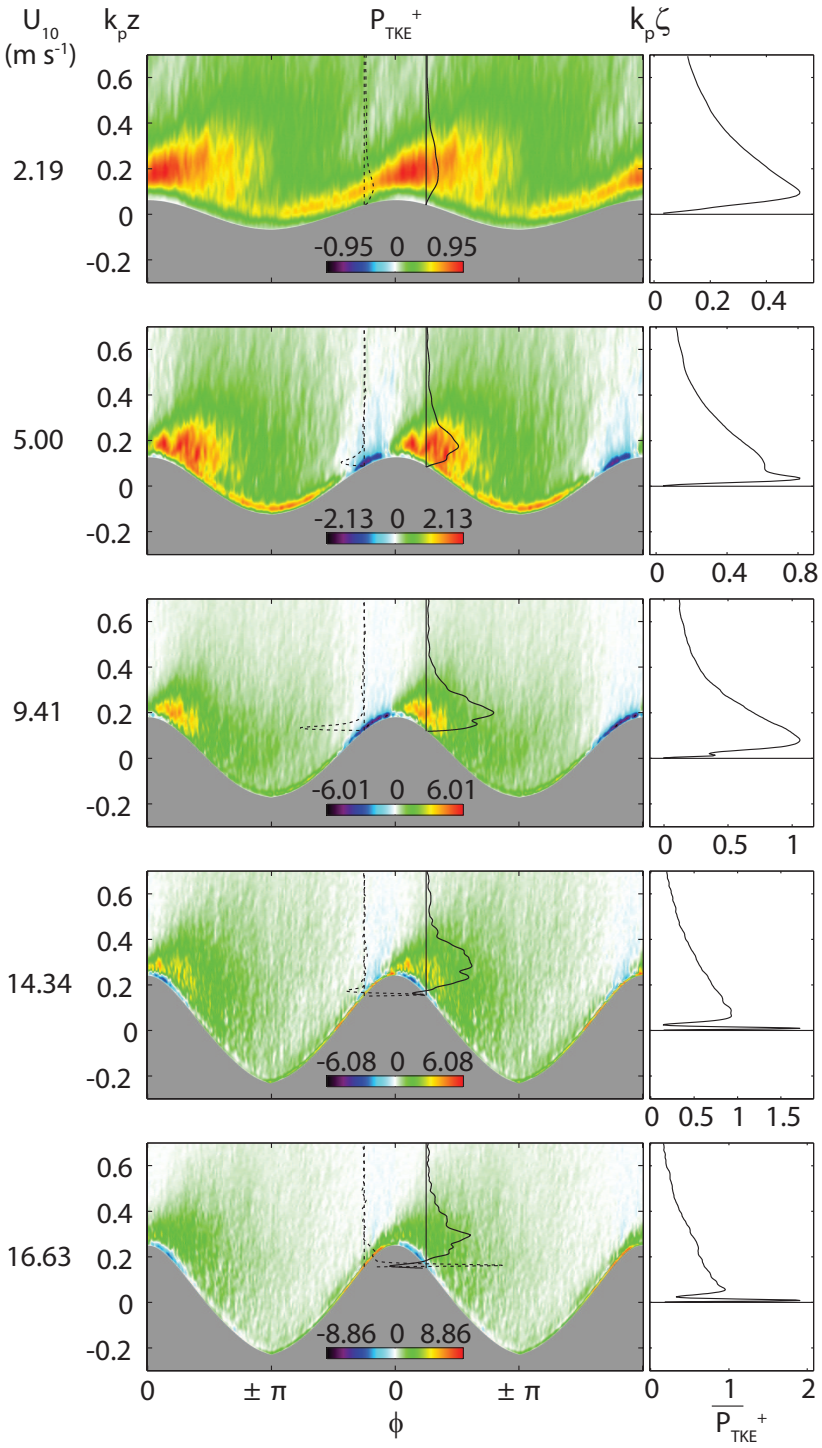

Figure 3.15: Normalized turbulent kinetic energy (TKE) production $P^{+}_{TKE} = P_{TKE}/\left[u_*^2\left(U_{10}k_p\right)\right]$. Profiles with the same scaling factor for all five experiments are plotted at phases $-\pi/4$ and $\pi/4$. Ensemble production averages (across all wave phases) are provided on the right of each phase average field.

TKE is dramatically destroyed ($P_{TKE} < 0$) very near the surface, just upwind of the crests. This can be explained by the intense boundary layer thinning that occurs in that region of highly favorable pressure gradient. In that region, near the smooth water surface upwind of the crests, turbulent motions are reduced, and viscous dissipation is important. In fact, the entire sampled air column above $\phi \sim -\pi/4$ experiences either TKE destruction or at least no production. This result is coherent with the hypothesis of a tendency toward relaminarization of the airflow upon approaching the crest (see section 3.4.2 above). Both of these lower wind speed cases point to an important role of the critical height for the generation of turbulent kinetic energy, at low to moderate wind speeds. At our three highest wind speeds (U_{10} = 9.41, 14.34, 16.63 m s^{-1}), there is no inner layer, free of TKE production. It should be noted that no critical layer was observed at those wind speeds, because the waves are too young (see also wave age considerations later in chapter 4). When U_{10} = 9.41 m s^{-1}, we observe a similar TKE destruction region upwind of crests. This is not surprising, because we had observed on instantaneous snapshots, that at this wind speed, the water surface was generally still smooth upwind of crests (and the viscous sublayer still intact). A jet of high P_{TKE} observed past the crest, can probably now be attributed to airflow separation events, because detached free shear layers are producers of intense turbulence (Ho and Huerre, 1984). This is also observed at the two high wind speeds U_{10} = 14.34, 16.63 m s^{-1}. In fact in these cases, we notice a very thin layer of negative P_{TKE} at the surface past wave crests. This suggests that airflow separation is causing this near surface region to be so sheltered that TKE is destroyed, probably by viscous forces very close to the sheltered surface. Notice that even at lower wind speeds, no TKE is ever produced in that very thin, near-surface, sheltered region. At the two high wind speeds (U_{10} = 14.34, 16.63 m s^{-1}), unlike in the two moderate wind speed cases (U_{10} = 5.00, 9.41 m s^{-1}), there is also a peak in TKE production on the upwind face of the waves, on average. This observation is in agreement with the roughness patterns observed on the upwind faces of waves at these higher wind speeds (e.g., figure 3.2, panels j and l). At the highest 10-m wind speed of 16.63 m s^{-1}, P_{TKE} in that region even exceeds the

TKE production caused by airflow separation.

Next, we show respectively the most important contributing terms to the total TKE production P_{TKE}, noted here P_1 and P_2 (figure 3.16), and the least important ones, P_3 and P_4 (figure 3.17). The strong TKE production terms P_1 and P_2 arguably cause production of horizontal variance $\langle u'^2 \rangle$, whereas the weaker terms P_3 and P_4 cause vertical variance $\langle w'^2 \rangle$ (Yang and Shen, 2010). A general observation is that P_1 and P_2 compete against each other, and P_3 and P_4 do as well. Also, the important terms P_1 and P_2 are generally at least one order of magnitude greater than the less important terms (P_3 and P_4). This means that P_1 and P_2 are the principal contributors to the total TKE production P_{TKE} (figure 3.15). Interestingly, these terms show similar features at all wind speeds: P_1 is negative on the upwind face of waves, and positive on downwind faces, whereas P_2 presents the reversed asymmetry (figure 3.16). Yet the total TKE production P_{TKE} is relatively different from one experiment to another (see comments above). This means that it is the competition between the along-wave magnitudes of P_1 and P_2 that determines the total production P_{TKE}. Broadly, we notice that with increasing wind speed, the magnitudes of P_2 start off smaller than those of P_2 (from $U_{10} = 2.19$ to 9.41 m s^{-1}), and gradually take over and become larger than the magnitudes of P_1 at high wind speeds ($U_{10} = 14.34$, 16.63 m s^{-1}). This effect is also noticeable when looking again at the total TKE production P_{TKE} in figure 3.15: for the two moderate wind speed cases ($U_{10} = 5.00$ and 9.41 m s^{-1}), P_{TKE} is negative on upwind wave faces, and positive downwind (just like P_1, in figure 3.16, left). At the two highest wind speeds, the trend is opposite: P_{TKE} is positive upwind of crests, and negative at the surface downwind of crests. (like P_2, figure 3.16, right). Away from the surface however, above downwind oriented wave faces, P_{TKE} is always positive, i.e., it is controlled by the P_1 term. This is correlated to the phase locked sheltering (separated or not) that occurs systematically past wave crests. The lesser magnitude TKE production terms P_3 and P_3 are also competing against one another: P_3 (figure 3.17, left) is generally negative along upwind wave faces, and positive downwind. The opposite is true for the smallest term P_4 (figure 3.17, right). However in this case,

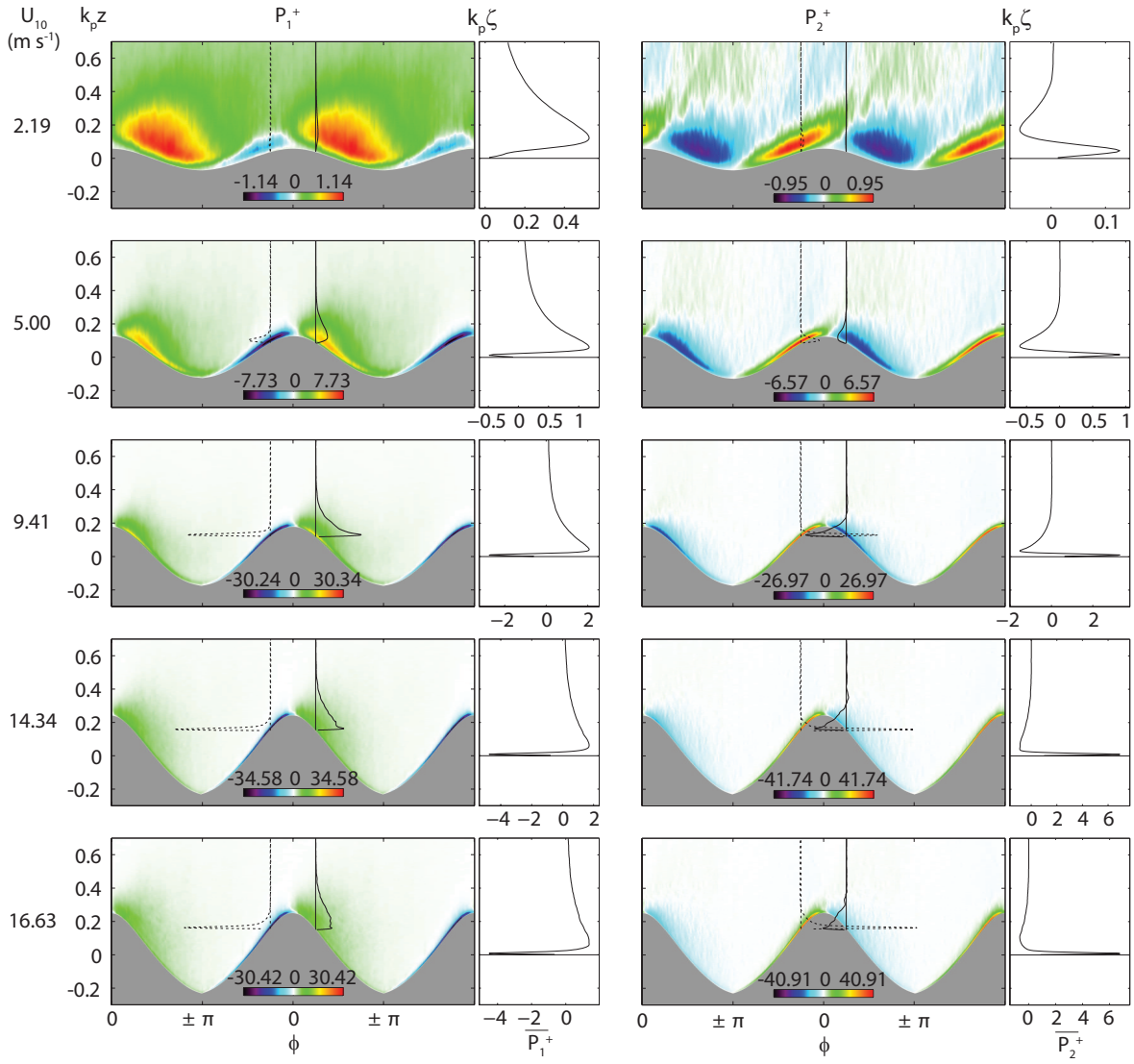

Figure 3.16: Two largest normalized turbulent kinetic energy (TKE) production terms $P_1^+ = P_1/\left[u_*^2\,(U_{10}k_p)\right]$ and $P_2^+ = P_2/\left[u_*^2\,(U_{10}k_p)\right]$. See additional comments in the caption of figure 3.15.

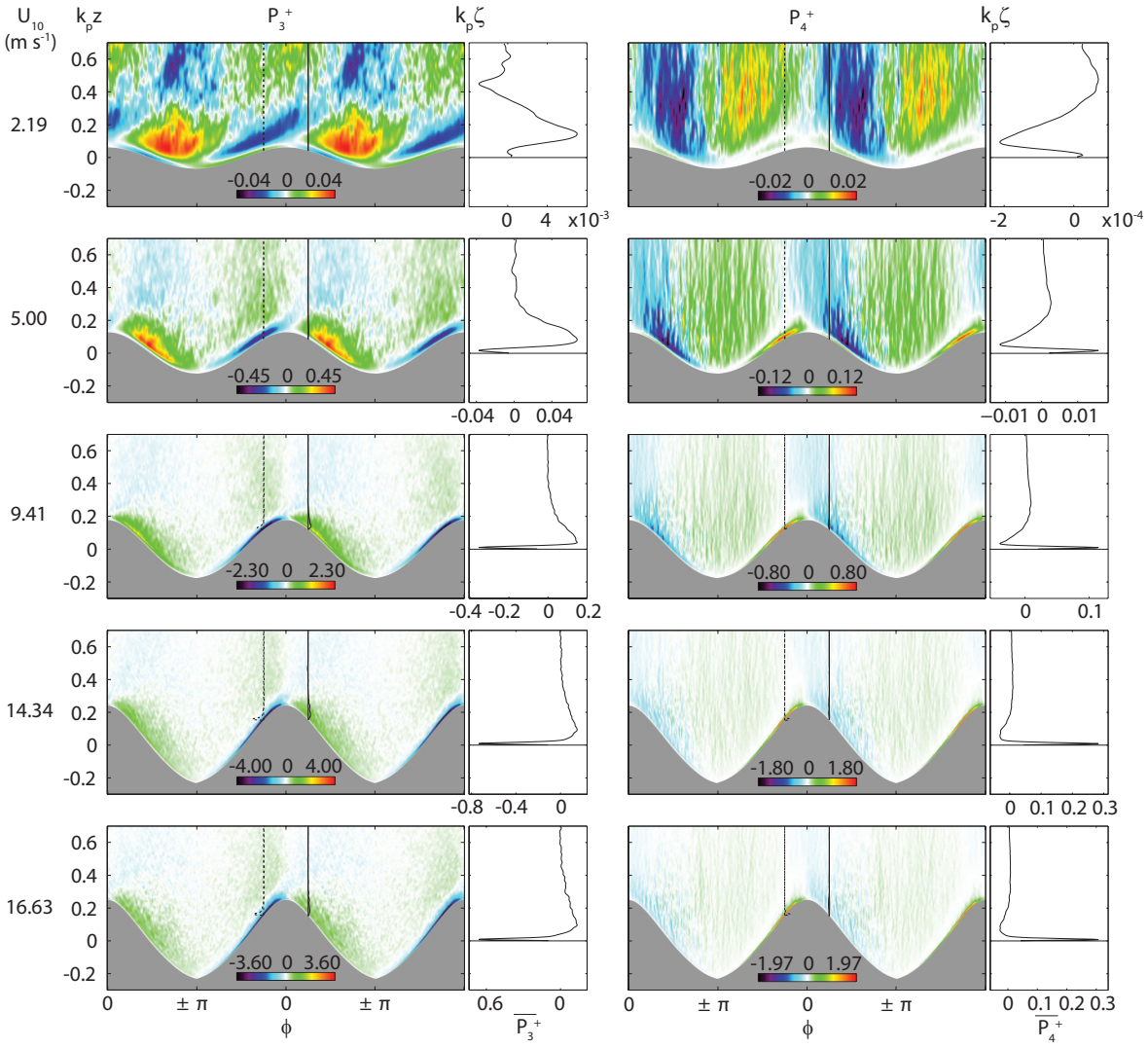

Figure 3.17: Two smallest normalized turbulent kinetic energy (TKE) production terms $P_3^+ = P_3/\left[u_*^2\left(U_{10}k_p\right)\right]$ and $P_4^+ = P_4/\left[u_*^2\left(U_{10}k_p\right)\right]$. See additional comments in the caption of figure 3.15.

the smallest term (right) remains approximately 50% smaller than the largest $\langle w'^2 \rangle$ producing term, and this for all wind speeds.

Within the wave boundary layer, we have noticed important phase-locked features in wave-coherent velocity and momentum fluxes. Turbulent stresses and turbulent kinetic energy production are also strongly wave-phase dependent. In addition, close to the water surface, we have observed dramatic shifts in fluxes and velocity fields (on average and on instantaneous snapshots), compared with the same quantities away from the surface.

3.4.5 Surface tangential viscous stress

In this section, we investigate the along-wave distributions of stresses acting directly on the water surface. The phase averaged surface tangential viscous stresses are plotted in figure 3.18. First, we observe that the mean (normalized) along wave viscous stresses are, at all phases, a non-zero fraction of the total stress ρu_*^2. This fraction decreases with increasing wind velocity. The minimum mean viscous stress to total stress ratio for this study is 0.04, on the leeward face of wind waves with $U_{10} = 16.63$ m s^{-1}. The maximum is 1.1, which occurs just upwind of the crests of wind waves with $U_{10} = 2.19$ m s^{-1}. This means that at high wind speeds, the viscous stress can be virtually negligible, even very close to the surface ($\zeta \sim 300$ μm), while at low wind speeds, the surface viscous stress can be locally larger than the total air-water stress (within the limits of the constant stress layer assumption). The general pattern of the stress variations for all wind wave conditions is a dip at the middle of the leeward side of waves ($\phi \sim \pi/2$), and a peak just upwind of, or at the crest ($\phi \sim 0$). The maximum surface stress location is always upwind of wave crests, and moves downwind with increasing wind speed. We offer two explanations for this varying phase shift as a function of wind speed. First, it is possible that the slower airflow has more time to react to gradual changes in slope of the surface before reaching the crest, whereas the faster airflow does not, and only reacts when a more dramatic slope change occurs, which is generally the case at the sharp crests of higher wind speed wind waves. Second,

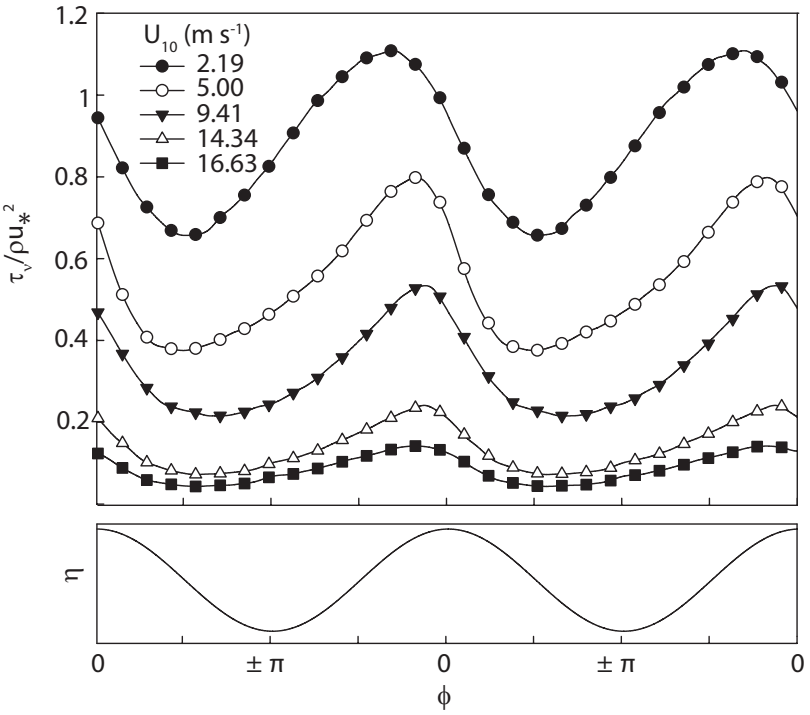

Figure 3.18: Mean along-wave surface viscous stress τ_ν (defined in equation 3.1), averaged between $\zeta = 284$ μm and $\zeta = 664$ μm, and normalized over total stress ρu_*^2. The normalized stresses increase with decreasing wind speed, but note that the dimensional stresses show the opposite trend (shown below). A sketch of a mean wave profile is provided (bottom panel) to help visualize the wave phase.

the wave age and the effect of the surface orbital velocities may have an impact on the distribution of viscous stress along the surface of the waves. In fact, the horizontal surface orbital velocities in the water, are generally maximum and positive at the wave crest. We've mentioned earlier, when looking at the phase averaged velocities in the air (figure 3.6), that the near surface layer of the airflow is increasingly affected by water surface orbital motions, with decreasing wind speed [2]. Such downwind motions of the water particles at the crest may reduce the shear as the airflow approaches the crest. This effect is enhanced with increasing wave age because the relative forcing of the underwater orbital motions is greater.

The contribution of viscous stress to the total stress decreases with increasing wind speed (and increasing wave slope), and yet the dimensional viscous stress follows the opposite trend (see figure 3.19). In particular, the mean viscous stresses remain lower than 0.01 Pa along the low wind speed wind waves (U_{10} = 2.19 m s^{-1}), and the drop in τ_ν past the crest is minimal. The viscous stress oscillates around 0.02 Pa when U_{10} = 5.00 m s^{-1}, and the drop past the crest increases. This may be caused by the increase in wave slope. At wind speeds of U_{10} = 9.41 m s^{-1} and above, we observe first a saturation of the mean trough stress at a value of $\tau_\nu \sim$ 0.025 Pa. This trough saturation is coherent with the onset of airflow separation, which then occurs past more than 50% of the waves. At the highest wind speed (U_{10} = 16.63 m s^{-1}), the mean tangential stress saturates along the entire wave. At the crest, the mean stress is even lower than at the lower wind speed of 14.34 m s^{-1}. The along-wave saturation in tangential stress is coherent with the increased roughness at higher wind speeds. Small roughness elements destroy the viscous sublayer and cause drag to be predominantly turbulent, even very close to the surface. In fact, at the highest wind speed, the water surface may be already so rough on the upwind face of the waves, before reaching the crest, that the airflow is already detached before

[2] This mechanism is studied in more detail in chapter 4, where we show that it is actually related to wave age, not wind speed. In this case, the wave age dependence is not incoherent with the wind speed dependence, because the age of our wind waves decreases with increasing wind speed.

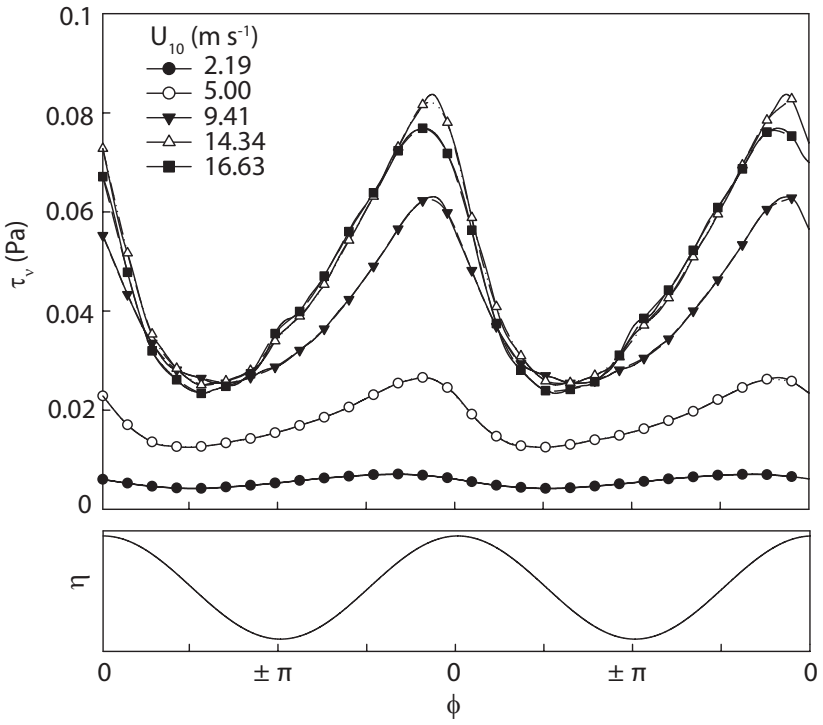

Figure 3.19: Mean along-wave surface viscous stress τ_ν (defined in equation 3.1), averaged between $\zeta = 284$ μm and $\zeta = 664$ μm. The dimensional stresses increase with increasing wind speed, and show signs of saturation at the highest wind speed. A sketch of a mean wave profile is provided (bottom panel) to help visualize the wave phase.

reaching the crest. This would explain the drop in tangential stress above the crest when $U_{10} = 16.63$ m s^{-1}. We should also note that τ_ν presents along-wave asymmetry: The slope of the profiles is always relatively gentle upwind of the stress maximum; past the peak, the viscous stress drops more dramatically. These profile shapes are in qualitative agreement with predictions by Gent and Taylor (1977). Using an eddy viscosity model (Gent and Taylor, 1976), they obtained similar asymmetrical surface shear stress along-wave profiles. They also predicted a dramatic drop in τ_ν past the wave crests, when the mean airflow is separated. Finally, it can be noted that our average along-wave stress values are approximately half of the extrapolated values found by Banner and Peirson (1998). Their study was done at a shorter fetch, with shorter, steeper, slower waves. In addition, their mean values are computed from a small number of scattered measurements. Here, our phase averages are robust, because the mean value in each of the 144 phase bins was computed from at least 12,000 surface tangential stress measurements (and up to 48,000 at the highest wind speeds).

The surface viscous stresses show, on average, important along-wave variability, in all wind wave experiments. Next, we assess the influence of wind speed and friction velocity on the total (across all wave phases) viscous stress, viscous drag, and form drag.

3.5 Mean Viscous Drag: Influences of Mean Wind-Wave Conditions and Airflow Separation

In this section, our mean viscous stress and drag results are first compared with past laboratory studies. Then, we investigate the influence of airflow separation on the viscous, turbulent, and wave contributions to the wind stress.

3.5.1 Mean surface viscous and form stresses as a function of wind speed

In figure 3.20, we present the mean total drag measurements, given by

$$C_d = \frac{\tau}{\rho U_{10}^2}, \tag{3.3}$$

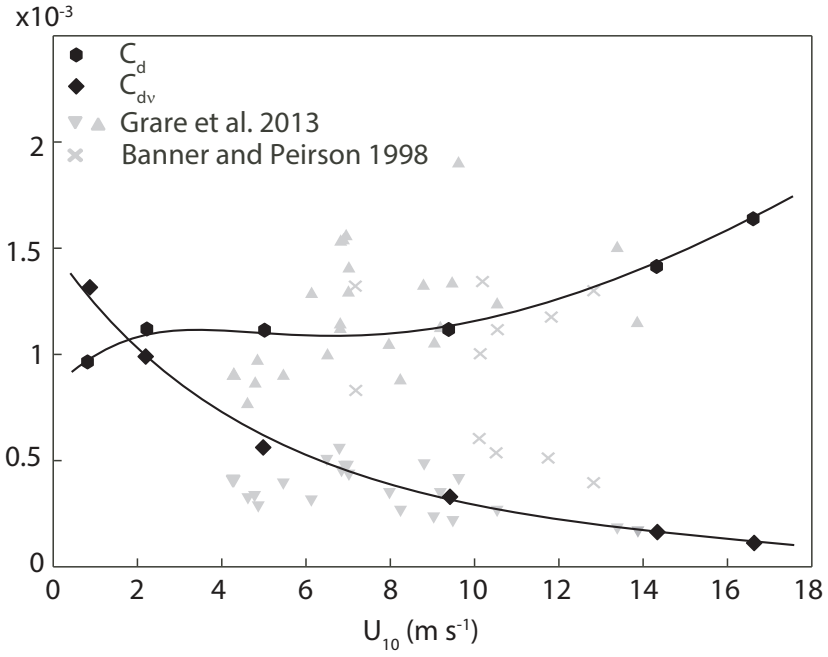

Figure 3.20: Mean total drag (C_d) and mean viscous drag ($C_{d\nu}$) as a function of 10-m wind speed U_{10} (black symbols). Drag definitions are provided in equations 3.3 and 3.4. Additional data are included, extracted from Grare et al. (2013b) and Banner and Peirson (1998) (gray symbols).

where τ is the total wind stress estimated using $\tau = \rho u_*^2$, and the mean surface viscous drag measurements, given by

$$C_{d\nu} = \frac{\tau_\nu}{\rho U_{10}^2}. \tag{3.4}$$

First, it should be noted that our total drag estimates are in good general agreement with measurements by both Grare et al. (2013b) and Banner and Peirson (1998). We observe a leveling off of the drag at low wind speeds, and an increase of the total drag with increasing wind speed. This behavior is coherent with a number of field drag measurements, reported for example by Edson et al. (2013). However, in slight contrast with commonly used parameterizations, at our lowest wind speed, where waves were not detected, we observe a slight drop in total drag, which is in disagreement with the COARE 3.5 parameterization (e.g., Edson et al., 2013).

The viscous drag on the other hand, decreases with increasing wind speed, as was also observed by Banner and Peirson (1998) from underwater measurements, and by Grare et al. (2013b) from air-side measurements. Our viscous drag measurements fall rather well within the results obtained by Grare et al. (2013b), and are approximately 40% lower than those of Banner and Peirson (1998), whose surface stress estimates were obtained by extrapolation. It should be noted here that each stress measurement presented in figure 3.20 is obtained by averaging over 2 million PIV stress measurements taken in the airflow viscous layer at the air-water interface. In addition, unlike estimates by Banner and Peirson (1998) and Grare et al. (2013b), the tangential viscous stress estimates, following the accepted definition of viscous stress (e.g., Kundu and Cohen, 2010), are given by the non-diagonal terms of the viscous stress tensor in a frame of reference with axes respectively tangent and normal to the surface (see equation 3.1 in section 3.2). We find that the viscous stress in these low to moderate wind speeds represents a non negligible contribution to the total momentum flux. This is in agreement with conclusions by Banner and Peirson (1998) and later Grare et al. (2013b).

Next, we deduce form drag estimates, from our viscous stress measurements.

This was also done for example by Grare et al. (2013b).

Assuming that the total stress is constant throughout the airflow boundary layer, it is possible to decompose the across-surface flux of horizontal momentum at the water surface into the sum of a viscous stress contribution and a form stress:

$$\tau = (\overline{\tau_{\nu cc}})_{\zeta=0} + \left(\overline{p\frac{\partial \eta}{\partial x}}\right)_{\zeta=0} = \rho u_*^2 \tag{3.5}$$

where p_η is the pressure at the interface, and $\tau_{\nu cc}$ is the viscous flux of horizontal momentum across the surface, or "cartesian-curvilinear" viscous stress:

$$\tau_{\nu cc} = \mu\left(\frac{\partial u}{\partial \zeta} + \frac{\partial w}{\partial \xi}\right). \tag{3.6}$$

The pressure-slope correlation term (third from the left in equation 3.5) is the form stress τ_{form}. Note that $\tau_{\nu cc}$ is different than τ_ν, which is defined as the viscous flux of along-surface momentum across the air-water interface (see equation 3.1, section 3.2).

In fact, a careful analysis of the momentum balance in a wave following frame of reference shows that the form drag term (pressure-slope correlation) only appears when considering across-surface fluxes of horizontal momentum. This was shown for example by Sullivan et al. (2000) and Hara and Sullivan (2015). More details are provided in appendix A.

In figure 3.21, we present mean form stress contributions to the total stress, as a function of wave slope $a_{rms}k_p$. The results were estimated using equation 3.5. Results from a number of other studies, compiled by Grare et al. (2013b), are also shown. Our form drag estimates show an increase with increasing slope, and fall well within the estimates from others. The increase in form drag and decrease in viscous drag with increasing wind speed and wind wave slope shows that as the wind forcing increases, waves grow steeper, and form drag becomes a large contributor to the total stress. This is in agreement with conclusions by Banner and Peirson (1998) for example.

It has been suggested in the past that airflow separation changes the partitioning

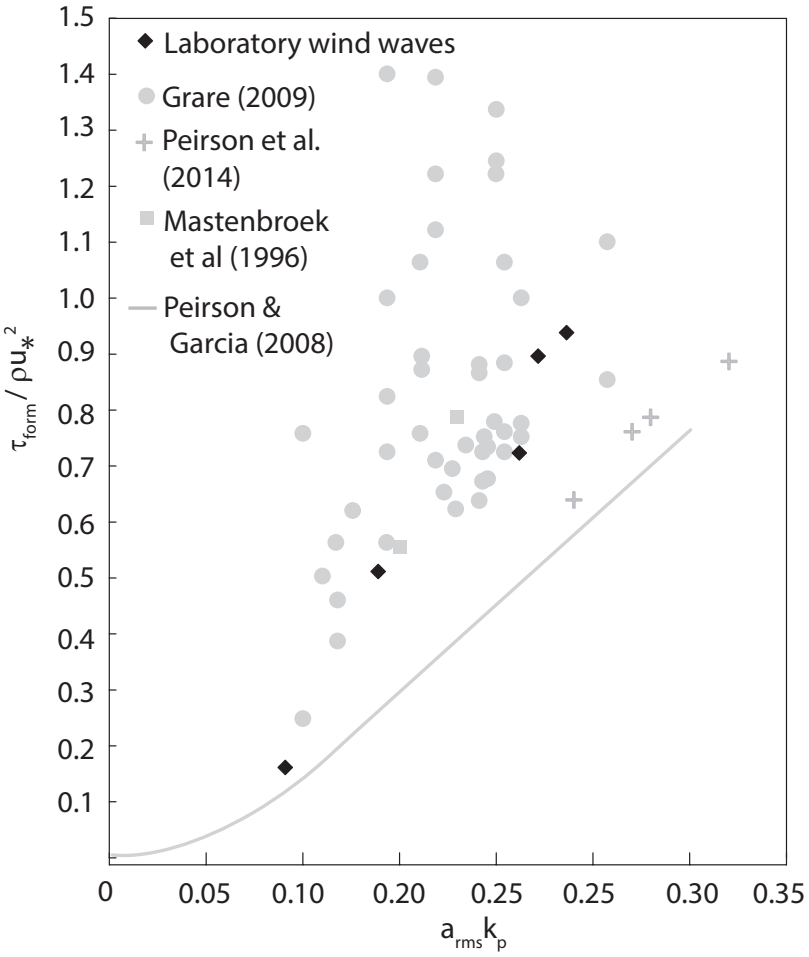

Figure 3.21: Mean form stress τ_{form} normalized over total stress, as a function of wave slope (black symbols). An expression for τ_{form} is provided in equation 3.5. Results from other published laboratory studies are also shown (gray symbols). These were extracted from Grare et al. (2013b). More extreme values of τ_{form}/τ (greater than 1.5 and smaller than 0) reported by Grare et al. (2013b), were omitted.

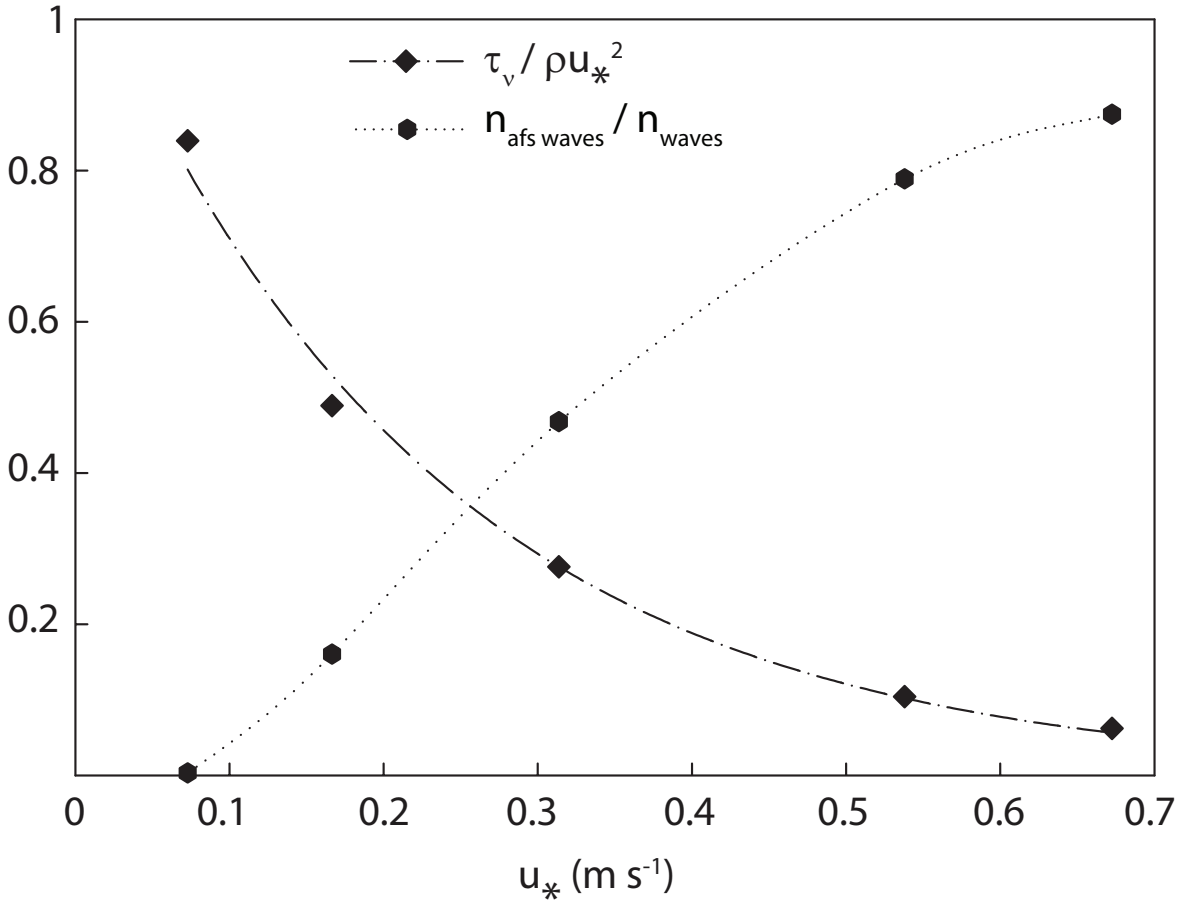

Figure 3.22: Mean viscous stress normalized over total stress, and fraction of airflow separating waves, as a function of friction velocity. Dash-dotted line is an exponential fit of the normalized viscous stress $\tau_\nu/\rho u_*^2$.

of surface stress, between viscous and form contributions (e.g., Jones and Toba, 2001). We estimate next the total form drag, and the effect of airflow separation on the wind stress.

3.5.2 Influence of airflow separation on viscous stresses

In figure 3.22, we report both the fraction of viscous stress over the total stress and the fraction of waves that experience airflow separation, as a function of friction velocity u_*, for all wind wave experiments. While the normalized viscous stress decays exponentially with increasing friction velocity, the fraction of airflow separating waves

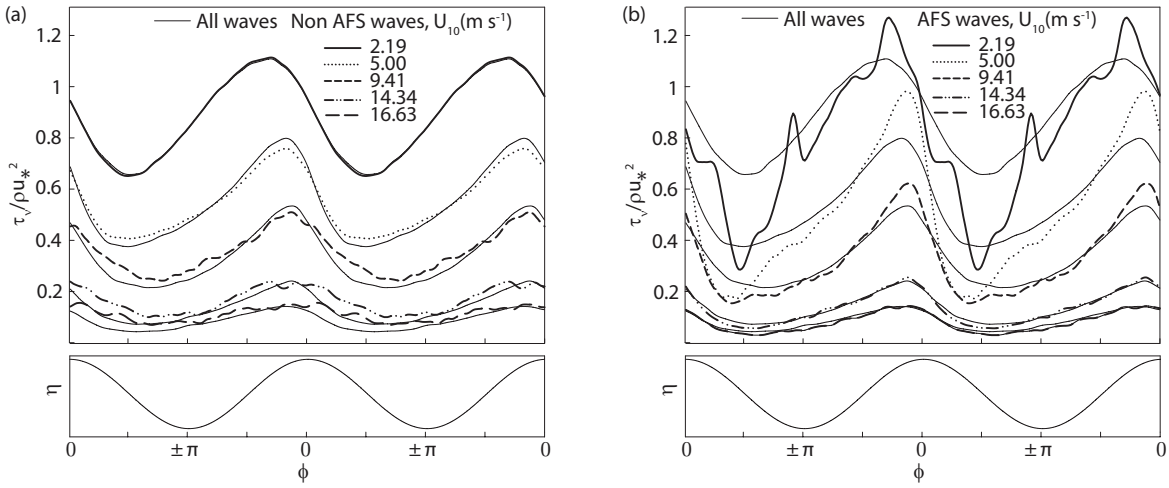

Figure 3.23: Along-wave viscous stresses for non airflow separating waves (a) and airflow separating waves (b). Symbols were replaced by lines for clarity. Thin solid lines represent the phase averaged total viscous stress, already reported in figure 3.18. Thicker lines are the conditionally averaged values.

increases monotonically with wind speed. A wave is considered here to experience airflow separation, when the instantaneous near surface spanwise vorticity drops below zero on the downwind face of the wave. At the lowest wind speed, the airflow separates over 0.4 % of the waves and the surface viscous stress represents 84% of the total stress, whereas at the highest wind speed, 87% of the waves experience airflow separation and the viscous stress is only 0.1% of the total stress. We find that the viscous stress is 50% of the total stress at $U_{10} = 5.00$ m s^{-1}.

The impact of airflow separation is estimated by phase averaging the viscous stress for only airflow separating waves, and that for non airflow separating waves. The results, plotted in figure 3.23, clearly show that airflow separation influences on average predominantly the stress at the crests and at the troughs: at crests, airflow separating waves experience higher than average crest viscous stress, and at the trough, they experience lower than average viscous stress. The increased variability in the plot of the phase-averaged viscous stress at the lowest wind speed in panel b of figure 3.23 is caused by a very reduced sample size, since at that low wind speed ($U_{10} = 2.19$ m s^{-1})

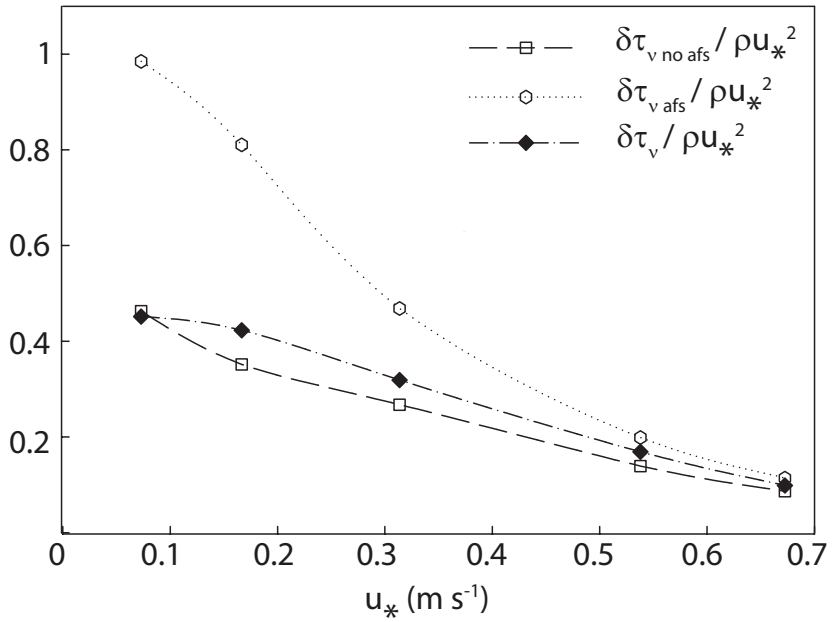

Figure 3.24: Mean normalized maximum differential in mean along-surface viscous stress, as a function of friction velocity u_*. Mean values are given for non-airflow separating waves ($\delta\tau_{\nu \text{ no afs}}$), airflow separating waves ($\delta\tau_{\nu \text{ afs}}$), and all waves ($\delta\tau_\nu$).

only 9 waves experienced airflow separation, out of the 2520 waves sampled at that wind speed. These observations motivate us to look at the effect of airflow separation on the viscous stress differential between crests and troughs, and how this differential is impacted by airflow separation.

Figure 3.24 shows the difference between maximum and minimum mean along-wave viscous stresses, normalized by the total stress, for each experiment. We observe here that the relative importance of airflow separation for the viscous stress contribution (to total stress) is greatest at low to moderate wind speeds, where the viscous sublayer exists in general on the aerodynamically smooth windward face of the waves. At higher wind speeds, the viscous stress is nearly never important for the total stress, whether airflow separation occurs or not, past the crest of the peak waves. The viscous stress differential almost reaches 100% of the total stress when $U_{10} = 2.19$ m s^{-1}. This means that at this wind speed, on waves that show separation, the difference between

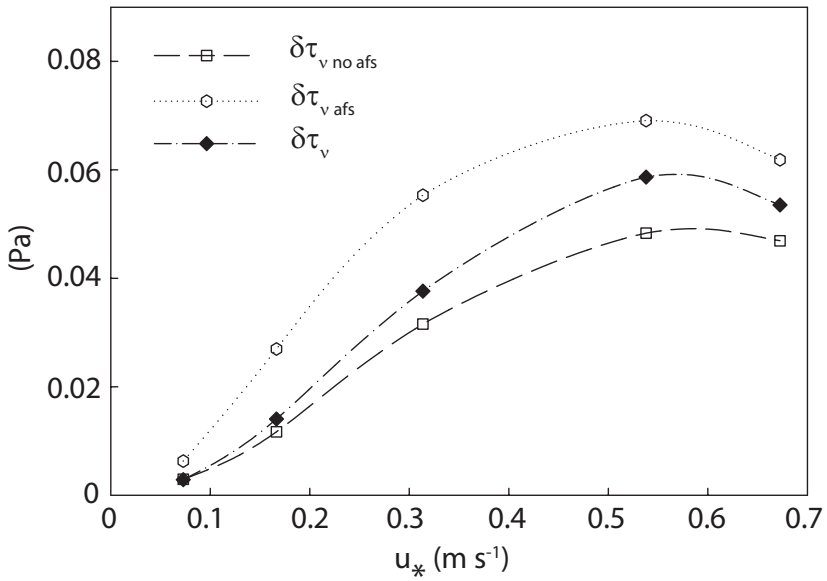

Figure 3.25: Mean maximum differential in mean along-surface viscous stress, as a function of friction velocity u_*. Mean values are given for non-airflow separating waves ($\delta\tau_{\nu no\ afs}$), airflow separating waves ($\delta\tau_{\nu afs}$), and all waves ($\delta\tau_\nu$).

crest and trough is nearly as large as the total wind stress. The stress differential is still approximately 80% of the total stress when $U_{10} = 5.00$ m s^{-1}. Such a dramatic viscous stress difference between crest and trough may have dramatic effects on wave growth. In fact, Longuet-Higgins (1969) showed, using theoretical arguments, that such a phase-locked viscous stress variation is dynamically equivalent to a wave-growth favorable form stress.

If we do not non-dimensionalize the stress differences by the total stress τ, we can see that the dimensional viscous stress differential increases with increasing wind speed, and saturates at the highest wind speed, near $\delta\tau_\nu = 0.05$ Pa (see figure 3.25). For the non-separating and separating wave ensembles, the trend is the same. The absolute difference between $\delta\tau_{\nu afs}$ and $\delta\tau_{\nu no\ afs}$ is greatest at the moderate wind speed ($U_{10} = 9.41$ m s^{-1}, $u_* = 0.31$ m s^{-1}). If we recall the instantaneous observations from section 3.2.2, we should note that this is the highest wind speed where we still observe evidence of an intact viscous sublayer upwind of wave crests.

3.6 Summary and Conclusions

We have presented, for the first time, to the best of our knowledge, high resolution quantitative velocity measurements in the turbulent airflow above surface waves and down to within the viscous sublayer. We were able to achieve high resolution two-dimensional velocity measurements in the airflow above wind waves, in a range of low to high wind speeds, as close as 100 μm above the water surface. We identified coherent turbulent structures in the airflow above waves, that have been, up to now, only observed above solid walls (Adrian, 2007): bursts of near surface spanwise vorticity, and turbulent ejections and sweeps. Airflow separation events, also directly observed, start to appear in low to moderate winds, and are very frequent at high wind speeds. They occur over nearly 90% of the short wind waves at $U_{10} = 16.63$ m s^{-1}. By phase averaging velocities and fluxes within the airflow, we were able to quantify the mean dynamics within the viscous sublayer, buffer and logarithmic layers, as well as below and above the critical height. We found evidence of turbulent boundary layer thinning and thickening over wind waves. Like the boundary layer thickness, the mean along-wave tangential viscous stresses are phase-locked, with maxima just before wave crests, and minima in the vicinity of troughs. Airflow separation dramatically influences instantaneous and mean along-wave viscous stress distributions. This effect is most pronounced when viscous sublayers exist upwind of crests. This is observed only up to certain wind speeds (here up to $U_{10} = 9.41$ m s^{-1}). At higher wind speeds, intense turbulent kinetic energy is produced along the entire wave profile. Finally, we note that at the lowest wind speed $U_{10} = 2.19$ m s^{-1}, the mean properties of the airflow are considerably different within an inner region near the surface (below the critical height), from the behavior farther away from the surface (outside the critical layer). This result is in agreement with previous modelling efforts (Belcher and Hunt, 1998; Sullivan et al., 2000; Kihara et al., 2007; Yang and Shen, 2010). These authors have related this effect to the age of the waves, or the ratio of the wave speed with respect to wind speed. In the following chapter, we investigate the effect of wave age on the structure of airflow.

Chapter 4

INFLUENCE OF WAVE AGE ON THE STRUCTURE OF THE AIRFLOW ABOVE WAVES

4.1 Introduction

In recent years, efforts to estimate drag coefficients at the ocean surface have revealed that drag depends not only on wind speed, but also on wave height, wave slope, wind-wave alignment, and wave age (e.g., Sullivan and McWilliams, 2010; Jones and Toba, 2001). Wave age is important because it is a direct indicator of the coupling between the wind and the waves, which is crucial for the total momentum flux at the ocean surface. Wave age is alternatively defined as C_p/u_*, or C_p/U_{10}. It is the ratio of the velocity of the peak waves C_p, over the velocity of the wind U_{10} or over the friction velocity u_*. In fetch-limited, "local equilibrium conditions" (Csanady, 2001), strongly forced short wind waves move slowly compared to the speed of the wind: they are young. Long swells often move fast with respect to wind speed: they are old. In these idealized conditions, young waves are found at shorter fetches, while older waves are found at longer fetches. The frequency spectrum of waves in the ocean has been found to reach a state of saturation or "wind-wave equilibrium" (Sullivan and McWilliams, 2010), when $C_p/U_{10} \sim 1.2$ (Alves et al., 2003). This is when the spectral density of the wave field reaches an upper limit, because energy dissipation processes are balancing the energy input from the wind (Phillips, 1977). Young seas with waves ages C_p/U_{10} below 1.2 are often called "wind-driven wave regime", and when $C_p/U_{10} > 1.2$, the wind is "wave-driven" (Sullivan and McWilliams, 2010).

Modelers have suggested that wind-wave coupling mechanisms differ significantly from one regime to another (Belcher and Hunt, 1998; Kihara et al., 2007), but

experimental evidence is scarce, and wave growth mechanisms are still not fully understood (Sullivan and McWilliams, 2010). In particular, two competing theoretical approaches have been the subject of vigorous debate: Miles' (1957) quasi-laminar critical layer wave generation theory, and Belcher's and Hunt's (1993) sheltering hypothesis. In Miles' theory, which is based on linear stability analysis of a stratified shear flow, turbulent (and viscous) stresses are considered negligible very close to the water surface, and waves cause an air-side shear instability which in turn forces them to grow. Belcher and Hunt on the other hand, suggest that turbulent stresses above waves are spatially distributed in such a way (with respect to wave phase) that they force a thickening of the boundary layer past the average wave, which is favorable to wave growth. As suggested by Sullivan and McWilliams (2010), this mechanism is common in aerodynamics, where an average thinning/thickening of a turbulent boundary layer is known to occur upstream/downstream of an obstacle. In the case of waves, this implies a wave-coherent distribution of stresses along the wave profile (form drag and viscous shear stress), which are both favorable to wave growth. In fact, the distribution of viscous stress related to phase-coherent boundary layer thinning and thickening, has been suggested by Longuet-Higgins (1969) to have the same dynamical effects on wave growth as wave-coherent normal stresses (with a $\pi/2$ phase lag). Away from the surface, water waves affect the turbulence in the airflow in such a way that measurements of turbulence over solid wavy boundaries (e.g., Kendall, 1970) are not quite sufficient to address this need. When turbulence is included in a wind-wave coupling theory, the closure problem requires a modeling effort that can only be validated by turbulence measurements above actual waves (Hsu et al., 1981). In fact, the mechanisms by which momentum is transferred across the air-sea interface are further complicated not only by the intermittent occurrence of airflow separation events, which may strongly impact the air-sea momentum flux (Banner and Melville, 1976), and start to be significant even in low to moderate wind speeds (see for example Veron et al. (2007) and the present chapter), but also by wave breaking and sea spray generation.

In this chapter, we present high resolution two-dimensional measurements of

the airflow above waves with a wide range of wave ages. The data were obtained in the laboratory, using a complex experimental system specially developed for this study. The setup is described in detail in chapter 2. In section 4.2, the instantaneous turbulent structure of the airflow is discussed. It presents features reminiscent of turbulent boundary layers over flat plates (e.g., ejections and sweeps paired with detached high vorticity layers) and over solid wavy boundaries (e.g., airflow separation), but the surface signatures of underwater dynamics specific to water surface gravity waves (e.g., orbital velocities) also dramatically influence the turbulent airflow, starting at relatively low wave ages ($C_p/u_* = 6.5$). These results, when presented alongside mean wave-coherent velocities and fluxes in section 4.3, point to the complex interactions between mean and instantaneous turbulent effects on wind-wave coupling, which in turn may impact the total momentum flux across the air-water interface.

4.2 Instantaneous Fields

In figure 4.1, we show examples of instantaneous 2D velocity fields (horizontal component $u(x, z, t)$, plotted in color) in the air above water, for five different wind/wave conditions, plotted above the raw LFV images of the water (water is plotted in gray). The water surface is very different from one experiment to another. No detectable waves are generated by the lowest wind speed $U_{10} = 0.86$ m s^{-1} (figure 4.1a). Old wave age conditions are achieved by blowing similar low winds over mechanically generated swells (figure 4.1b). Only a fraction of a swell wavelength (approximately 55%) is visible here. The wind in this case doesn't generate any significant waves. At moderate wind speeds, the wind-generated waves are typically non-linear, with relatively flat troughs, sharp crests with capillary waves just past the crests (figure 4.1c). The waves steepen with increasing wind speed (figure 4.1 panels d and e), and many are visibly breaking, generating bubbles in the water and spray in the air (not visible here). Also, the water surface becomes covered with small roughness elements ($O(1cm)$). The grayscale part of the image that is below the water surface is the signature of the underwater part of the LFV laser sheet, refracted through the water surface. This data is

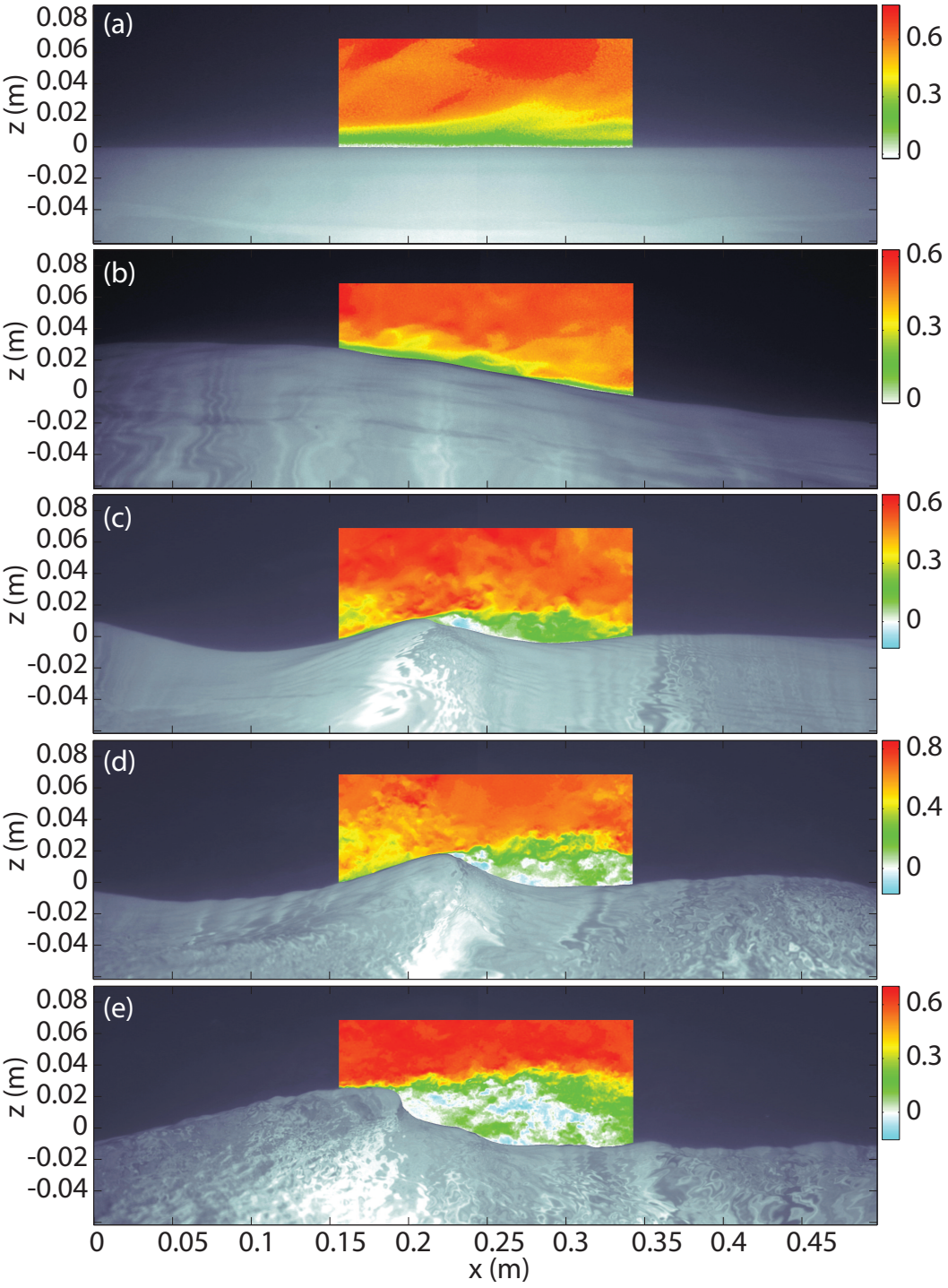

Figure 4.1: Examples of instantaneous velocity fields u/U_{10} plotted over LFV images. (a) $U_{10} = 0.86$ m s^{-1}, (b) $U_{10} = 1.40$ m s^{-1} with mechanical swell, (c) $U_{10} = 5.00$ m s^{-1}, (d) $U_{10} = 9.41$ m s^{-1}, (e) $U_{10} = 14.34$ m s^{-1}.

difficult to exploit quantitatively, but does give a qualitative (albeit distorted) picture of the structure of the surface.

The airflow velocity fields above the air-water interface also display clear differences from one wind/wave condition to another. In figure 4.1a, no waves are being generated, but within the buffer layer, low velocity fluid is intermittently being ejected away from the water surface, which is also characteristic of the near-wall region in turbulent boundary layers over flat plates, where most of the turbulent stress and kinetic energy throughout the boundary layer are produced (e.g., Kline et al. 1967, and also reviews by Robinson 1991 and by Jiménez 2011). Later PIV investigations over flat plates (Meinhart and Adrian, 1995; Adrian, 2007) have reported similar "low momentum ramps" (Jiménez, 2011). Ejections (or "Q2 events", see below) and sweeps (or "Q4 events", i.e., higher velocity fluid swept down toward the surface, also perhaps visible in figure 4.1a, near the downwind edge of the velocity field) have been attributed to the presence in the buffer layer of quasi-streamwise vorticity streaks, sweeping and ejecting fluid to and from the boundary (Kim et al., 1971; Robinson, 1991; Jiménez, 2011)), but also to hairpin vortices (Adrian, 2007). The contours of low streamwise velocity (u component) ejected away from the interface are strongly tilted downwind and inevitably cause free shear (spanwise vorticity[1]) layers to exist at the interface between these regions and the surrounding faster (streamwise) moving fluid. Such high vorticity layers are further discussed in chapter 3. Also, these intermittent ejections may in turn impact the distribution of turbulent stress (shear but also pressure-driven) along the surface, and thus be an important factor in the initial stages of wind-wave generation through turbulent near-surface pressure variations (Phillips, 1957). In figure 4.1b, where the low wind is blowing over the leeward face of a mechanical swell, the ejections appear less intense and more confined to the surface, in spite of the adverse pressure gradient (caused by the presence of the tilted water surface). This observation

[1] It can be noted here that these shear-related elongated vorticity structures are not vortical, but merely due to high shear. This is supported by a study of the swirling strength (Zhou et al., 1999), which is included in chapter 3

is not consistent with the work of Kline et al. (1967) who noticed an intensification of ejections in adverse pressure gradient conditions. But now the near-surface airflow is also strongly influenced by the wave surface orbital motions, as well as the forward translation of the wave profile. These motions of the boundary render the wind-wave problem more complex than the case of a solid flat plate, and may impact the turbulence throughout the entire boundary layer (see below).

The airflow above the wind waves in panels c, d and e of figure 4.1 appears to be separating past the crest of the waves, leading to the formation of a sheltered region of very low (near zero) air velocity downwind of the crest. Airflow separation events were observed in the laboratory over wind waves by Chang et al. (1971), Kawai (1981), Kawamura and Toba (1988), and later Veron et al. (2007) over wind waves. However, due to their transient and intermittent nature, separation events within turbulent boundary layers are not easy to define or detect, even over solid boundaries, as was emphasized by Simpson (1989). The conditions for the occurrence of airflow separation over surface gravity waves have been the subject of debate, especially since Banner and Melville (1976) and later Gent and Taylor (1977) suggested that this may only occur over breaking waves, or in conjunction with strong near-surface underwater drift currents (Gent and Taylor, 1977). Banner and Melville (1976) showed theoretically that in the monochromatic linear limit, if a wave doesn't break (i.e., there is no stagnation point at the interface, in a frame of reference moving at phase speed C_p), continuity of vorticity (shear) across the interface prevents the airflow from separating. The intermittency of airflow separation events above waves adds to the difficulty of obtaining experimental evidence. In this study, we consider that the airflow separates if the near surface high vorticity layer characteristic of an attached boundary layer (Wu et al., 2006; Veron et al., 2007) is ejected away from the water surface (shown later in figure 4.4), and the surface spanwise vorticity downwind of the point of detachment is zero or negative. The detached high vorticity layer (due to high shear) may then be a source of intense turbulence away from the water surface. Identifying such events requires high resolution measurements very close to the surface. The frequency

of occurrence of airflow separation past wind waves, is discussed in detail in chapter 3.

In this chapter, we focus on the effect of wave age on the structure of the airflow above waves. Over fast, old mechanically generated swells, the PIV field of view is only a small fraction (approximately 16%) of the wavelength of the waves. Hence figure 4.1 doesn't show a full picture of the dynamics above all phases of the large mechanical waves. To provide a more comprehensive overview, instantaneous fields taken at different times are displayed side-by-side in figures 4.2, 4.3, and 4.4. This yields a picture of the airflow above at least one full wave. The snapshots are taken at intervals of respectively 0.28 s (for $C_p/u_* = 3.7$, and 6.5) and 0.14 s (for $C_p/u_* = 6.4$, 19.1, and 27.7), with time decreasing from left to right. The general pattern over the younger waves is that u increases above crests and decreases above troughs, and w is positive upwind of crests and negative downwind of crests. Over the older waves ($C_p/u_* = 27.7$), the trend is reversed: the airflow very clearly moves downward over the upwind face, and upward over the downwind face of the waves (figure 4.3e), and u shows ejections of low velocity fluid predominantly upstream of the crest (figure 4.2e). Most of the areas where u is lower, display high positive vorticity structures away from the surface. When u is high near the surface, the spanwise vorticity is high and positive (and due to high shear) at the surface, which is characteristic of attached boundary layers (Wu et al., 2006). When the near surface velocity decreases, the boundary layer thickens, and the surface high vorticity layer may thicken as it is less constrained to the surface by the velocity gradient, and may in some cases dramatically detach from the surface past the crest of steep waves, causing airflow separation (figure 4.4a). At the higher wind speeds, most detached free high vorticity layers appear to disintegrate and shed a number of small scale vortices (figure 4.4, panels a and b). At lower wind speeds (figure 4.4, panels c, d, e), detached high vorticity layers remain somewhat coherent even away from the surface. The lifetime of these coherent structures is discussed in detail in chapter 3. It should be noted that the airflow separation that takes place in figure 4.4a is not only characterized by a detachment of the surface high vorticity layer, but also a total absence of a surface

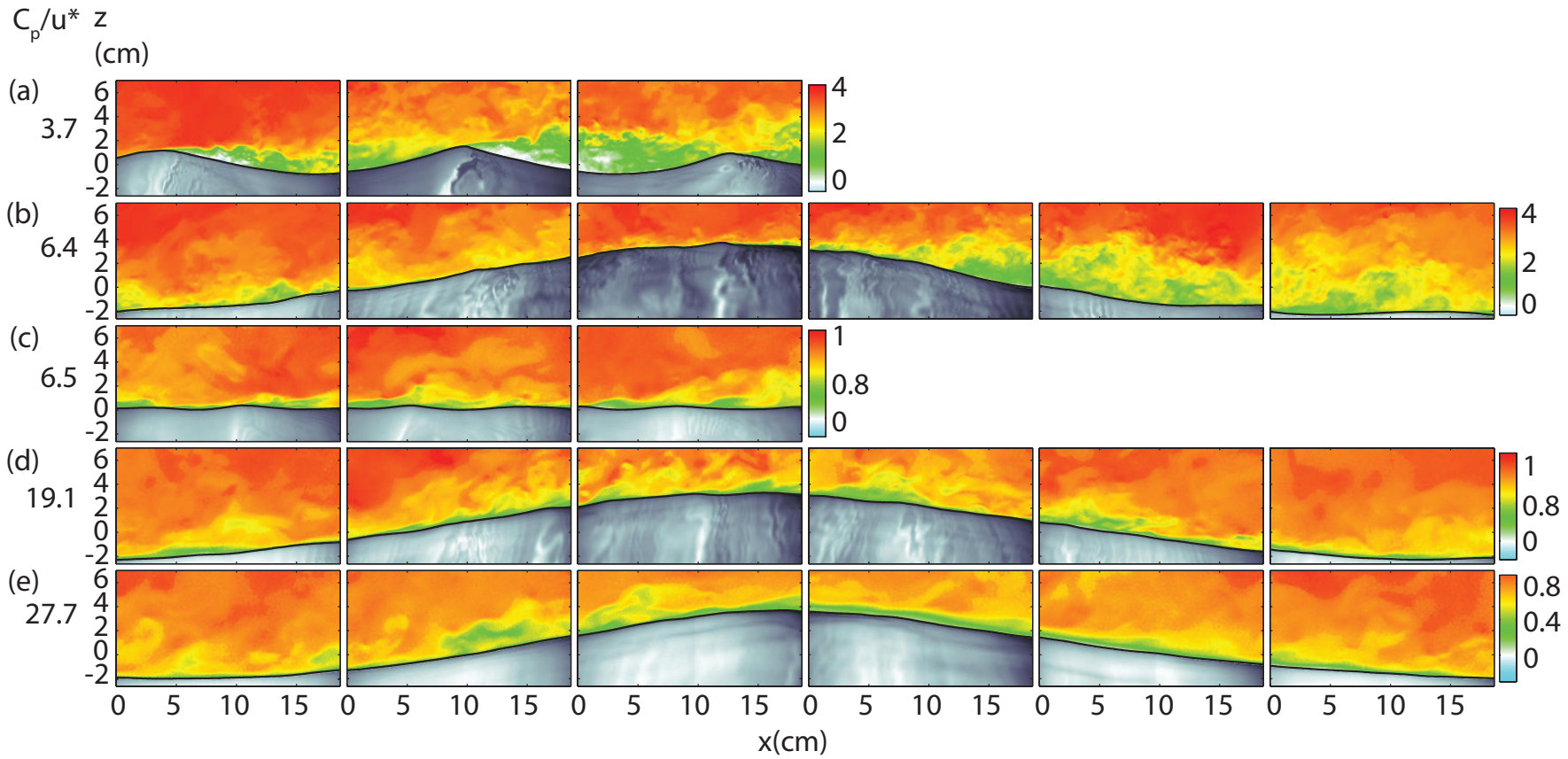

Figure 4.2: Instantaneous horizontal velocity fields u (m s^{-1}), above segments of waves. Each row contains consecutive snapshots from one experiment. Mean wave age C_p/u_* for each experiment is given on the left.

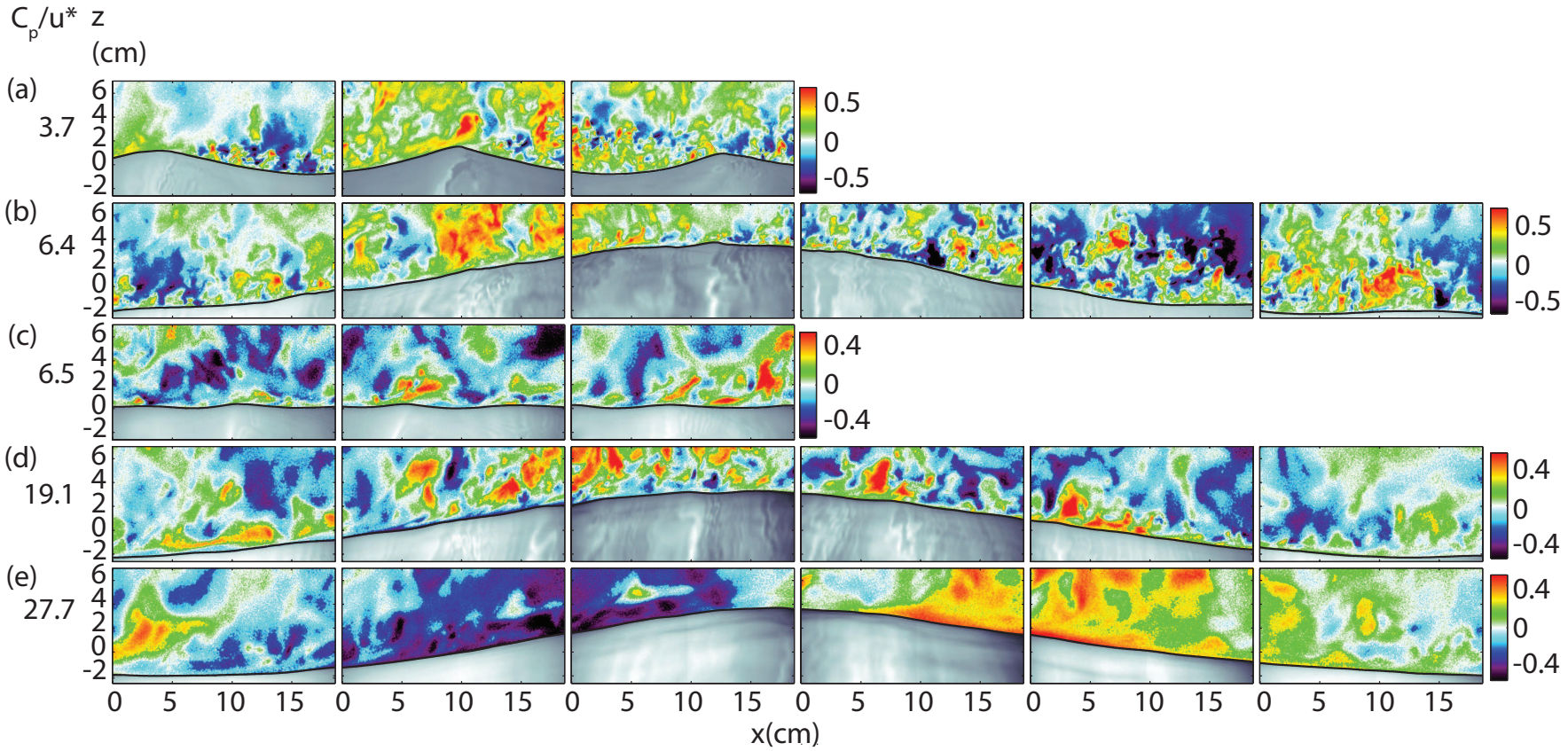

Figure 4.3: Instantaneous vertical velocity fields w (m s^{-1}), above segments of waves. Each row contains consecutive snapshots from one experiment. Mean wave age C_p/u_* for each experiment is given on the left.

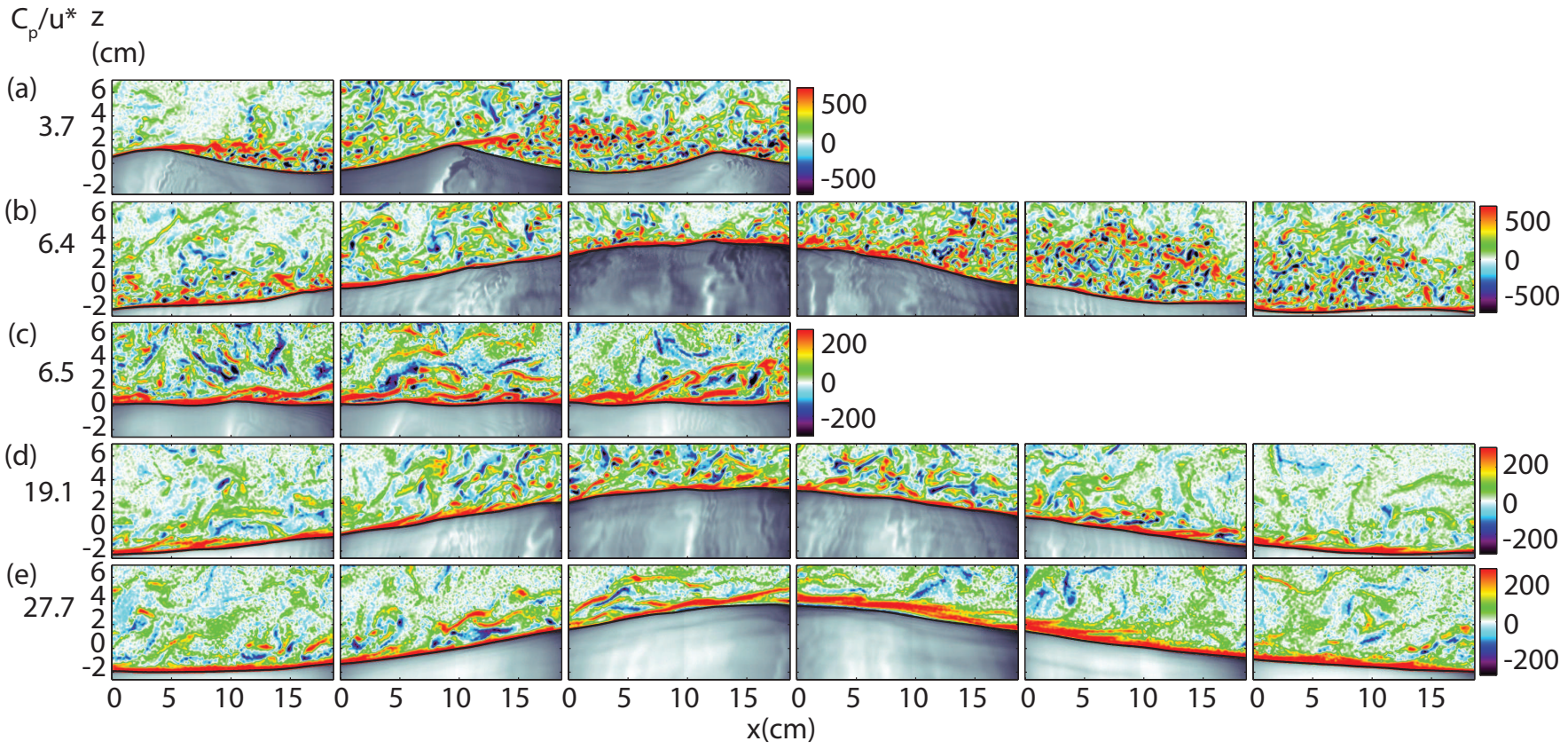

Figure 4.4: (a) Instantaneous vorticity fields ω (m s^{-1}), above segments of waves. Each row contains consecutive snapshots from one experiment. Mean wave age C_p/u_* for each experiment is given on the left.

vorticity layer in the sheltered region, which indicates a clear separation of the flow from the boundary (Simpson, 1989). Nonetheless, after careful observation of figure 4.4c, one can notice that the high vorticity layers (probably linked to low velocity bursts, as stated above) predominantly originate from the surface just past wave crests, which would be coherent with the assumption that they occur more frequently in adverse pressure conditions (Kline et al., 1967). In this sense, the (albeit very small) waves in figure 4.4a are beginning to "organize" the structure of the turbulence in the airflow (see averages of turbulent quantities later in section 4.5), since free high shear layers are presumably important sources of turbulent production. Finally, it is worth noticing that panels b and e (figure 4.2) are (very broadly) "mirror" images of one another, in the sense that figure 4.2b shows turbulent boundary layer thickening downwind of the crest: green and yellow structures extend up to a certain height above the surface, and figure 4.2e shows (again very broadly) similar structures upwind of the crest. The vorticity fields (figure 4.4, panels b and e) yield a similar picture: in figure 4.4b, detached vorticity structures are predominantly downwind of the crest, while in figure 4.4e, they are mostly upwind. These observations hint to a later result in this chapter, which is that old enough waves may cause a "reversed sheltering effect" (see below) or "negative streamline asymmetry" (Belcher and Hunt, 1998).

4.3 Phase Averaged Velocities

In figure 4.5, we examine the phase averaged velocities in the airflow in a frame of reference moving with the waves at phase speed C_p, for three experiments with different wave ages C_p/u_*. The first two experiments are wind-generated waves (with wave ages $C_p/u_* = 3.7$, and 6.5), and the third is with wind blowing over mechanical swell, which allows us to achieve an older wave age of 31.7. The phase averaged horizontal velocity field $(\langle u \rangle - C_p)/U_{10}$ shows a phase-locked thickening of the boundary layer that occurs on average past the crest of the younger waves (figure 4.5, panels a and b), and the thickening of the (reversed) airflow above the older waves (figure 4.5c) occurs very slightly upstream of the crest. Note that in this frame of reference, in all three

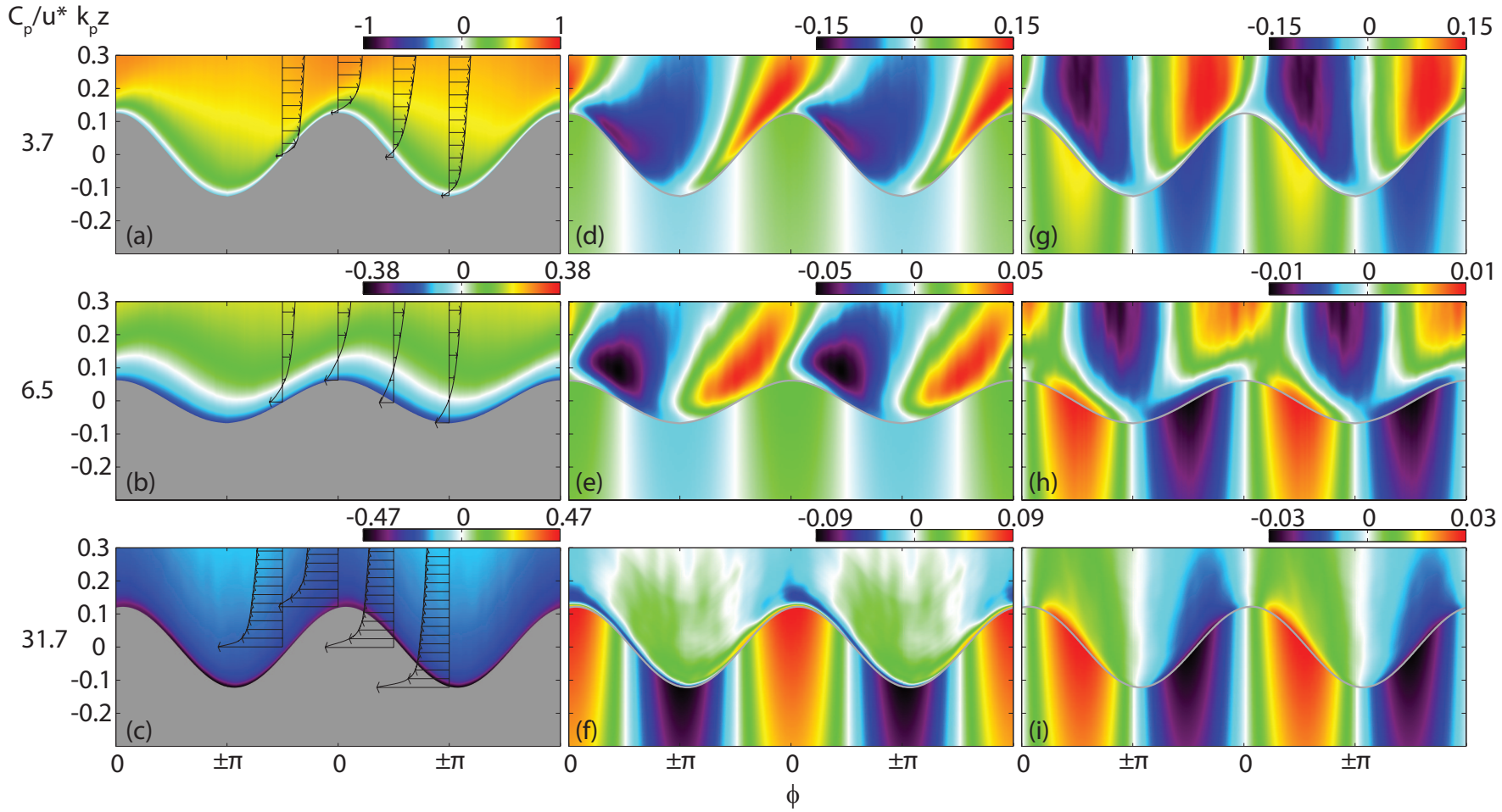

Figure 4.5: (a,b,c) $(\langle u \rangle - C_p)/U_{10}$: phase averaged horizontal velocities in the air above waves, in a frame of reference moving at peak phase speed C_p. (d,e,f) Measured wave coherent horizontal velocities are plotted in the air ($\widetilde{u}/U_{10}$), and the horizontal component of the underwater wave orbital velocities (computed) are plotted below the water surface. (g,h,i) Mean measured vertical velocities $\widetilde{w}/U_{10}$ in the air, and vertical underwater orbital velocities. Data in the air is measured; data in the water is computed from linear wave theory.

cases, the airflow is reversed within a layer near the surface. The thickness of this flow reversal layer (or "critical layer", Miles (1957)) appears to increase with increasing wave age. In the old wave case, this layer may extend very high, since $U_{10} \sim C_p$. In the youngest wave case, the mean thickness of the critical layer is very small ($\overline{\delta_c} = 0.7$ mm), with 0.4 mm $< \langle \delta_c \rangle <$1.1 mm. In the older wind wave case, we have $\overline{\delta_c} = 1.9$ mm, with 1.5 mm $< \langle \delta_c \rangle <$ 2.7 mm. In both cases, the critical layer follows (with a lesser amplitude than the surface, especially in figure 4.5b) the undulations of the surface, with a positive phase lag (downstream shift) of approximatively $\pi/4$. We may point out here that without the relatively high resolution of the near-surface measurements achieved in this study, the existence of a critical layer over these relatively young wind waves ($C_p/u_* = 6.5$) may have been overlooked.

The wave-coherent (or wave "perturbation", e.g., Belcher and Hunt, 1998) velocities $\widetilde{u}/U_{10}$ and $\widetilde{w}/U_{10}$ display different patterns within versus outside the critical layer. Above the critical height, $\widetilde{u}/U_{10}$ follows an alternating positive-negative pattern, with downwind tilted velocity contours. (This is only visible in panels d and e of figure 4.5, since the field of view in panel f doesn't extend any higher than a fraction of the critical layer.) One would expect such patterns over solid hills. This sheltering effect was predicted by Belcher and Hunt (1998), and modeled by direct numerical simulation (Sullivan et al., 2000; Kihara et al., 2007), but only over monochromatic sinusoidal waves and solid hills. Within the near-surface critical layer, the velocity contours are tilted upwind. This is very clear in figure 4.5, panels e and f. In figure 4.5d, since the critical layer is so thin, most of the wave perturbation field shows downwind tilted velocity contours. Nonetheless, sharp kinks in the velocity contours are visible very close to the surface, (for example at $\phi = -\pi/2$); this provides further evidence of the existence of a critical height below which wave surface orbitals influence the airflow, even over these relatively young waves, in a fixed frame of reference (this time not moving at peak phase speed C_p). Notice that the upwind tilted positive-negative contours in figure 4.5f can be seen as a mirror image of the downwind tilted positive-negative patterns in figure 4.5d. This reverse sheltering effect was already somewhat hinted at

by the instantaneous structures of velocity and vorticity in figures 4.2, 4.3, and 4.4. At the surface, the positive/negative $\widetilde{u}/U_{10}$ velocity contours in the air above these old waves (figure 4.5f) are connected to (and of the same order as) their underwater positive/negative counterparts. A possible interpretation is that, very close to the surface, the surface orbitals of the old waves (traveling from left to right) are generating a horizontal airflow perturbation reminiscent of a flow traveling in the opposite direction (from right to left). Away from the surface (but still below the critical height, since in this old wave case, with $C_p/u_* = 31.7$, the critical height is very large), $\widetilde{u}/U_{10}$ follows a pattern coherent with linear wave theory: negative values above crests, and positive values above troughs (e.g., Kundu and Cohen, 2010). Miles' critical layer theory predicts this pattern below the critical layer (e.g., Hristov et al., 2003).

The vertical wave-coherent velocities $\widetilde{w}/U_{10}$ also show two distinct patterns, below and above the critical height. Below, the measured airflow velocities match well with the underwater orbitals, especially for the two older wave cases (figure 4.5, panels h and i). It is important to mention here that the data presented above the surface are the PIV measurements, while the results presented below the wave-phase averaged surface are calculated from linear water-wave theory. Over the younger waves (figure 4.5g), since the critical layer is so thin, the matching with underwater orbitals is not as obvious, although the negative underwater orbitals do appear to have a slight influence on the airflow very close to the surface (for example over troughs, just past $\phi = \pi$). The fact that this matching only occurs for the (negative) velocities at that particular phase, may be due to the effect of sheltering (separated or not), since the latter causes systematic velocity reduction over troughs, whereby the flow is probably "slow" enough with respect to C_p (i.e., the "local wave age" at that phase is large enough), such that the orbitals influence significantly the airflow. Above the critical height, the alternating negative-positive patterns are dramatically phase-shifted upwind with respect to the underwater patterns. This suggests once again that at those heights, the airflow is not influenced by the orbitals, but rather by the forward traveling wave form. This phase shift $\delta\phi$, of approximately $\pi/2$ in figure 4.5h, is even more dramatic over the younger

wave case where $\delta\phi \sim \pi$ (figure 4.5g).

4.4 Mean Wave Fluxes

The mean wave coherent stresses, plotted in figure 4.6, vary dramatically as a function of wave age, wave phase, and height above the water surface. Over the younger waves (figure 4.6a), the phase averaged wave coherent stress $\langle\widetilde{u}\widetilde{w}\rangle/u_*^2$ is intense and positive upwind of crests, and slightly less intense and positive downwind of crests. These large (and downwind tilted) jets of positive flux are interlaced with narrower less intense negative flux contours. These are tilted downwind above crests, and are nearly vertical (no tilt) above troughs, just past $\phi = \pi$. This is also the phase at which the negative surface orbitals are able to "draw" the airflow downward (figure 4.5), as suggested in the previous section (4.3). The zones of negative flux exist because the contours of the horizontal component of the wave perturbations are tilted downwind, while the vertical component's are not tilted. So within those zones, while the airflow is still being "perturbed" downwind/upwind, it is also being "perturbed" downward/upward. This effect doesn't appear to be specific to moving water waves; it is presumably also present when sheltering occurs over a solid wavy boundary (Sullivan et al., 2000). This suggests that over young wind waves, the wave form is controlling the mean wave flux in the airflow. Over the older wind waves (figure 4.6b), similar sheltering patterns in the wave stress are also present (with less tilting) away from the surface, though the negative zones are not represented here, because they occur above $k_p z = 0.3$. Near the surface on the other hand, contours of intense negative wave stress are located over the upwind face and the downwind face of the waves. These contours are tilted upwind, and while they are more intense than the underwater stresses, they appear nonetheless to be continuous across the interface (and match the theoretical underwater estimates).

In the two wind wave cases, the mean wave stress $\overline{\widetilde{u}\widetilde{w}}/u_*^2$ is negative below the critical layer, and positive above. Over the younger steeper waves, the mean positive wave stress represents over 60% of the total stress ρu_*^2, at $k_p\zeta = 0.09$ (figure 4.6d). The near surface negative wave stress within the very thin critical layer is comparatively

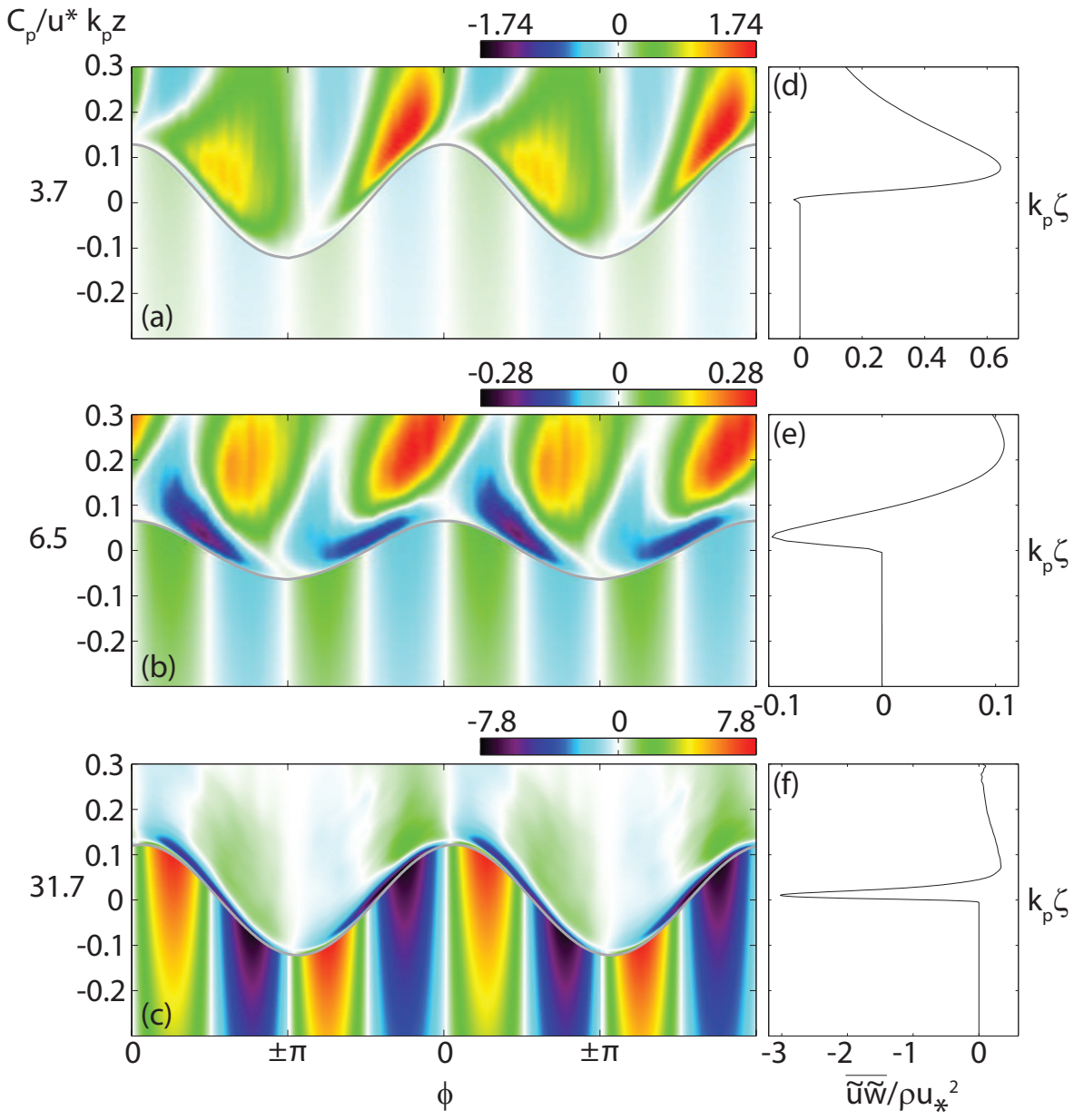

Figure 4.6: (a,b,c) Normalized phase averaged wave stress $\langle \widetilde{u}\widetilde{w} \rangle / u_*^2$. (d,e,f) Total mean (across all phases) wave stress $\overline{\widetilde{u}\widetilde{w}}/u_*^2$ (right). Phase averages are plotted above the phase averaged water surface elevation, and total mean profiles are plotted with respect to the surface following vertical coordinate ζ. Each line corresponds to one experiment, and the corresponding wave ages are indicated on the left.

very small (less than 1% of the total stress). Over the older wind waves, the mean negative/positive wave stress reaches roughly 10% of the total stress below/above the critical height (figure 4.6e). Over the old mechanical waves ($C_p/u_* = 31.7$), the near surface negative flux reaches extreme values (on average 300% of the total stress), which means that the wave orbital motions are strongly forcing the airflow near the surface. The mean stress also becomes positive away from the surface, even though we are still well within the critical layer, but this slight "overshoot" is probably just a kinematic consequence of the very (upwind) tilted and very negative near surface horizontal perturbation velocities (figure 4.5f) which "bleed" over to the contours of negative vertical velocities (figure 4.5i) between $\phi = -\pi$ and $\phi = 0$. Similar results were found by Sullivan et al. (2000) by direct numerical simulation over monochromatic waves (C_p/u_*,ak) = (22.7,0.1). They obtained a near surface negative momentum flux that reaches just over 100% of the total stress, and a slightly positive overshoot above. Our waves are older and slightly steeper (C_p/u_*,ak) = (31.7,0.12), which could partially explain our larger values.

4.5 Turbulent Variances and Fluxes

The phase averaged sum of horizontal and vertical turbulent variances $\langle u'^2 + w'^2\rangle/u_*^2$ is plotted in figure 4.7 (panels a,b and c), for the same experiments as in the previous section. In figure 4.7a, there is on average a phase-locked jet of intense turbulence past the crest of the waves, away from the surface. We attribute this to airflow separation, whereby high shear layers intermittently detach from the crest of steep waves. Detached (from the surface) free shear layers are sources of intense turbulence away from the surface. Examples of these layers are represented in figure 4.4. It is worth mentioning that although airflow separation only occurs over a fraction (under 20%[2]) of all the waves considered to compute the phase averaged field in figure 4.7a), the turbulence generated by these sporadic events is so intense that it dominates the

[2] Separation events were detected automatically using criteria on the near-surface viscous shear and vorticity in the air. Additional details are provided in chapter 3.

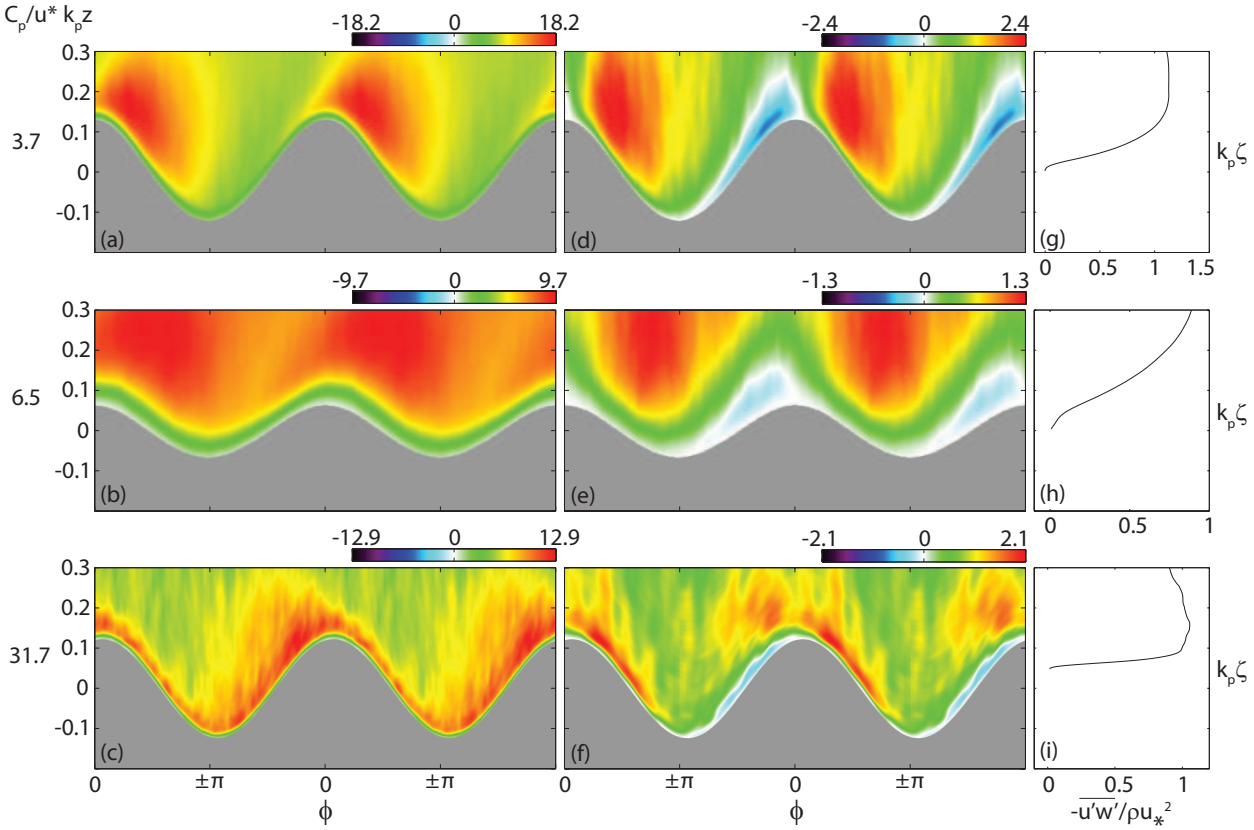

Figure 4.7: (a,b,c) Normalized phase averaged sum of turbulent variance $\langle u'^2 + w'^2 \rangle / u_*^2$. (d,e,f) Normalized phase averaged turbulent stress $-\langle u'w' \rangle / u_*^2$. (g,h,i) Total mean (across all phases) turbulent stress $-\overline{u'w'}/u_*^2$. Phase averages are plotted above the phase averaged water surface elevation, and total mean profiles are plotted with respect to the surface following vertical coordinate ζ. Each line corresponds to one experiment, and the corresponding wave ages are indicated on the left.

average. Flow separation past solid periodic hills has been found to generate an average intensification of the turbulent kinetic energy away from the surface downstream of the hill (e.g., Breuer et al., 2009). Over the older wind waves, $\langle u'^2 + w'^2 \rangle / u_*^2$ is also intensified downwind of crests and away from the surface (figure 4.7b), but this process is not nearly as pronounced as in figure 4.7a. Also, above the critical layer, the background turbulence remains relatively high. These observations can be better understood by looking again at figure 4.4c. There are a number of detached high spanwise vorticity structures (negative and positive) present up to some distance (up to approximately 3 cm) away from the surface above nearly the entire section of water surface plotted here. These are probably sources of turbulence everywhere (at all phases). Figure 4.7 is only representing the turbulence within the first 5 mm ($k_p z < 0.3$), where thick (and detached) high vorticity layers are the norm. It can be noted that in figure 4.4c, these free shear layers remain intact, even away from the surface, whereas in figure 4.4a for example, detached free shear layers, more intense than in figure 4.4c by a factor of 2 or more, disintegrate into small vortices very quickly past the crests. On the other hand, the older mechanical waves cause on average an intensification of the turbulence on the upwind side of the waves (figure 4.7c). This pattern is a reversed picture of what happens outside the critical layer over wind waves (figure 4.7, panels a and b). Again, figure 4.4 may shed some light on this phenomenon, specifically panel e, where high vorticity layers appear to be ejected from the surface on the upwind side of the waves.

The distribution of turbulent stress $-\langle u'w' \rangle / u_*^2$ in the airflow is on average also strongly coupled with the waves. In all three experiments presented here, the turbulent stress is negative (upward) along the upwind face of the waves, and positive over the lee. Figure 4.7.e suggests that the turbulent stresses predominantly act above the critical layer, at least in the case of young waves. Overall, these results support predictions by Belcher et al. (1993) that the turbulent stresses systematically accelerate the flow (upward stress) before the crest, and decelerate it (downward stress) past the crest. Over the older mechanical waves (figure 4.7f) however, the positive stress region doesn't remain confined to the lee side of the waves, but rather extends to the upwind face of

the waves (up to $\phi \sim -2\pi/3$) and away from the surface, which can be related to the boundary layer thickening (flow deceleration) observed above (and slightly upstream of) crests in figure 4.5c.

The line plots in figure 4.7 (panels g, h and i) show that the turbulent momentum flux rapidly represents over 100% of the total flux as close to the surface as $k_p z = 0.1$, over the youngest and oldest waves. This points once again to the symmetry between dynamics completely above the critical layer for very young waves, and dynamics below for very old waves. The middle-aged wind waves however ($C_p/u_* = 6.5$), show very little turbulence within the critical layer, and the mean turbulent momentum flux doesn't reach the level of the total flux until $k_p z = 0.6$ (not shown here).

A quadrant analysis of the turbulent momentum fluxes is presented in figure 4.8, where we have plotted our laboratory results along-side results reported in Sullivan et al. (2008). Quadrant analysis was first introduced by Wallace et al. (1972); Willmarth and Lu (1972) as a method to understand and quantify turbulent stress producing motions in solid-wall-bounded turbulent boundary layers. Later, the method was applied to the turbulent flux measurements within the marine atmospheric boundary layer (Chambers and Antonia, 1981; Smedman et al., 1999; Sullivan et al., 2008). Briefly, the ratio $Q_r = -(Q2+Q4)/(Q1+Q3)$ represents the importance of downward ($Q2 + Q4 = \overline{u'w'}$, with u' and w' of opposite signs) versus upward ($Q1 + Q3 = \overline{u'w'}$, with u' and w' of same sign)) turbulent momentum flux events. Ejections (Q2) and sweeps (Q4), such as those directly observed in figure 4.1, are considered to be the principal mechanism for downward momentum flux events in turbulent boundary layers. Our results, which were achieved for 10-m wave ages C_p/U_{10} ranging from 0.07 to 2.15, fall well within the results from LES calculations (Sullivan et al., 2008), CBLAST (Edson et al., 2007), and field measurements from Smedman et al. (1999). Our measurements of turbulent fluxes were taken between $z = 1$ cm and $z = 4$ cm. The downward turbulent flux events are in general twice as important as upward events, which appears to be the norm for waves near the wind-wave equilibrium ($C_p/U_{10} = 1.2$, see Alves et al., 2003) such as ours.

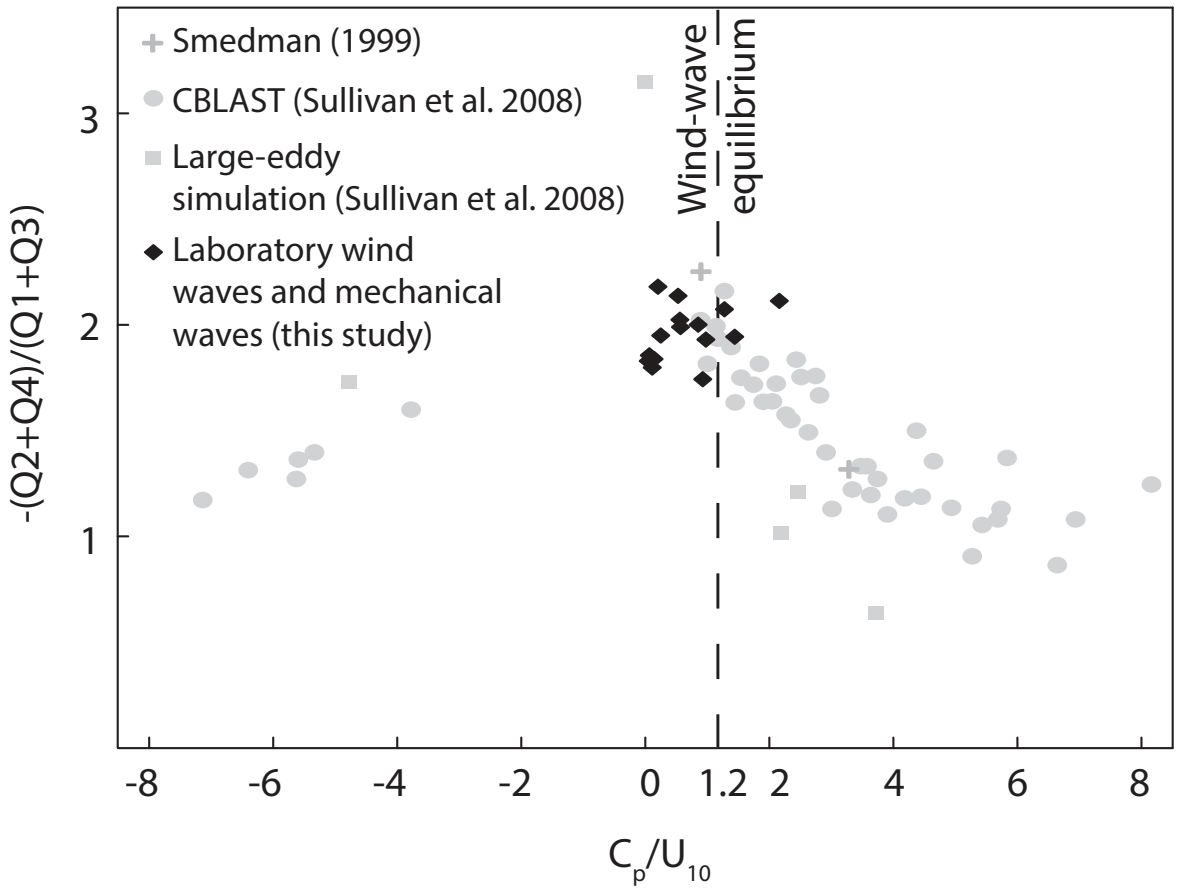

Figure 4.8: Quadrant analysis of turbulent momentum flux events, as a function of wave age. The ratio $-(Q2+Q4)/(Q1+Q3)$ represents the importance of downward ($Q2+Q4=\overline{u'w'}$, with u' and w' of opposite signs) versus upward ($Q1+Q3=\overline{u'w'}$, with u' and w' of same sign) turbulent momentum flux events. Additional data, extracted from Sullivan et al. (2008), are provided for comparison with our laboratory results.

4.6 Summary and Conclusions

We were able to obtain high resolution two-dimensional velocity measurements in the airflow above waves, in a wide range of wind/wave conditions, in controlled laboratory conditions. We found a strong wave phase dependence of all quantities, as well as a drastic dependence on the wave age. Very young waves ($C_p/u_* \sim 2$) were found to have very thin critical layers, with on average a large sheltering effect (or streamline asymmetry) past the crest, where turbulence and turbulent shear stress are very large compared with the surrounding fluid. The thickness of the critical layer, where the wave surface orbitals are strongly interacting with the airflow, increases with increasing wave age. Even for relatively young wind waves ($C_p/u_* = 6.5$), the mean airflow near the surface starts to display a reversed asymmetry (or "negative asymmetry", Belcher and Hunt, 1998) with respect to the airflow above the critical height. This may point to the importance on average of a critical layer mechanism (Miles, 1957) for the growth of wind waves, in spite of the turbulent nature of the airflow, and in spite of the numerous turbulent ejections of high vorticity structures that leave the surface and cross the critical layer. In fact, turbulence in the airflow is on average dramatically reduced below the critical height. Above the critical height, the phase distribution of the turbulence is also asymmetrical (sheltering) which is rather favorable toward wave growth. In this sense, both the mean flow and the turbulence appear to work in concert on wave growth. The question of the reduction of turbulent stress by waves, and replacement by wave-induced stress is not obvious, and will require a thorough study of the momentum balance throughout the air above the waves, which involves careful projections of the different quantities and appropriate coordinate transformation (Hara and Sullivan, 2015). This will be the object of a future study (see appendix A). The intermittent occurrence of airflow separation past young wave crests dramatically increases the average intensity of the turbulence past crests, produced by detached very high free shear layers. Questions remain as to the coupling of these events with the motions in the water below, and specifically whether wave breaking is the only condition for the separation of turbulent boundary layers

over waves. Simultaneous air-water measurements, using similar high resolution two-dimensional techniques as those presented here, would shed some light on this debate. Finally, above fast (old) waves, the sheltering effect is reversed, and surface orbital velocities appear to control and drive the entire air-side boundary layer. A quadrant analysis of the turbulent stresses around $\zeta \sim 3$ cm shows trends of predominantly downward momentum flux versus upward (by a factor of 2), in all our wind-wave conditions, which is in agreement with CBLAST field measurements and LES results (Sullivan et al., 2008).

Chapter 5

CONCLUSIONS

5.1 Summary and Conclusions

Using a novel complex imaging system, we were able to measure high resolution two-dimensional velocity fields in the airflow above waves, in a wide range of wind/wave conditions, in the laboratory. The system uses a combination of particle image velocimetry and laser-induced fluorescence techniques. Our laboratory measurements were achieved as close as 100 μm to the air-water interface, and have yielded important results on the structure of the airflow above waves.

5.1.1 Instantaneous structure of the turbulent airflow above waves

We were able to directly observe coherent turbulent structures in the airflow above waves, such as turbulent ejections and sweeps, and detachment from the surface of high spanwise vorticity layers. These events take place, starting at very low wind speeds ($U_{10} = 2.19$ m s^{-1}), when no waves are detected. When waves are present at the air-water interface, their form factor creates alternatively favorable and adverse pressure gradient conditions and their surface orbital motions influence the airflow near the surface. In particular, high vorticity layers are ejected from the crests of wind waves starting at low wind speeds ($U_{10} = 2.19$ m s^{-1}). Since ejections and sweeps are important contributors to the total turbulent energy present in the turbulent boundary layer (Robinson, 1991), their presence above waves may impact the marine atmospheric boundary layer as a whole. Furthermore, their strong coupling with the wavy surface influences the distribution of air-sea momentum flux. Similar structures have only been directly in turbulent boundary layers over solid walls up to now (Meinhart and Adrian, 1995; Adrian, 2007).

We identified airflow separation events over wind waves, using detailed analysis of two-dimensional instantaneous spanwise vorticity fields within the first 500 μm above the water surface. Separation events start at low to moderate wind speeds. Airflow separation may lead to negative spanwise vorticity, and upward surface tangential stresses past the crest of the waves. Such events take place past nearly 20% of wind waves when $U_{10} = 5.00$ m s^{-1}, at a fetch of 22.7 m. At high wind speeds ($U_{10} = 16.63$ m s^{-1}), nearly 90% of the wind-generated waves induce airflow separation.

We directly observed that at low to moderate wind speeds, even when airflow separation occurs past wave crests, the airflow viscous sublayer is intact on the upwind face of waves. This points to the fact that at these wind speeds, the airflow may be on average smooth upwind of crests, and rough downwind of crests. At higher wind speeds, we noted that the surface roughness elements protrude outside the viscous sublayer, on the upwind face of waves, which is an indicator of aerodynamically rough airflow conditions.

5.1.2 Structure of the mean airflow and fluxes

We were also able to estimate the statistical significance of the observed instantaneous structures, and understand the impacts of their coupling with the wave field, by performing wave-phase sensitive averaging. This was made possible by combining our air-side velocity data with local and surrounding spatial and temporal wave measurements. Robust phase-sensitive averaging of two-dimensional motions and fluxes in the airflow, on average from exactly 100 μm to approximately 8 cm above the instantaneous water surface, was achieved. Using the large streamwise spatial wave profiles provided by the imaging system, it was possible to perform this averaging not only over monochromatic mechanical waves, but also over wind waves, in an orthogonal surface-following frame of reference. To the best of our knowledge, this is the first time that this has been achieved over wind waves.

We find that mean and turbulent quantities are on average strongly phase-locked. The structure of the airflow motions, momentum fluxes, and turbulence production regions, are also very dependent on wave age.

Over very young wind waves ($C_p/u_* \sim 2$) the critical layer is thin. A strong sheltering effect takes place past wave crests. The sheltering is sometimes non-separated, downwind wave faces are then populated with numerous turbulent sweeps and ejections. Airflow separation can also occur frequently past young wind waves; intense turbulence is then generated in the airflow past wave crests. The mean turbulent momentum fluxes and turbulent kinetic energy production are dramatically increased past wave crests, in spite of the intermittent nature of airflow separation events. In high wind speed conditions, intense turbulence is also produced on the rough, upwind faces of waves. This effect may mitigate the relative drag increase due to flow separation.

When wind waves travel slightly faster (with respect to wind speed), the critical layer has, on average, a finite thickness, and shows strong coupling with the mean underwater wave motions. We observe this starting at relatively young wave ages ($C_p/u_* = 6.5$). In spite of numerous turbulent ejections and sweeps stemming from the water surface and frequently crossing the critical height, turbulence is dramatically decreased within the critical layer of wind waves at that wave age ($C_p/u_* = 6.5$). Below the critical layer, mean wave-coherent fluxes indicate that mean wave motions can induce motions in the MABL.

Old (fast with respect to the wind) waves ($C_p/u_* > 30$) show intense forcing of the airflow by the underwater orbital motions and momentum fluxes. In these conditions, we observed signs of a reversed sheltering effect above the average wave.

5.2 Future Work

5.2.1 Wind-wave coupling and wind-wave generation

Questions remain as to the coupling of the airflow structure with the motion in the water below. In this study, using linear wave theory, we began to estimate the coupling mechanisms between water and air motions. However the kinematics of

strongly wind-forced waves are very non-linear, especially when dissipative mechanisms take place, such as parasitic capillary waves or white-capping. These mechanisms are believed to have a large impact on the airflow and on the wind stress as a whole. Simultaneous air-water measurements, using similar high resolution two-dimensional techniques as those presented here, would shed some light on this debate.

5.2.2 Field measurements

We report the successful achievement of two-dimensional high resolution near-surface (as close as 0.3 mm) measurements in the airflow above waves in the field, which have begun to point toward a validation of the laboratory results. Observations of instantaneous two-dimensional vorticity fields, directly measured in the airflow above waves in the field, suggest that, like in the laboratory, the downwind side of wave crests is populated by numerous turbulence-producing dynamics. Further analysis of our results is needed to better quantify this. Details are provided in appendix B. We anticipate to observe a combination of young wave airflow dynamics above the strongly wind-forced components of the wave spectrum, and old wave mechanisms in the mean airflow correlated with longer swell components. It should be noted that the problem in the field is further complicated by the three-dimensionality of the wave field, non-alignment of wind and waves, wind gustiness.

In addition, detailed field measurements in high to extremely high wind speeds are lacking, largely because of the important technical challenges involved in acquiring small scale high resolution data in stormy conditions, near the highly dynamic air-sea interface. Even laboratory measurements of the detailed airflow structure in extremely high wind speeds are still lacking. Such measurements are essential, in order to improve hurricane intensity forecasts. The complexity and challenging nature of the measurements required for this, will require the use of fixed, minimally intrusive research platforms, in regions of high wind speed conditions.

BIBLIOGRAPHY

Adrian, R. J. (2007). Hairpin vortex organization in wall turbulence. *Phys. Fluids*, 19(4):041301.

Alves, J. H. G., Banner, M. L., and Young, I. R. (2003). Revisiting the pierson-moskowitz asymptotic limits for fully developed wind waves. *J. Phys. Oceanogr.*, 33(7):1301–1323.

Anderson, D., Tannehill, J., and Pletcher, R. (1984). *Computational fluid mechanics and heat transfer*. Hemisphere Publishing, New York, NY.

Aris, R. (1962). *Vectors, tensors and the basic equations of fluid mechanics*. Englewood Cliffs: Prentice-Hall.

Babanin, A. V., Banner, M. L., Young, I. R., and Donelan, M. A. (2007). Wave-follower field measurements of the wind-input spectral function. part iii: Parameterization of the wind-input enhancement due to wave breaking. *Journal of Physical Oceanography*, 37(11):2764–2775.

Banner, M. L. (1990). The influence of wave breaking on the surface pressure distribution in wind-wave interactions. *Journal of Fluid Mechanics*, 211:463–495.

Banner, M. L. and Melville, W. K. (1976). On the separation of air flow over water waves. *J. Fluid Mech.*, 77:825–842.

Banner, M. L. and Peirson, W. L. (1998). Tangential stress beneath wind-driven air-water interfaces. *J. Fluid Mech.*, 364:115–145.

Barnett, T. and Kenyon, K. (1975). Recent advances in the study of wind waves. *Reports on Progress in Physics*, 38(6):667.

Baskaran, V., Smits, A. J., and Joubert, P. N. (1987). A turbulent flow over a curved hill part 1. growth of an internal boundary layer. *Journal of Fluid Mechanics*, 182:47–83.

Batchelor, G. and Proudman, I. (1954). The effect of rapid distortion of a fluid in turbulent motion. *The Quarterly Journal of Mechanics and Applied Mathematics*, 7(1):83–103.

Belcher, S. E. and Hunt, J. C. R. (1998). Turbulent flow over hills and waves. *Annu. Rev. Fluid Mech.*, 30:507–538.

Belcher, S. E., Newley, T. M. J., and Hunt, J. C. R. (1993). The drag on an undulating surface induced by the flow of a turbulent boundary layer. *J. Fluid Mech.*, 249:557–596.

Belden, J. and Techet, A. H. (2011). Simultaneous quantitative flow measurement using piv on both sides of the air-water interface for breaking waves. *Experiments in Fluids*, 50(1):149–161.

Bell, M. M., Montgomery, M. T., and Emanuel, K. A. (2012). Air–sea enthalpy and momentum exchange at major hurricane wind speeds observed during cblast. *J. Atmos. Sci.*, 69(11):3197–3222.

Benjamin, T. B. (1959). Shearing flow over a wavy boundary. *J. Fluid Mech.*, 6(02):161–205.

Bliven, L., Huang, N., and Long, S. (1986). Experimental study of the influence of wind on benjamin-feir sideband instability. *J. Fluid Mech.*, 162:237–260.

Bretschneider, C. L. (1965). Generation of waves by wind. state of the art. Technical report, DTIC Document.

Breuer, M., Peller, N., Rapp, C., and Manhart, M. (2009). Flow over periodic hills-numerical and experimental study in a wide range of reynolds numbers. *Computers & Fluids*, 38(2):433–457.

Calhoun, R. J. and Street, R. L. (2001). Turbulent flow over a wavy surface: Neutral case. *Journal of Geophysical Research: Oceans (1978-2012)*, 106(C5):9277–9293.

Chalikov, D. V. (1978). The numerical simulation of wind-wave interaction. *J. Fluid Mech.*, 87:561–582.

Chambers, A. J. and Antonia, R. A. (1981). Wave-induced effect on the reynolds shear stress and heat flux in the marine surface layer. *J. Phys. Oceanogr.*, 11(1):116–121.

Chang, P. C., Plate, E. J., and Hidy, G. M. (1971). Turbulent air flow over the dominant component of wind-generated water waves. *J. Fluid Mech.*, 47(01):183–208.

Craik, A. D. (2004). The origins of water wave theory. *Annu. Rev. Fluid Mech.*, 36:1–28.

Crapper, G. (1957). An exact solution for progressive capillary waves of arbitrary amplitude. *Journal of Fluid Mechanics*, 2(06):532–540.

Csanady, G. T. (2001). *Air-sea interaction: laws and mechanisms*. Cambridge University Press.

Donelan, M. (1990). Air-sea interaction. *The sea*, 9(Part A):239–292.

Donelan, M., Haus, B., Reul, N., Plant, W., Stiassnie, M., Graber, H., Brown, O., and Saltzman, E. (2004). On the limiting aerodynamic roughness of the ocean in very strong winds. *Geophys. Res. Lett.*, 31(18).

Donelan, M. A., Babanin, A. V., Young, I. R., and Banner, M. L. (2006). Wave-follower field measurements of the wind-input spectral function. part ii: Parameterization of the wind input. *J. Phys. Oceanogr.*, 36(8):1672–1689.

Donelan, M. A., Babanin, A. V., Young, I. R., Banner, M. L., and McCormick, C. (2005). Wave-follower field measurements of the wind-input spectral function. part i: Measurements and calibrations. *Journal of Atmospheric and Oceanic Technology*, 22(7):799–813.

Duncan, J., Qiao, H., Philomin, V., and Wenz, A. (1999). Gentle spilling breakers: crest profile evolution. *J. Fluid Mech.*, 379:191–222.

Edson, J., Crawford, T., Crescenti, J., Farrar, T., Frew, N., Gerbi, G., Helmis, C., Hristov, T., Khelif, D., Jessup, A., et al. (2007). The coupled boundary layers and air-sea transfer experiment in low winds. *Bull. Amer. Meteor. Soc.*

Edson, J., Fairall, C., Bariteau, L., Zappa, C., Cifuentes-Lorenzen, A., McGillis, W., Pezoa, S., Hare, J., and Helmig, D. (2011). Direct covariance measurement of co2 gas transfer velocity during the 2008 southern ocean gas exchange experiment: Wind speed dependency. *Journal of Geophysical Research: Oceans (1978-2012)*, 116(C4).

Edson, J. B., Jampana, V., Weller, R. A., Bigorre, S. P., Plueddemann, A. J., Fairall, C. W., Miller, S. D., Mahrt, L., Vickers, D., and Hersbach, H. (2013). On the exchange of momentum over the open ocean. *J. Phys. Oceanogr.*, 43(8):1589–1610.

Friedlingstein, P., Andrew, R., Rogelj, J., Peters, G., Canadell, J., Knutti, R., Luderer, G., Raupach, M., Schaeffer, M., van Vuuren, D., et al. (2014). Persistent growth of CO2 emissions and implications for reaching climate targets. *Nature geoscience*, 7(10):709–715.

Gent, P. and Taylor, P. (1976). A numerical model of the air flow above water waves. *J. Fluid Mech.*, 77(01):105–128.

Gent, P. R. and Taylor, P. A. (1977). A note on separation over short wind waves. *Bound. -Layer Meteor.*, 11:65–87.

Grachev, A. and Fairall, C. (2001). Upward momentum transfer in the marine boundary layer. *J. Phys. Oceanogr.*, 31(7):1698–1711.

Grachev, A., Fairall, C., Hare, J., Edson, J., and Miller, S. (2003). Wind stress vector over ocean waves. *J. Phys. Oceanogr.*, 33(11):2408–2429.

Grare, L. (2009). *Etude des interactions Océan-Atmosphère à proximité immédiate de l'interface: Application aux vagues de vent et aux vagues extrêmes.* PhD thesis, University of Aix-Marseille.

Grare, L., Lenain, L., and Melville, W. K. (2013a). Wave-coherent airflow and critical layers over ocean waves. *J. Phys. Oceanogr.*, 43(10):2156–2172.

Grare, L., Peirson, W. L., Branger, H., Walker, J. W., Giovanangeli, J.-P., and Makin, V. (2013b). Growth and dissipation of wind-forced, deep-water waves. *J. Fluid Mech.*, 722:5–50.

Hara, T. and Belcher, S. E. (2002). Wind forcing in the equilibrium range of wind-wave spectra. *J. Fluid Mech.*, 470:223–245.

Hara, T. and Sullivan, P. P. (2015). Wave boundary layer turbulence over surface waves in a strongly forced condition. *J. Phys. Oceanogr.*, 45(3):868–883.

Hasselmann, K., Barnett, T., Bouws, E., Carlson, H., Cartwright, D., Enke, K., Ewing, J., Gienapp, H., Hasselmann, D., Kruseman, P., et al. (1973). Measurements of wind-wave growth and swell decay during the joint north sea wave project (jonswap). Technical report, Deutches Hydrographisches Institut.

Helmholtz, H. v. (1868). Über diskontinuirliche Flüssigkeits-Bewegung. *Monatsberichte der Kniglichen Preussische Akademie der Wissenschaften zu Berlin*.

Ho, C.-M. and Huang, L.-S. (1982). Subharmonics and vortex merging in mixing layers. *J. Fluid Mech.*, 119:443–473.

Ho, C.-M. and Huerre, P. (1984). Perturbed free shear layers. *Annu. Rev. Fluid Mech.*, 16(1):365–422.

Hristov, T., Miller, S., and Friehe, C. (2003). Dynamical coupling of wind and ocean waves through wave-induced air flow. *Nature*, 422(6927):55–58.

Hsu, C.-T., Hsu, E. Y., and Street, R. L. (1981). On the structure of turbulent flow over a progressive water wave: theory and experiment in a transformed, wave-following co-ordinate system. *J. Fluid Mech.*, 105:87–117.

Hudson, J., Dykhno, L., and Hanratty, T. (1996). Turbulence production in flow over a wavy wall. *Experiments in Fluids*, 20(4):257–265.

Hussain, A. K. M. F. and Reynolds, W. C. (1970). The mechanics of an organized wave in turbulent shear flow. *J. Fluid Mech.*, 41(02):241–258.

Janssen, P. A. (1991). Quasi-linear theory of wind-wave generation applied to wave forecasting. *J. Phys. Oceanogr.*, 21(11):1631–1642.

Jeffreys, H. (1925). On the formation of water waves by wind. *Proceedings of the Royal Society of London. Series A, Containing Papers of a Mathematical and Physical Character*, pages 189–206.

Jiménez, J. (2011). Cascades in wall-bounded turbulence. *Annu. Rev. Fluid Mech.*, 44(1):27.

Jones, I. S. and Toba, Y. (2001). *Wind stress over the ocean*. Cambridge University Press.

Kahma, K. K. and Calkoen, C. J. (1992). Reconciling discrepancies in the observed growth of wind-generated waves. *J. Phys. Oceanogr.*, 22(12):1389–1405.

Kahma, K. K. and Donelan, M. A. (1988). A laboratory study of the minimum wind speed for wind wave generation. *J. Fluid Mech.*, 192:339–364.

Kawai, S. (1981). Visualization of airflow separation over wind-wave crests under moderate wind. *Bound. -Layer Meteor.*, 21:93–104.

Kawai, S. (1982). Structure of air flow separation over wind wave crests. *Boundary-Layer Meteorology*, 23(4):503–521.

Kawamura, H., Okuda, K., Kawai, S., and Toba, Y. (1981). Structure of turbulent boundary layer over wind waves in a wind wave tunnel. *The science reports of the Tohoku University. Fifth series, Tohoku geophysical journal*, 28(2):69–86.

Kawamura, H. and Toba, Y. (1988). Ordered motion in the turbulent boundary layer over wind waves. *J. Fluid Mech.*, 197:105–135.

Kelvin, L. (1871). Xlvi. hydrokinetic solutions and observations. *The London, Edinburgh, and Dublin Philosophical Magazine and Journal of Science*, 42(281):362–377.

Kendall, J. M. (1970). The turbulent boundary layer over a wall with progressive surface waves. *J. Fluid Mech.*, 41(02):259–281.

Khandekar, M. L. (1989). *Operational analysis and prediction of ocean wind waves*, volume 33. Springer Science & Business Media.

Kihara, N., Hanazaki, H., Mizuya, T., and Ueda, H. (2007). Relationship between airflow at the critical height and momentum transfer to the traveling waves. *Phys. Fluids*, 19(1):015102.

Kim, H., Kline, S., and Reynolds, W. (1971). The production of turbulence near a smooth wall in a turbulent boundary layer. *J. Fluid Mech.*, 50(01):133–160.

Kim, J., Moin, P., and Moser, R. (1987). Turbulence statistics in fully developed channel flow at low reynolds number. *J. Fluid Mech.*, 177:133–166.

Kitaigorodskii, S. and Donelan, M. (1984). Wind-wave effects on gas transfer. In *Gas transfer at water surfaces*, pages 147–170. Springer.

Kline, S., Reynolds, W., Schraub, F., and Runstadler, P. (1967). The structure of turbulent boundary layers. *J. Fluid Mech.*, 30(04):741–773.

Kovasznay, L. S. (1970). The turbulent boundary layer. *Annu. Rev. Fluid Mech.*, 2(1):95–112.

Kukulka, T. and Hara, T. (2008a). The effect of breaking waves on a coupled model of wind and ocean surface waves. part ii: Growing seas. *J. Phys. Oceanogr.*, 38(10):2164–2184.

Kukulka, T. and Hara, T. (2008b). The effect of breaking waves on a coupled model of wind and ocean surface waves. part ii: Growing seas. *J. Phys. Oceanogr.*, 38(10):2164–2184.

Kundu, P. and Cohen, I. (2010). *Fluid Mechanics*. Elsevier Science.

Lamb, H. (1932). *Hydrodynamics*. Cambridge university press.

Lewis, E. R., Wiscombe, W. J., Albrecht, B. A., Bland, G. L., Flagg, C. N., Klein, S. A., Kollias, P., Mace, G., Reynolds, R., Schwartz, S., et al. (2012). Magic: Marine arm gpci investigation of clouds. *Environmental Sciences, DOE/SC-ARM-12-020, http://www. osti. gov/scitech/servlets/purl/1052589 (last access: 1 April 2014)*.

Lin, M.-Y., Moeng, C.-H., Tsai, W.-T., Sullivan, P. P., and Belcher, S. E. (2008). Direct numerical simulation of wind-wave generation processes. *Journal of Fluid Mechanics*, 616:1–30.

Longuet-Higgins, M. S. (1969). Action of a variable stress at the surface of water waves. *Phys. Fluids*, 12(4):737–740.

Makin, V., Kudryavtsev, V., and Mastenbroek, C. (1995). Drag of the sea surface. *Bound. -Layer Meteor.*, 73(1-2):159–182.

Mastenbroek, C., Makin, V., Garat, M., and Giovanangeli, J.-P. (1996). Experimental evidence of the rapid distortion of turbulence in the air flow over water waves. *J. Fluid Mech.*, 318:273–302.

McCroskey, W. (1982). Unsteady airfoils. *Annu. Rev. Fluid Mech.*, 14(1):285–311.

Meinhart, C. D. and Adrian, R. J. (1995). On the existence of uniform momentum zones in a turbulent boundary layer. *Phys. Fluids*, 7(4):694–696.

Melville, W. (1977). Wind stress and roughness length over breaking waves. *J. Phys. Oceanogr.*, 7(5):702–710.

Melville, W. K. (1983). Wave modulation and breakdown. *J. Fluid Mech.*, 128:489–506.

Melville, W. K. and Fedorov, A. V. (2015). The equilibrium dynamics and statistics of gravity–capillary waves. *J. Fluid Mech.*, 767:449–466.

Miles, J. (1993). Surface-wave generation revisited. *J. Fluid Mech.*, 256:427–441.

Miles, J. W. (1957). On the generation of surface waves by shear flows. *J. Fluid Mech.*, 3(02):185–204.

Miles, J. W. (1962). On the generation of surface waves by shear flows. part 4. *J. Fluid Mech.*, 13(03):433–448.

Monin, A. and Obukhov, A. (1954). Osnovnye zakonomernosti turbulentnogo peremeshivanija v prizemnon sloe atmosfery (basic laws of turbulent mixing in the atmosphere near the ground). *Trudy geofiz. inst. AN SSSR*, 24(151):163–186.

Motzfeld, H. (1937). Die turbulente strömung an welligen wänden. *ZAMM-Journal of Applied Mathematics and Mechanics/Zeitschrift für Angewandte Mathematik und Mechanik*, 17(4):193–212.

Mueller, J. A. and Veron, F. (2009). Nonlinear formulation of the bulk surface stress over breaking waves: Feedback mechanisms from air-flow separation. *Bound. -Layer Meteor.*, 130(1):117–134.

Okuda, K., Kawai, S., and Toba, Y. (1977). Measurement of skin friction distribution along the surface of wind waves. *Journal of the Oceanographical Society of Japan*, 33(4):190–198.

Oppenheim, A. V. and Schafer, R. W. (2013). *Discrete-Time Signal Processing*. Pearson Education, Limited.

Paris, A. (1871). Observations on the state of the sea collected on board the dupliex and the minierva. *Revue Maritime et Coloniale*.

Phillips, O. M. (1957). On the generation of waves by turbulent wind. *J. Fluid Mech.*, 2(05):417–445.

Phillips, O. M. (1977). *Dynamics of the upper ocean*. Cambridge University Press.

Powell, M. D., Vickery, P. J., and Reinhold, T. A. (2003). Reduced drag coefficient for high wind speeds in tropical cyclones. *Nature*, 422(6929):279–283.

Raffel, M., Willert, C. E., Wereley, S. T., and Kompenhans, J. (2007). *Particle Image Velocimetry: A Practical Guide*. Springer Science & Business Media.

Rapp, R. and Melville, W. (1990). Laboratory measurements of deep-water breaking waves. *Philosophical Transactions of the Royal Society of London A: Mathematical, Physical and Engineering Sciences*, 331(1622):735–800.

Reul, N., Branger, H., and Giovanangeli, J. P. (1999). Air flow separation over unsteady breaking waves. *Phys. Fluids*, 11:1959–1961.

Robinson, S. K. (1991). Coherent motions in the turbulent boundary layer. *Annu. Rev. Fluid Mech.*, 23(1):601–639.

Russell, J. S. (1844). Report on waves. In *14th meeting of the British Association for the Advancement of Science*, volume 311, page 390.

Schlichting, H. and Gersten, K. (2000). *Boundary-Layer Theory*. Springer.

Siddiqui, K. and Loewen, M. R. (2010). Phase-averaged flow properties beneath microscale breaking waves. *Bound. -Layer Meteor.*, 134(3):499–523.

Simpson, R. L. (1989). Turbulent boundary-layer separation. *Annu. Rev. Fluid Mech.*, 21(1):205–232.

Smedman, A., Högström, U., Bergström, H., Rutgersson, A., Kahma, K. K., and Pettersson, H. (1999). A case study of air-sea interaction during swell conditions. *J. Geophys. Res.*, 104(C11):25833–25851.

Soloviev, A. V., Lukas, R., Donelan, M. A., Haus, B. K., and Ginis, I. (2014). The air-sea interface and surface stress under tropical cyclones. *Scientific reports*, 4.

Stanton, T., Marshall, D., and Houghton, R. (1932). The growth of waves on water due to the action of the wind. *Proceedings of the Royal Society of London. Series A, Containing Papers of a Mathematical and Physical Character*, pages 283–293.

Stevenson, T. (1886). *The design and construction of harbours: a treatise on maritime engineering*. A. and C. Black.

Stewart, R. H. (1970). Laboratory studies of the velocity field over deep-water waves. *J. Fluid Mech.*, 42(04):733–754.

Sullivan, P. P., Edson, J. B., Hristov, T., and McWilliams, J. C. (2008). Large-eddy simulations and observations of atmospheric marine boundary layers above nonequilibrium surface waves. *J. Atmos. Sci.*, 65(4):1225–1245.

Sullivan, P. P. and McWilliams, J. C. (2010). Dynamics of winds and currents coupled to surface waves. *Annu. Rev. Fluid Mech.*, 42:19–42.

Sullivan, P. P., McWilliams, J. C., and Moeng, C. H. (2000). Simulation of turbulent flow over idealized water waves. *J. Fluid Mech.*, 404:47–85.

Sullivan, P. P., McWilliams, J. C., and Patton, E. G. (2014). Large-eddy simulation of marine atmospheric boundary layers above a spectrum of moving waves. *J. Atmos. Sci.*, 71(11):4001–4027.

Suzuki, N., Hara, T., and Sullivan, P. P. (2014). Impact of dominant breaking waves on air–sea momentum exchange and boundary layer turbulence at high winds. *J. Phys. Oceanogr.*, 44(4):1195–1212.

Sverdrup, H. U. and Munk, W. H. (1947). Wind, sea, and swell: theory of relations for forecasting. Technical report, U.S. Hydrographic Office.

Thomas, M., Misra, S., Kambhamettu, C., and Kirby, J. (2005). A robust motion estimation algorithm for piv. *Meas. Sci. Technol.*, 16:865–877.

Ursell, F. (1956). Wave generation by wind. *Surveys in mechanics*, pages 216–249.

Veron, F. (2015). Ocean spray. *Annu. Rev. Fluid Mech.*, 47:507–538.

Veron, F., Saxena, G., and Misra, S. K. (2007). Measurements of the viscous tangential stress in the airflow above wind waves. *Geophys. Res. Lett.*, 34:1959–1961.

Wallace, J. M., Eckelmann, H., and Brodkey, R. S. (1972). The wall region in turbulent shear flow. *J. Fluid Mech.*, 54(01):39–48.

Weber, E. H. and Weber, E. F. W. (1825). Wellenlehre auf experimente gegründet. *W. Engelmann*.

Webster, P. J. and Lukas, R. (1992). TOGA COARE: The coupled ocean-atmosphere response experiment. *Bulletin of the American Meteorological Society*, 73(9):1377–1416.

Willmarth, W. and Lu, S. (1972). Structure of the reynolds stress near the wall. *J. Fluid Mech.*, 55(01):65–92.

Winant, C. D. and Browand, F. K. (1974). Vortex pairing : the mechanism of turbulent mixing-layer growth at moderate reynolds number. *J. Fluid Mech.*, 63:237–255.

Wu, J. Z., Ma, H. Y., and Zhou, M. D. (2006). *Vorticity and Vortex Dynamics*. Springer.

Yang, D., Meneveau, C., and Shen, L. (2013). Dynamic modelling of sea-surface roughness for large-eddy simulation of wind over ocean wavefield. *J. Fluid Mech.*, 726:62–99.

Yang, D. and Shen, L. (2010). Direct-simulation-based study of turbulent flow over various waving boundaries. *J. Fluid Mech.*, 650:131–180.

Zhang, E., Yeh, H., Lin, Z., and Laramee, R. S. (2009). Asymmetric tensor analysis for flow visualization. *Visualization and Computer Graphics, IEEE Transactions on*, 15(1):106–122.

Zhou, J., Adrian, R. J., Balachandar, S., and Kendall, T. (1999). Mechanisms for generating coherent packets of hairpin vortices in channel flow. *J. Fluid Mech.*, 387:353–396.

Appendix A

MOMENTUM BALANCE IN THE AIRFLOW ABOVE THE WAVY AIR-WATER INTERFACE.

A.1 Introduction

In past studies, a number of theoreticians, modelers, and experimentalists have posed the question of choosing an appropriate coordinate system to study the coupling of wind with waves (e.g., Miles, 1957; Benjamin, 1959; Gent and Taylor, 1976; Chalikov, 1978; Hsu et al., 1981). While it is clear that a fixed cartesian frame of reference does not allow to model dynamics that take place within a wave height above the water surface, cartesian fluxes are still commonly estimated, especially in field measurements, where near-surface measurements are extremely challenging (e.g., Grare et al., 2013a).

In idealized conditions, when waves are monochromatic and have a finite amplitude, it is straightforward to define a surface-following coordinate system that exponentially tends toward the fixed cartesian system away from the surface (e.g., Benjamin, 1959; Sullivan et al., 2000). This decay is coherent with the decay of deep-water wave theory orbital motions. They also tend exponentially toward no motion, away from the surface. In realistic wind-wave conditions, where a wide spectrum of wave components are present everywhere, it is possible to extend this monochromatic approach to a multi-modal version. This was done for example by Chalikov (1978) and recently by Hara and Sullivan (2015). In fact, Hara and Sullivan (2015) chose to model across-surface fluxes of horizontal momentum, rather than across-surface fluxes of normal (to the surface) momentum (e.g., Gent and Taylor, 1976), or vertical fluxes of horizontal momentum (e.g., Sullivan et al., 2000). This allowed them to rigorously estimate the balance, for example between form stress, turbulent, and wave-coherent stresses up

to the water surface, using an assumption of constant wind stress. This approach is difficult to apply to measurements (field and laboratory), because it requires to know the slope of the waves, in order to project certain quantities into along-surface and surface-normal coordinates, and consider others in a cartesian projection. In addition, as pointed out by Hudson et al. (1996), different projections may influence the sign of the flux, especially very close the wavy boundary. We showed an example of this effect in figure 3.9 of chapter 3. Using our complex two-dimensional imaging system, we are able to chose any of the aforementioned approaches.

A.2 Momentum balance (theory)

The instantaneous momentum balance can be written either in cartesian coordinates

$$\frac{\partial u_i}{\partial t} + \frac{\partial}{\partial x_j}\left(p\delta_{ij} + u_i u_j - 2\nu s_{ij}\right) = 0, \tag{A.1}$$

cartesian-curvilinear coordinates (Hara and Sullivan, 2015),

$$J\frac{\partial u_i}{\partial t} + \frac{\partial}{\partial \xi_j}\left(Jp\frac{\partial \xi_j}{\partial x_i} + u_i U_j - 2\nu J S_{ij}\right) = 0, \tag{A.2}$$

or in a fully curvilinear form:

$$\frac{\partial U_i}{\partial t} + \left(g_{ij}p + U_i U_j - 2\nu\Sigma_{ij}\right)_{,j} = 0, \tag{A.3}$$

The following notations are used in the above 3 equations:

$(u_1, u_3) = (u, w)$ and $(U_1, W_3) = (U, W)$

s_{ij} is the cartesian strain rate tensor as defined by

$$s_{ij} = \frac{1}{2}\left(\frac{\partial u_i}{\partial x_j} + \frac{\partial u_j}{\partial x_i}\right).$$

S_{ij} is the cartesian-curvilinear strain rate tensor

$$S_{ij} = \frac{1}{2}\left(g_{ik}\frac{\partial u_j}{\partial \xi_k} + g_{jk}\frac{\partial u_i}{\partial x_k}\right),$$

and g_{ij} the metric tensor

$$g_{ij} = \frac{\partial x_k}{\partial \xi_i}\frac{\partial x_k}{\partial \xi_j},$$

where Σ_{ij} is the fully curvilinear strain rate tensor as defined by

$$\Sigma_{ij} = \frac{1}{2}\left(g^{ik}U_{j,k} + g^{jk}U_{i,k}\right).$$

The comma in (A.3) denotes covariant differentation, following

$$A_{i,j} = \frac{\partial A_i}{\partial \xi_j} + \Gamma^i_{kj}A_k,$$

and Γ^i_{kj} are the Christoffel symbols of second kind (e.g., Aris, 1962):

$$\Gamma^i_{kj} = \frac{1}{2}g_{ip}\left(\frac{\partial g_{pk}}{\partial \xi_j} + \frac{\partial g_{pj}}{\partial \xi_k} - \frac{\partial g_{kj}}{\partial \xi_p}\right).$$

Finally, J is the Jacobian of the transformation, which in this study can be expressed as:

$$J = \frac{\partial x}{\partial \xi}\frac{\partial z}{\partial \zeta} - \frac{\partial x}{\partial \zeta}\frac{\partial z}{\partial \xi} = 1 - 2\sum_n a_n k_n e^{i(k_n\xi+\phi_n)}e^{-k_n\zeta}.$$

It may be noted here that (A.2) results from a chain differentiation of (A.1) (Anderson et al., 1984).

Using the triple decomposition defined above, and time averaging these equations leads to:

Cartesian:

$$\frac{\partial}{\partial z}\left(\overline{\widetilde{u}_i\widetilde{w}} + \overline{u_i'w'} + \overline{p}\delta_{i3} - 2\nu\overline{s_{i3}}\right) = 0 \tag{A.4}$$

Cartesian-curvilinear:

$$\frac{\partial}{\partial \zeta}\left(\overline{\widetilde{u}_i\widetilde{W}} + \overline{u_i'W'} + \overline{\frac{1}{J}p\frac{\partial \zeta}{\partial x_i}} - 2\nu\overline{S_{i3}}\right) = 0 \tag{A.5}$$

Curvilinear:

$$\left(\overline{\widetilde{U}_i\widetilde{W}} + \overline{U_i'W'} + \overline{p}\delta_{i3} - 2\nu\overline{\Sigma_{i3}}\right)_{,3} = 0 \tag{A.6}$$

Note now that the pressure terms disappear in the pure cartesian (respectively pure curvilinear) cases when $i = 1$, i.e., in the horizontal (respectively along-surface) projection of the momentum balance.

From equation A.5, the balance of across-surface fluxes of horizontal momentum (cartesian-curvilinear approach) can now be written as:

$$\overline{-\widetilde{u}\widetilde{W}} - \overline{u'W'} - \overline{\frac{1}{J}p\frac{\partial \zeta}{\partial x}} + \nu\left(\frac{\partial \overline{u}}{\partial \zeta} + \frac{\partial \overline{w}}{\partial \xi}\right) = u_*^2 \tag{A.7}$$

A.3 Results

Normalizing equation A.7 by the total kinematic stress u_*^2 yields the following balance:

$$1 = \underbrace{\overline{-\widetilde{u}\widetilde{W}}/u_*^2}_{W}\underbrace{-\overline{u'W'}/u_*^2}_{T}\underbrace{-\overline{\frac{1}{J}p\frac{\partial \zeta}{\partial x}}/u_*^2}_{P}\underbrace{+\nu\left(\frac{\partial \overline{u}}{\partial \zeta} + \frac{\partial \overline{w}}{\partial \xi}\right)/u_*^2}_{V} \tag{A.8}$$

In figure A.1, we show the momentum flux terms from equation A.8, computed from our PIV measurements in the airflow, during one of our wind wave experiments (U_{10} = 14.34 m s^{-1}). The waves during this experiment were young (C_p/u_* = 1.6). This wave age is very close to the conditions used by Hara and Sullivan (2015) in their LES results. They used a wave age of C_p/u_* = 1.58. Hara and Sullivan (2015) also provide a detailed development of equation A.8.

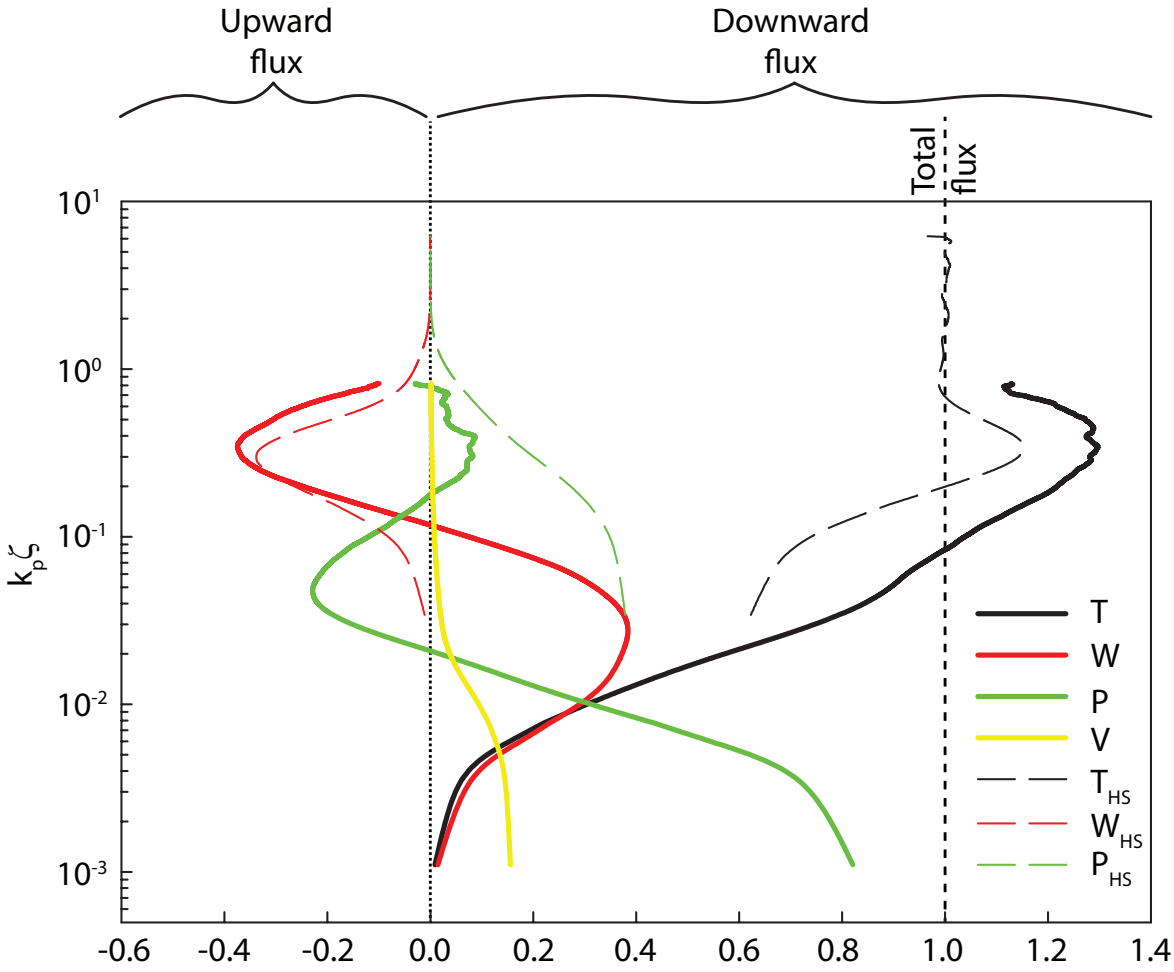

Figure A.1: Mean momentum fluxes, in the "cartesian-curvilinear" momentum balance approach, for wind waves at a fetch of 22.7 m, with 10-m wind speed $U_{10} = 14.34$ m s^{-1}, and wave age $C_p/u_* = 1.6$. Turbulent (T), wave-coherent (W), and viscous (V) were directly obtained from our velocity measurements. The pressure-slope correlation term P is deduced, using the constant stress assumption (equation A.8). T_{HS}, W_{HS}, and P_{HS} are large eddy simulation (LES) results from Hara and Sullivan (2015), for wind waves with a similar wave age of $C_p/u_* = 1.58$.

First, we observe that the turbulent flux T shoots past the total flux near $k_p\zeta = 0.08$. T reaches a maximum around $k_p\zeta = 0.34$, and begins to converge toward 1 farther away from the surface. This result is in broad agreement with the LES results from Hara and Sullivan (2015). In fact, their point of maximum turbulent stress is the same as ours. Near the surface, T drops to nearly zero, where the mean viscous stresses contribute to 0.16% of the total stress. In these steep wave conditions ($a_{rms}k_p = 0.26$), such a small contribution of viscous stresses is not surprising. This was also observed for example by Banner and Peirson (1998), who suggested that the remaining contributor to stress at the surface is the form drag, or pressure-slope term. Here we estimate the form stress P throughout the sampled air-column, by deducing it from equation A.8, where all other terms are measured by PIV. Our results show that pressure is a large contributor to the total stress at the surface of these young strongly forced waves: at the surface, we note that $P > 0.8$. Away from the surface, our estimate of P drops dramatically and even becomes negative when $0.02 < k_p\zeta < 0.17$. This is in contrast with the LES form stress results from Hara and Sullivan (2015), whose P_{HS} remains positive everywhere up to $k_p\zeta \sim 2.42$. Our wave-coherent stress measurements W agree broadly with W_{HS} above a height of ~ 0.12, where all estimates are negative (upward flux). Below this height, our wave stress estimates are downward ($W > 0$), whereas W_{HS} goes to zero. However, this is approximately the region where our pressure estimates also disagree (as was stated above). So it appears that it is our partitioning between pressure and wave-coherent stresses that disagree near the surface, but our estimates of their total combined effect may be coherent with those by Hara and Sullivan (2015). In fact, they suggest that both terms are physically similar, and both contribute to what they call a "wave-induced stress". We agree with this idea, especially when remembering the average boundary layer thinning and thickening that occurs along the average wave, in all wind wave experiments presented in this study (see previous chapters). It is well known that boundary layer thickness variations above hills or solid waves require (or are required by) along-wave pressure fluctuations, and wave perturbation stresses (e.g., Belcher and Hunt, 1998).

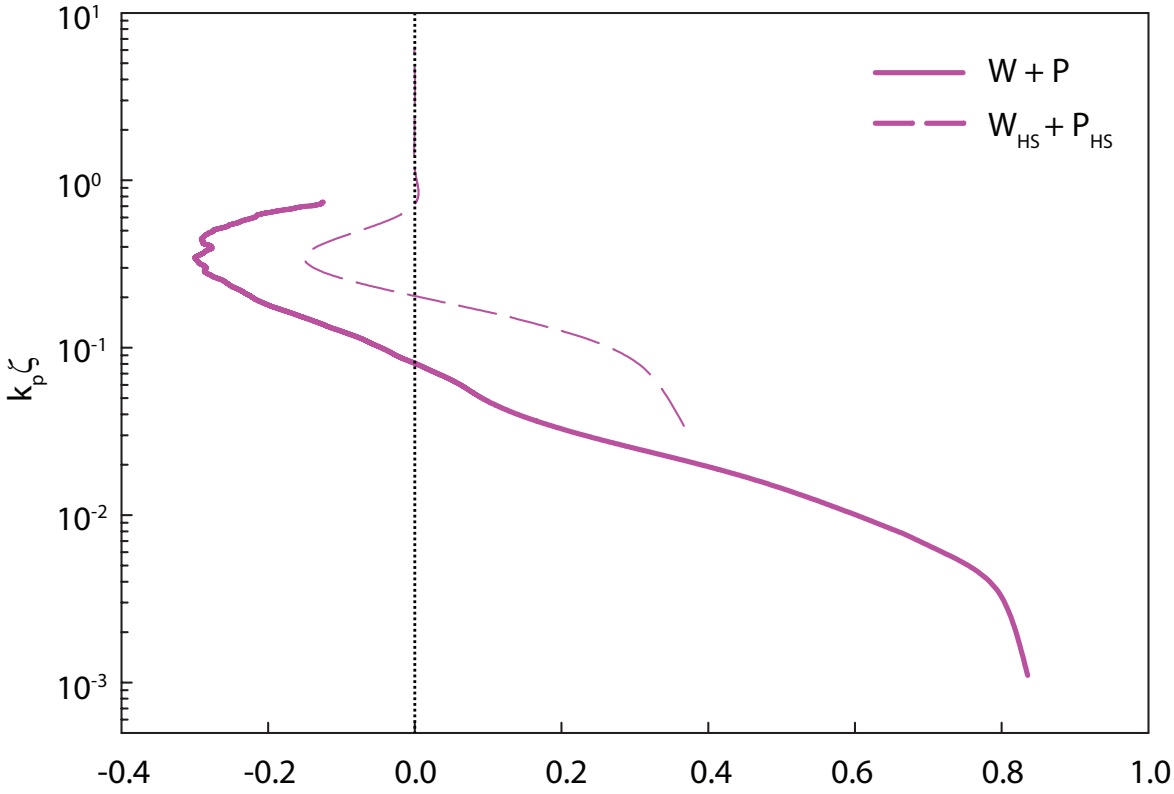

Figure A.2: Comparison of our results with the "wave-induced stress" term, from Hara and Sullivan (2015). It is the sum of pressure and wave contributions $P + W$.

In figure A.2, we compare our estimates of the "wave-induced term" $P + W$, with those of Hara and Sullivan (2015). The results are broadly coherent, with again, slightly larger (and closer to the surface) "overshoot" (in the negative) of our wave-induced term compared with theirs. Remember our turbulent term T had the same behavior: overshoot (above 1) larger and closer to the surface than T_{HS}. This could be caused simply by our slightly steeper peak wave conditions: Hara and Sullivan (2015) use $ak = 0.226$, while we have here $a_{rms}k_p = 0.26$. Overall, we find a good agreement between our experimental results and the LES results from Hara and Sullivan (2015), for similar wind-wave conditions. It should be noted that, to the best of our knowledge, our detailed measurements are the first to provide rigorous investigation of the entire momentum balance, in "cartesian-curvilinear" coordinates. This is only made possible thanks to the combination of high resolution two-dimensional velocity measurements, along with spatial and temporal wave characteristics, which allowed to project and phase average all measured quantities into any coordinate system.

Appendix B

FIELD PIV MEASUREMENTS IN THE AIRFLOW ABOVE WAVES: PRELIMINARY RESULTS

B.1 Introduction

In the laboratory, using an elaborate novel complex imaging system, we were able to obtain unique high resolution measurements of the kinematics in the airflow above a wide range of wind/wave conditions. Our observations over wind-generated waves, in local equilibrium with the wind, are exactly applicable to the field in a small number of fetch limited, steady state conditions. For example, these conditions exist close to an upwind shore, when the wind is steady and horizontally uniform, and in the absence of onshore swells (Csanady, 2001). Our observations over mechanically generated swells recreate older wave conditions, where wind and waves are aligned.

At the ocean surface, local equilibrium conditions are not the norm. This was recently pointed out for example by Hara and Sullivan (2015)). It is common for swells generated by storms far away to propagate into regions of young wind seas. The underlying swells can cause the younger wind waves to break, because swell crest surface orbital velocities can locally increase the surface drift (Phillips, 1977). In addition, swells and local winds are often not aligned (Grachev et al., 2003). Such conditions may invalidate Monin-Obukhov similarity theory (Sullivan and McWilliams, 2010). Finally, the wind forcing in the field is not always steady and homogenous; large scale turbulent motions in the MABL cause wind gusts, that abruptly change the local wind stress.

In order to check the degree of applicability of our detailed high resolution laboratory measurements to field conditions, we conducted a series of preliminary experiments in the field. Details and preliminary results are given below.

B.2 Instrument setup

A small research platform, R/P *Cheval Blanc*, was especially developed, in order to acquire PIV measurements in the airflow above waves. The foundation of the boat was a modified commercial 18-foot Hobie catamaran. The experimental setup is sketched in figure B.1. Once in position in the ocean, this structure offered a reasonably stable and minimally intrusive platform that is convenient for the study of the airflow above ocean waves, in low to moderate wind speeds. A common difficulty with air-sea momentum flux measurements from large vessels, is the large wind shadow created by the ship, which heavily disturbs the environment and the fluxes themselves. This then requires the measured data to be corrected for "ship-induced flow perturbations" (Lewis et al., 2012).

In contrast, the bow of our small platform, when oriented into the wind, offered access to relatively undisturbed wind waves and winds. The setup was as follows: An aluminum structure bolted to the port hull was built to hold a pulsed Nd-Yag PIV Laser (200 mJ/pulse, 532 nm), that generated a vertical light sheet directed toward the surface and in the dominant along wind direction. The laser head was placed inside a modified waterproof Pelican case, fitted with an acrylic window for the laser sheet to shine through. A vertical laser sheet was achieved thanks to a mirror held above the undisturbed imaging area by a tripod. A CCD camera (Pulnix RM-4200, 2048 x 2048 pixel) was placed in a waterproof housing and mounted on the starboard hull. The camera was focused onto the region of the air-water interface where the vertical laser sheet intersected with the water surface. Both laser and camera were computer-controlled, using National Instruments software and hardware. The camera lens focus and aperture were remotely controlled by computer, via a Birger Engineering lens controller. In addition, the camera lens was fitted with a high quality band-pass green filter (532 nm), in order to filter out all other wavelengths but that of the PIV laser.

Fog seeding particles were generated upwind of the imaging region, using a low pressure (and low power) misting system that was developed for this experiment.

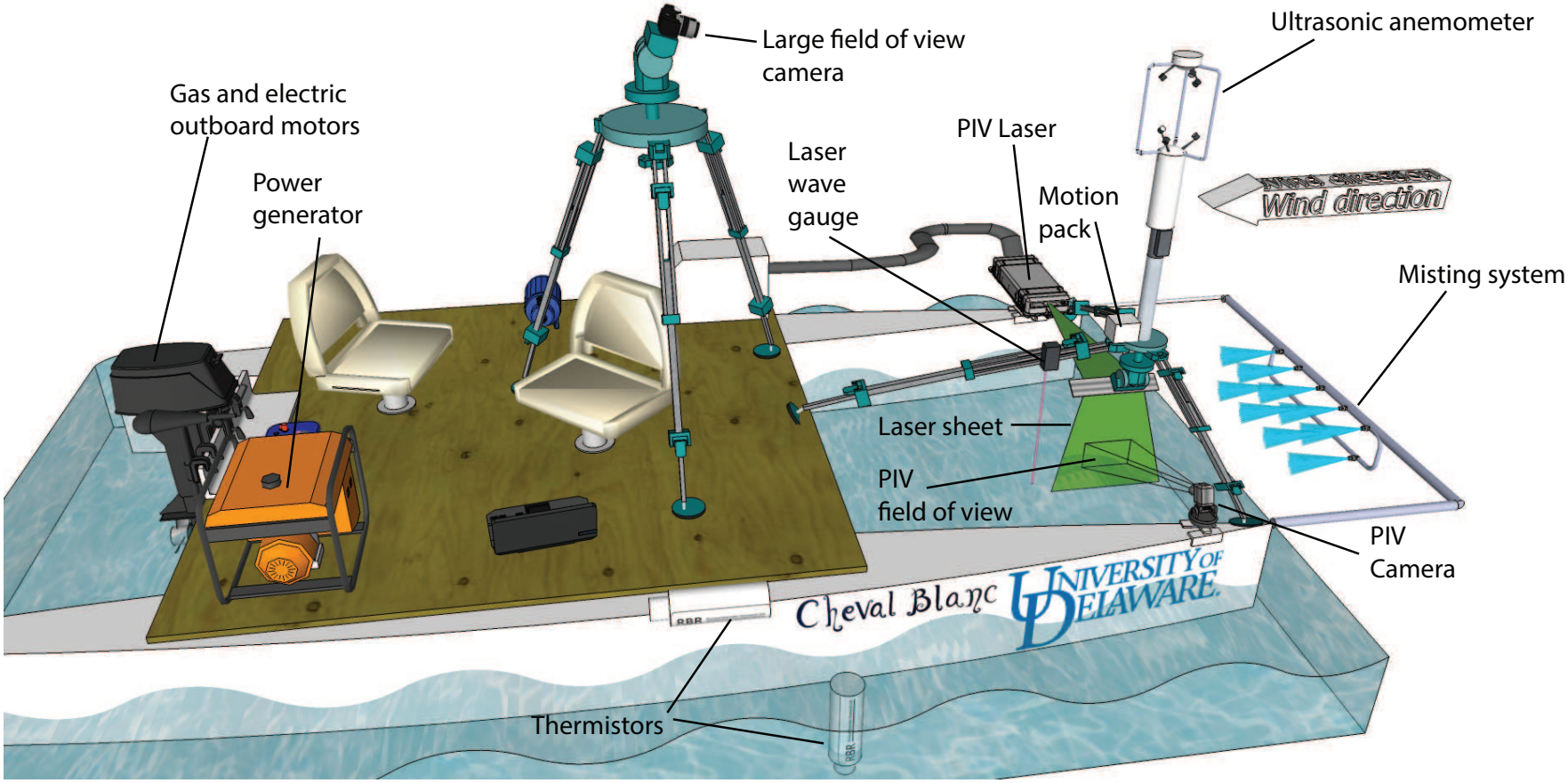

Figure B.1: Sketch of the field experimental design, mounted on the bow of the R/P *Cheval Blanc*, a research platform specifically developed for PIV measurements in the airflow above waves.

Since the misting system was situated only ∼2 m upwind of the PIV imaging section, it was important to verify the validity of our technique, in the laboratory, prior to field operation. By comparing single point ultrasonic anemometer data with PIV data, we verified in the laboratory that the fog particles had enough time and distance to be fully entrained by the undisturbed wind before entering the PIV field of view, and that the initial momentum input created by the misting did not induce additional motions and turbulence within the PIV imaging region. The choice of a low pressure misting system was crucial for these two points. In addition, it was also preferable to check that the presence of the thin misting tubes and nozzles in the airflow did not affect the turbulent fluctuations of the airflow within the imaging region. The laboratory testing was achieved by placing the fully equipped boat in the laboratory, downwind of an industrial blower. Then, a series of experiments were performed. First, PIV measurements were taken in the airflow, exactly where the imaging section was projected to be in the field (see for example the region identified as "PIV field of view" in figure B.1). Then, an ultrasonic anemometer (RM Young 81000) was positioned exactly within the PIV field of view. Anemometer measurements were taken with and without fog. Finally, the boat was removed, and the anemometer left in place, to acquire additional measurements, without fog and without the boat. Good agreement between all techniques was found for the mean turbulent fluctuations and fluxes, when comparing respectively all anemometer experiments with one another, and anemometer with PIV measurements.

Along with the basic PIV system, several other instruments were deployed to monitor the peripheral conditions of the experiment. A laser altimeter (Reinshaw, ILM HR) used as a wave gauge, took single point time series of the wave height in the vicinity of the imaging region. In addition, a six degree of freedom motion package (Xsense) was fastened to the mirror-holding tripod, in order to allow all acquired data to be corrected for the yaw, pitch and roll of the boat. An ultrasonic anemometer (RM Young 81000) measured the wind speed and turbulence at an altitude of 3 m above the mean water surface. Additionally, a DSLR camera (Nikon D300, 12 x 10^6 pixel), on

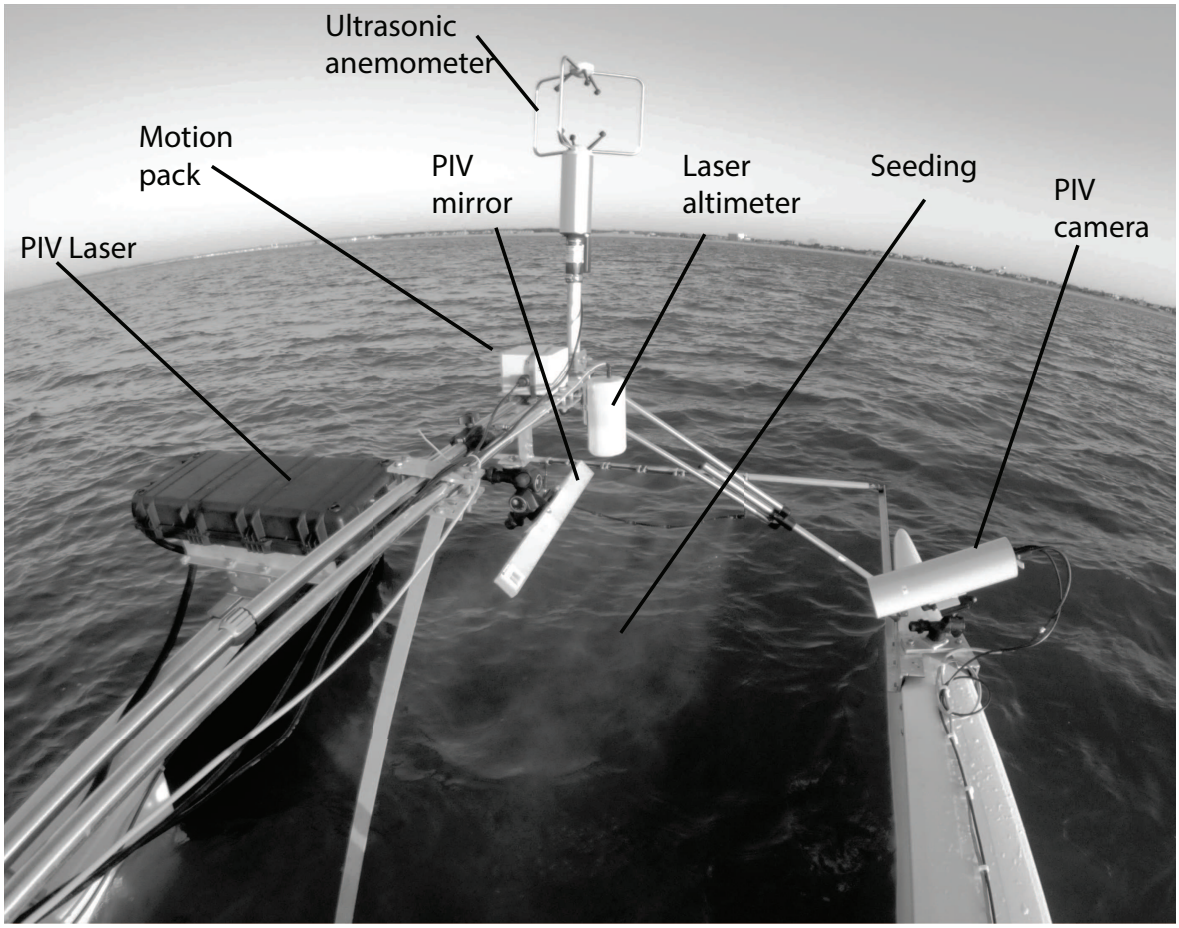

Figure B.2: Day time PIV dry run, off the bow of *Cheval Blanc*.

a tripod on the deck, fitted with an ultra-wide angle (fish eye) lens, directed upwind, acquired images of the overall wave field entering the imaging area, at a rate of 1 Hz. Finally, air- and water-side thermistors (Richard Brancker Research) were also used to monitor air and water temperatures at a rate of 1 Hz.

B.3 Field measurement procedure

At first, before sunset, the outboard motor was used to take the boat offshore in the Delaware Bay, out of any wind shadow and away from other mariners. The electric trolling motor was then used to keep the bow of the boat into the wind. Once in position, all instruments were powered up and tested. A photo of the day time testing

Figure B.3: Night time acquisition of PIV data in the incoming airflow above incoming waves, off the bow of *Cheval Blanc*.

phase is shown in figure B.2. There, we can readily see the seeding of the airflow by the fog particles. Notice also the orientation of the boat with respect to the wave fronts. The boat is kept perpendicular to the incoming waves, and aligned with the main wind speed direction. The wind speed direction, which can be qualitatively estimated by looking at the wake of the fog particles (figure B.2), was measured at all times using the 3D anemometer data.

Then, once the surrounding light conditions were dark enough for good quality PIV measurements (ideally, the PIV camera should only detect light from the pulsed PIV laser sheet), the fog was turned on, and PIV measurements were taken, for short intervals of $\sim$ 2 min. A photo of the night time data acquisition phase is shown in figure B.3. All PIV and camera pulses were sampled and time-stamped, along with all other surrounding data.

B.4 Preliminary results

In figure B.4.a, we show an example of an instantaneous raw PIV image. The illuminated fog particles are visible in the air above the wave, and we can observe on this shapshot that the seeding of the airflow is relatively uniform. This is important for successful PIV vector calculations (Raffel et al., 2007). It can also be noted that the air-water interface is easy to locate on this image, in spite of the presence of fog particles in the airflow, and the secondary laser light reflections that they may cause. This was unexpected, but it was not conceivable to take into the field a system as complex as the one deployed in the laboratory. Instead, in the field, it was probably the natural abundance of particles and dissolved organic and inorganic matter, that had a similar effect as a dye.

From the instantaneous two-dimensional PIV velocity fields, we were able to compute the instantaneous vorticity along the wave (figure B.4b). The vorticity field displays what appears to be a free high vorticity structure detached from the surface between the crest and $x = 0.12$ m, an attached high vorticity region around $x = 0.15$ m, and downwind of the crest, several detached high vorticity layer-like structures. This

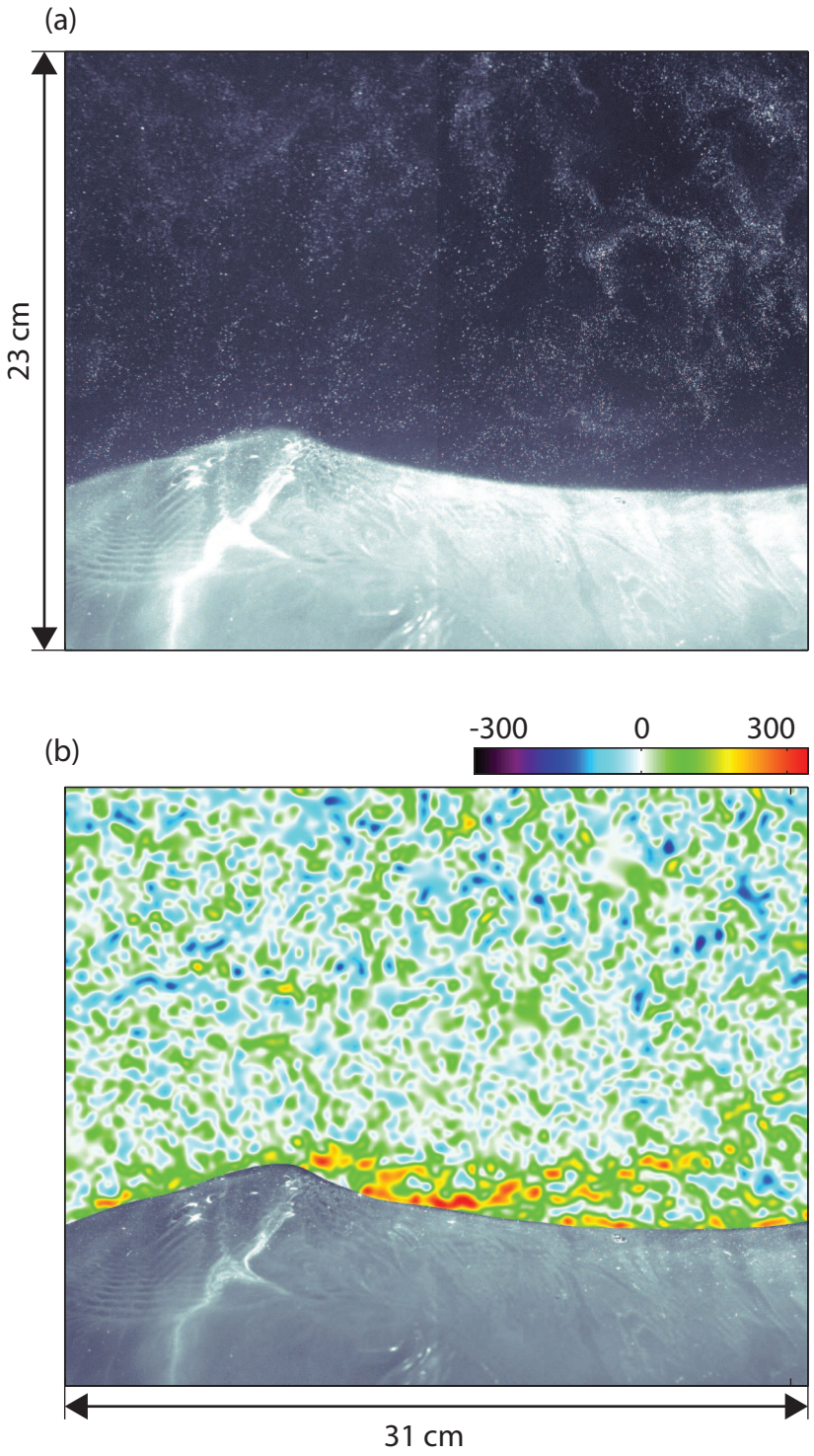

Figure B.4: Field PIV results. (a) Raw PIV image (resolution 0.15 mm/pixel). (b) Vorticity ω (s^{-1})

picture is reminiscent of the young airflow-separating waves observed in our laboratory (previous chapters of this dissertation). The vorticity field suggests that the crest of this wind wave causes the airflow to separate from the surface, generating in the process potential sources of increased turbulence. The brief qualitative result shown here is presented for illustrative purposes and shows quantitatively similar structures as those observed and studied in the laboratory. An in depth study of our field PIV data, and surrounding measurements, will be the object of future work.

Appendix C

LABORATORY DURATION LIMITED WAVE GENERATION EXPERIMENTS

C.1 Introduction

When the wind begins to blow over a relatively calm water surface, short wind waves are generated. The details of the mechanisms involved in this phenomenon are still not fully understood, because of the technical difficulties involved in measuring transient kinematics at the air-sea interface. Yet, this is an important problem for air-sea momentum flux estimates, sea state prediction, and micro-wave radar back-scatter, because local turbulent variations in the wind (wind gusts) are, more often than not, generating similar duration limited short wind wave fields, on top the background wave spectrum.

Numerous theoretical models have been suggested to explain the initial stages of wave generation by wind (e.g., Jeffreys, 1925; Miles, 1957; Phillips, 1957; Belcher et al., 1993). Recently, direct numerical simulations on the initial stages of wind wave generation were performed by Lin et al. (2008). In qualitative accordance with the theory of Phillips (1957), they found evidence of an initial linear growth stage, when mainly turbulent fluctuations in the airflow transfer momentum to the undisturbed water surface. Once waves are generated, the growth rate of waves is exponential (e.g., Hasselmann et al., 1973). Lin et al. (2008) suggested that phase-locked wave-coherent pressure fluctuations control the wind-wave energy transfers at this stage, in agreement with the sheltering hypothesis of Belcher et al. (1993).

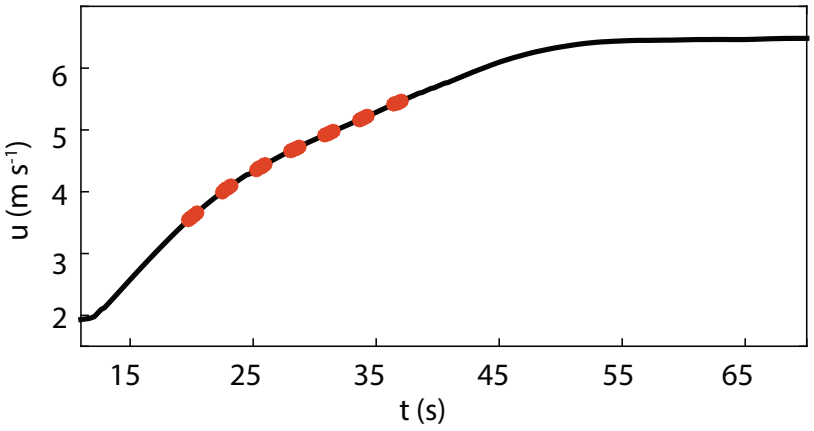

Figure C.1: Wind velocity ramp, at 9.5 cm above the mean water level (black line), and positions in time of the samples shown in figure C.2 (red dots).

An important contribution to the topic is provided by the detailed laboratory experiments performed by (Kahma and Donelan, 1988), who carefully measured an airflow friction velocity threshold for wind wave generation (u_* ~2 cm s^{-1}), and estimated exponential growth rates once waves were higher than 1 mm.

Our high resolution two-dimensional imaging system may provide new information on the problem of generation of waves by wind.

C.2 Preliminary results

Particle image velocimetry measurements were performed in the air above the water surface, while the winds in the large wind-wave tank were being ramped up from 0 to 7 m s^{-1} (U_{10}). The data presented in this appendix were taken at a fetch of 10 m. In figure C.1, we show the smoothed wind velocity ramp. In figure C.2, we show seven series (rows) of six consecutive two-dimensional velocity fields (separated by 1/7.2 s), over the developing waves. The PIV airflow velocity fields are plotted above the water-side portions of the PIVSD LIF images. In these preliminary results, we note the presence of a number of features that were present in the steady state fetch limited wind wave experiments discussed in chapter 3. These include turbulent ejections of regions of low velocity fluid away from the water surface, just as waves

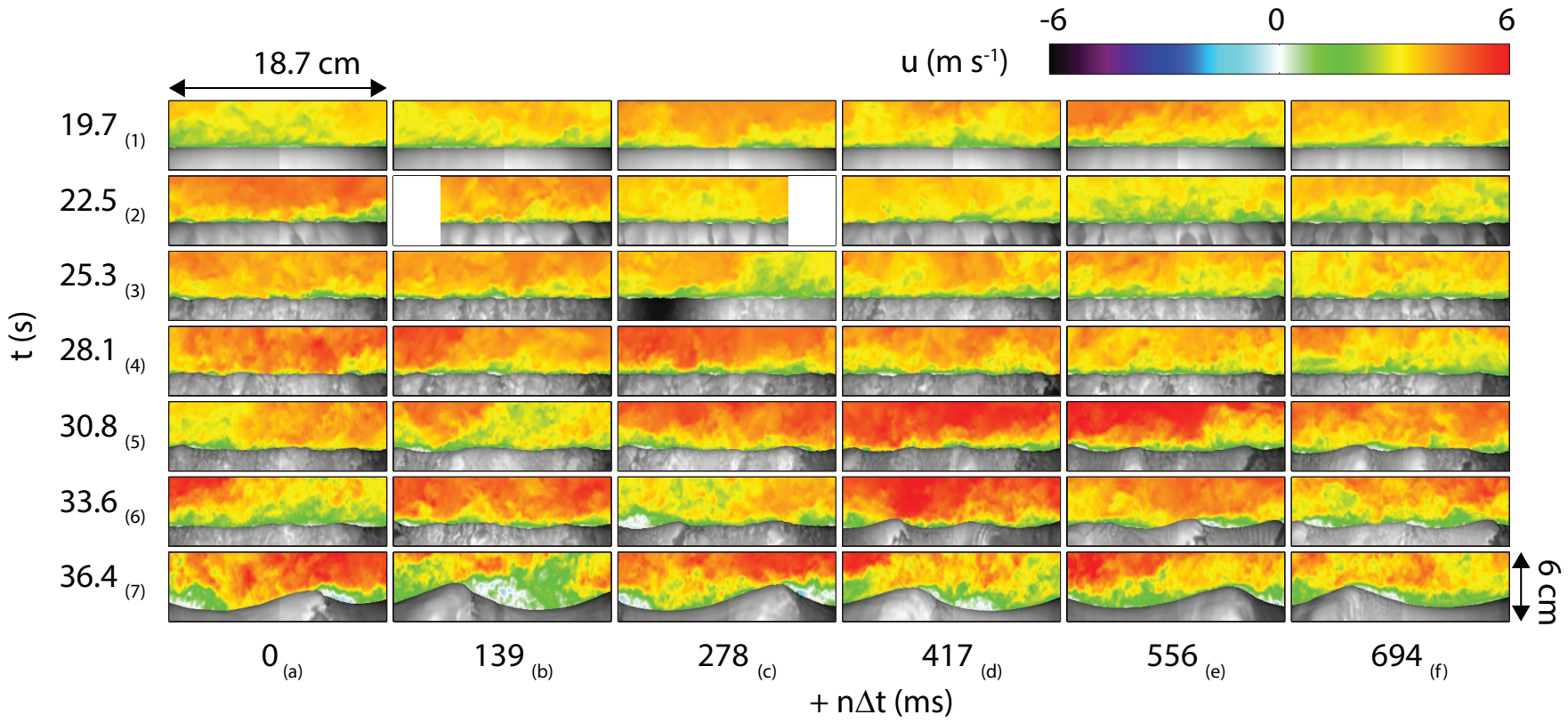

Figure C.2: Duration limited wind wave generation. Each line (noted (1) through (7)) of the color plots starts at one of the times marked in red on the ramp in figure C.2. Consecutive frames (separated by 1/7.2 s, noted (a) through (f)) are plotted side-by-side. All written time stamps are approximations, since the actual times are frequency fractions (nanosecond precision, provided by the National Instruments hardware, see chapter 2 for additional details on timing). The white rectangles are areas that were left out of the PIV calculations, because the anti-fog window wiper was then obstructing part of the field of view.

are being detected (see for example, the velocity in panel 1f. We should mention here that high resolution high frequency (93.6 Hz) single point water surface elevation measurements were also taken during these experiments, using our wave gauge system (WG, see chapter 2 for additional details), but the results are not shown here. A modification was done to the WG system for these small scale wind wave generation experiments: The upwind WG camera (WG1) was fitted with a 180 mm (Nikon) telephoto lens (instead of the previously used 60 mm, see table 2.2 in chapter 2), in order to increase the resolution of the optical water height measurements. However, in order to identify the wave "inception wind speed" (Kahma and Donelan, 1988), the underwater refraction patterns visible on the LIF images below the air-water interface, can potentially be a better indicator than water height measurements. This is because the underwater LIF refraction patterns are connected to the slope of the water surface. For a given disturbance of the water surface, variations in slope are larger than the variations in water height, since, for example, the slope is a higher order moment of the wave spectrum than the elevation. We observe a very slight disturbance in the underwater refraction pattern, starting in panel 1d. Later, (row 2), the small waves show a surprising pattern of rounded crests, and sharp troughs, reminiscent of Crapper waves (Crapper, 1957). This is very surprising, because similar waves have never been observed in previous wind wave generation studies, to the best of our knowledge. Later (rows 3 and 4), the water surface is very ruffled and shows small scale roughness elements. The airflow appears turbulent, and we observe numerous ejections and sweeps. Starting in row 5, we begin to see more organized patterns in the water and in the air. In panel 5f, sheltering clearly takes place past the crest of the first wave on the left. Later, around a $t = 36.4$ s (~ 15 s after the first detectable water disturbances), airflow separation appears to dominate. Hence, these preliminary results hint to the importance of airflow separation for the early stages of wind wave generation.